공학박사 학위논문

Design of Layered Cathode Materials for High-Performance Li-Ion Batteries

고성능 리튬이온전지용 층상구조 양극소재의 설계

2019년 **2**월

서울대학교 대학원

재 료 공 학 부

박 준 호

Abstract

Design of Layered Cathode Materials for High-Performance Li-Ion Batteries

Jun-Ho Park

Department of Materials Science and Engineering

Seoul National University

The importance of lithium ion batteries has increased as energy and environmental problems have increased, and research on cathode materials with high capacity, long life, and low cost for application to electric vehicles and electric power storage is being actively conducted. High-energy-density layered cathode materials such as over-lithiated layered oxides ($xLi_2MnO_3 \cdot (1-x)LiMO_2$) and Ni-rich layered oxides ($LiMO_2$ with ≥70 mol.% of Ni among Ni, Co and Mn) were designed and fabricated for the high-performance lithium ion batteries. Understanding intrinsic properties of high-energy-density cathode materials and improving the layered cathode materials through ideal post-treatment is most important for maximizing cell performances.

Herein, several post-treatment approaches including conventional post treatment based on the wet and dry processes are systemically executed and found limits based on the following

phenomena.

The wet process is mainly suitable for Ni-rich layered oxides in which lithium residue (or residual lithium) control is essential, and can be divided into an evaporation method and a filtering method. The evaporation method was insufficient in the residual lithium removal effect, but had less active material damage and was effective in forming a surface coating layer. The filtering method was very effective for lithium removal, but there was a possibility of deterioration in cell performance. The dry method could be effective in forming a functional coating layer, but it was difficult to form a uniform coating layer. The electrochemical and thermally stabilized vanadyl phosphates($VOPO_4$) was introduced into a over-lithiated layered oxides(OLO) by the mechano-fusion method, and the first cycle efficiency and the thermal stability were improved.

To overcome those limits, molecular-level rearrangements of Ni-rich layered oxides ($LiNi_{0.80}Co_{0.15}Mn_{0.05}O_2$, Ni-rich NCM) induced by thermal decomposition of a Co-embedded metal-organic framework is firstly suggested. As a result, the poor cyclability and thermal stability of Ni-rich NCM (resulting from irreversible changes in surface structure) are improved by the formation of a highly stable Co- and Ni-rich domain with a spinel-like phase on the surface.

Keywords: Li-ion batteries, cathode, layered structure, post treatment, surface treatment

Student Number: 2016-30201

Contents

List of Tables

Table 3.1 Inductively coupled plasma-atomic emission spectrometry (ICP-AES) results for MOF (ZIF-67).

Table 3.2 Results of Brunauer-Emmett-Teller (BET) analysis of N_2 adsorption–desorption isotherms for bare, 1 wt.% MOF-treated, and 6 wt.% MOF-treated Ni-rich NCM.

List of Figures

Figure 2.1.1 Schematic flow of the coating process based on evaporation.

Figure 2.1.2 (a) XRD patterns of NCM and TM/P-coated NCM and (b)-(c) enlarged XRD peaks

Figure 2.1.3 SEM images of pristine and TM/P-coated NCM with various TM/P ratios (a) NCM, (b)–(e) Al/P-coated NCM, (f)–(i) Co/P-coated NCM, (j)–(m) Fe/P-coated NCM.

Figure 2.1.4 TEM image of *Tm*/P coated NCM

Figure 2.1.5 SEM images of Co/P coated h-NCM

Figure 2.1.6 (a) Al 2p and (b) P 2p XPS spectra of Al/P-coated NCM; (c) Co 2p and (d) P 2p XPS spectra of Co/P-coated NCM; (e) Fe 2p and (f) P 2p XPS spectra of Fe/P-coated NCM.

Figure 2.1.7 Cycling performances of pristine and TM/P-coated NCM samples with various TM/P ratios (a) Al/P coated NCM (b) Co/P coated NCM (c) Fe/P coated NCM.

Figure 2.1.8 Cycling performances of pristine and Co/P-coated h-NCM samples.

Figure 2.1.9 Overall design chart for the reaction between MP/MO and $LiOH/Li_2CO_3$.[7]

Figure 2.1.10 A schematic view of removing residual lithium at the surface of the cathode materials during the surface treatment[7].

Figure 2.1.11 Phase diagram for (a) $Co_3(PO_4)_2$−$LiOH/Li_2CO_3$−O_2 and (b) P_2O_5−$LiOH/Li_2CO_3$−O_2[7].

Figure 2.2.1 (a) Plot of the discharge capacity vs. cycle number for coin-type half cells. (b) Plot of the residual lithium and capacity retention vs. the amount of water used for washing

Figure 2.2.2 SEM images of (a) bare, and washing and drying at (b) 80 ℃, (c) 120 ℃, and (d) 190 ℃ without post heat treatment and post heat treated powder after drying at (e) 80 ℃, (f) 120 ℃, and (g) 190 ℃. The ratio of water to NCM is 1:1.

Figure 2.2.3 XPS results for the O1s peak of NCM samples with increasing sputtering time: (a) bare (b) dried at 80 ℃ (c) 120 ℃ (d) 190 ℃ without post heat treatment and post heat treated powder after drying at (e) 80 ℃ (f) 120 ℃ (g) 190 ℃. The ratio of water to NCM is 1:1.

Figure 2.2.4 TEM images of (a) bare, and after washing and drying at (b) 80 ℃, (c) 120 ℃, (d) 190 ℃ without post heat treatment and post heat treated powder after drying at (e) 80 ℃, (f) 120 ℃, and (g) 190 ℃. The ratio of water to NCM is 1:1.

Figure 2.2.5 Schematic illustration of the observed surface changes for NCM during the washing, drying, and post heat treatment (HT) processes.

Figure 2.2.6 (a) Voltage profiles vs. capacity for coin-type cells at a rate of 0.1 C between 2.8–4.35 V for the bare and HT after drying at 80 ℃, 120 ℃, and 190 ℃. (b) Cycleability tests at a rate of 1 C in the coin-type half cells. (c) Electrochemical impedance spectroscopy (EIS)

comparison of the first discharge state of bare, and after HT after drying at 80 ℃, 120 ℃, and 190 ℃.

Figure 2.2.7 (a) Plot of the cyclability of 18650 type cell at a rate of 1 C. The ratio of water to NCM is 1:1 and HT after 120 ℃ drying sample is used as a cathode. (b) Comparison of the gas evolution after cycling an 18650 cell 300 times for a bare NCM cathode and a washed cathode (using a water amount of 1:1 water to NCM and HT after drying at 120 ℃).

Figure 2.2.8 Powder XRD patterns for (a) bare and washing water amount of (b) 0.7:1 (powder : water), (c) 1:1, (d) 1:2, (e) 1:5 and magnified image for the dashed line rectangle at the right side, and (f) corresponding lattice parameters.

Figure 2.2.9 SEM images of (a) bare and washing water amount ratio of (b) 1:0.7 (powder : water) (c) 1:1 (d) 1:2 and (e) 1:5

Figure 2.2.10 TGA profiles of the washed powders dried at 80 ℃, 120 ℃ and 190 ℃ without post heat treatment. The ratio of water to NCM is 1:1.

Figure 2.2.11 Powder XRD patterns for (a) no washing/drying (b) drying temperature of 80 ℃ (c) 120 ℃ (d) 190 ℃ (e) post-heat-treatment(HT) after 80 ℃ (f) 120 ℃ (g) 190 ℃ drying

Figure 2.2.12 Schematic diagram of gas sampling system (valves at each end of manifold are omitted for simplicity)

Figure 2.3.1 Schematic figures showing the process for initial lithation and de-lithiation of (a) OLO and (b) $VOPO_4$ coated OLO.

Figure 2.3.2 XRD diffraction patterns of (a) as-synthesized $VOPO_4$ and (b) OLO. SEM micrographs of (c) as-synthesized $VOPO_4$ and (d) OLO.

Figure 2.3.3 First- and second-cycle voltage profiles at 0.1C of 2032 coin type half-cells with (a) $VOPO_4$ and (b) OLO positive electrodes having 0, 10 and 20 wt.% of VOPO4 in the blended state. (Temperature; 25 ^{o}C, electrolyte; 1.3M $LiPF_6$/EC:DEC and the electrode capacity areal density; 1 mAh cm^{-2}.)

Figure 2.3.4 SEM images of (a) ball-milled $VOPO_4$ and (b) 1 wt.% $VOPO_4$-coated OLO. (c) Phosphate and (d) Vanadium EDX mapping image of Figure 2.3.4(b).

Figure 2.3.5 (a) Initial voltage curves of the bare OLO and the 0.5, 1 and 2 wt.% $VOPO_4$ coated OLO at a current density of 25 $mA \cdot g^{-1}$ and (b) discharge voltage curves of 2032 coin type half-cells with bare and $VOPO_4$-coated OLO recorded at a current density of 450 $mA \cdot g^{-1}$ after the controlled charge sequence (current density: 125 $mAh \cdot g^{-1}$; constant voltage mode was inserted to the end of charge until 12.5 $mA \cdot g^{-1}$) (c) the discharge voltage curves under 2C current density of the 2032 coin type half cells

Figure 2.3.6 Differential scanning calorimetry (DSC) graphs of the fully charged bare and 0.5 wt.% $VOPO_4$-coated OLO.

Figure 2.3.7 Differential capacity versus voltage curves of (a) 1^{st} and 2^{nd} cycle for $VOPO_4$ and (b) 1^{st} cycle for $VOPO_4$ blended OLO

Figure 2.3.8 Capacity loss(2032 coin type half-cell cycling at 1C rate) by conventional surface coating materials (Al_2O_3)

Figure 3.1 TGA curves and schematic diagrams showing the corresponding mechanisms up to 800 ℃ to the MOF-treated Ni-rich NCM compared to the uncoated control sample. (a) MOF (ZIF-67) attached to the Ni-rich NCM surface, (b) oxidative decomposition of MOF (ZIF-67) during heat treatment in air, and (c) remnant Co ions embedded on the Ni-rich NCM surface.

Figure 3.2 SEM images of (a) bare Ni-rich NCM, (b) 1 wt.% MOF-treated Ni-rich NCM, (c) 6 wt.% MOF-treated Ni-rich NCM, and (d) as-synthesized MOF. The insets show magnified images.

Figure 3.3 Cross-sectional high-angle annular dark field scanning transmission electron microscopy (HAADF-STEM) images and magnified images of (a,b) bare Ni-rich NCM and (e,f) 6 wt.% MOF-treated Ni-rich NCM. The corresponding EELS spectra (Ni, Co) of (c,d) bare and(g,h) 6 wt.% MOF-treated Ni-rich NCM.

Figure 3.4 Normalized XRD patterns of (a) bare Ni-rich NCM, (b) 1 wt.% MOF-treated Ni-rich NCM, and (c) 6 wt.% MOF-treated Ni-rich NCM.

Figure 3.5 High-resolution transmission electron microscopy (HR-TEM) and fast Fourier transform (FFT) patterns of bare (a–d) and 6 wt.% MOF-treated Ni-rich NCM (e–i).

Figure 3.6 (a) First charge–discharge curves between 2.8 and 4.35 V (vs. Li+/Li) at 0.1 C rate and the resulting 1C cycleability of bare, 1 wt.% MOF-treated, and 6 wt.% MOF-treated Ni-rich NCM at (b) room temperature and (c) 45 ℃.

Figure 3.7 Differential scanning calorimetry (DSC) curves for bare, 1 wt.% MOF-treated, and 6 wt.% MOF-treated Ni-rich NCM charged to 4.35 V.

Figure 3.8 Thermogravimetric analysis curve of metal-organic framework ZIF-67 up to 750 ℃

Figure 3.9 Cross-sectional high-angle annular dark field scanning transmission electron microscopy (HAADF-STEM) images and the corresponding EELS spectra (Ni, Co) of 1 wt.% MOF-treated Ni-rich NCM.

Figure 3.10 Pore size distributions of bare, 1 wt.% MOF-treated, and 6 wt.% MOF-treated Ni-rich NCM.

Figure 3.11 X-ray diffraction pattern of MOF (ZIF-67).

Chapter 1.
Introduction (Theoretical Review)

1.1 Lithium ion battery

Lithium ion battery (LIB) is mainly comprised of 4 representative components such as a cathode (positive), an anode (negative), an electrolyte and a separator.(Figure 1.1) The cathode (positive) materials generally contain lithium embedded transition metal oxides such as layered structure, tunnel-structure. The anode (negative) materials contain insertion-type materials, conversion-type materials and alloying-type materials. The electrolyte, which typically consist of inorganic lithium salts dissolved in mixture of organic solvents and, should be an ionic conductor and electronic insulator. The separator is to prevent short circuiting between the cathode and anode and provide lithium ion transport during charging and discharging. During cycling, lithium ions exchange between cathode and anode which phenomena which are called 'rocking-chair'. [8–11] Cathode material can accept the lithium ion in its crystal structure reversibly. $LiCoO_2$ as cathode and graphite as anode system was commercialized by Sony at 1991. To achieve higher energy density for the LIB, higher capacity and operation voltage is important factor. During charging lithium ions are extracted from $LiCoO_2$ cathode and intercalated into graphite anode in Figure 1.2. [2,10,12]. The capacity means the amount of lithium which can be extracted from cathode. The cell potential is determined by the difference between the chemical potential of the lithium in the cathode and anode ($\triangle G = -EF$), as shown in Figure 1.3. LIB operates at high ltage, high energy density, long cycleability, light weight

compared with other battery systems such as lead-acid batteries.(Figure 1.4) Furthermore, Many researchers have been studied about LIB, and numerous electronic devices and electric vehicles (EV) are adopted LIB because of these advantages.[3]

1.2 Cathode material for lithium ion batteries

Cathode materials are required to have light weight and high chemical potential for higher capacity and voltage to provide optimum utilization of the lithium ion batteries. Cathode materials can be categorized by the crystallographic structures, and the characteristic of the cell are, as shown in Figure 1.5, also dramatically different by the cathode materials. Many researchers are typically divided the cathode materials into 3 parts such as layered structure, olivine structure and spinel structure. $LiMO_2$ (M = transition metal) layered structure is used for lithium ion battery cathode material. The 3d transition metals (Ni, Co, Mn) are used for M in $LiMO_2$. $LiCoO_2$ and $LiNiO_2$ are well-known for layered structure. Spinel structures LiM_2O_4 and olivine structure $LiMPO_4$ are also used for lithium ion battery cathode, but the applications are limited due to lower capacity and rate performance.

Among layered cathode material recently Ni-rich $Li(Ni,Co,Mn)O_2$ and Li-rich and Mn-rich $Li(Ni,Co,Mn)O_2$ are researched for high energy density battery. In Ni-rich $Li(Ni,Co,Mn)O_2$ the high capacity is achieved $Ni^{2+/4+}$ redox reaction during charge-discharge.

In Li-rich and Mn-rich $Li(Ni,Co,Mn)O_2$ the high capacity is achieved through activation of oxygen in lithium-rich Li_2MnO_3 phase during high voltage activation above 4.5V in Figure 1.5.

1.3 Performance degradation of lithium ion batteries

Degradation of the lithium ion batteries performances occurs in many ways in the cell such as cathode, anode, electrolyte and separator. However, cathode materials are mainly discussed in this study.

Degradation of the cathode materials is generally happened at (i) active materials/electrolyte interfaces (ii) active materials and (iii) composite electrodes (current collector, binder, conductive agent, etc.). Many literatures are pointed out that materials/electrolyte interfaces are main degradation factor, and physically, chemically, electrochemically irreversible reactions at this area are essentially needed to be understood and improved [4,13,14]. Degradation phenomena regarding cathode materials are generally described as followed;

- Transition metal dissolution[15–17]
- Attack by the acidic compounds from moisture[18,19]
- Irreversible structural change of the cathode materials during cycling [20–22]
- Crack generation of the inter-particles and between the electrode components during cycling [23,24].

Most of the above problems are initiated from the surface of the cathode materials as shown in figure 1.6 [6,25–27]. Furthermore, proper post-treatment for making stabilized structure and morphology of surface is important.

1.4 Previous approaches

As mentioned in chapter 1.3, degradation occurred and propagated in to the entire bulk structure of cathode materials. Furthermore, many researchers are tried surface modifications to make it stabilized to degradations. In general, the previous approaches could be categorized into several based on its functional aspects such as protections from side reactions by stable metal oxides [28–32], Functional materials (i.e. Li ion/electron conducting or thermally stable materials)[8,19,33–37].

On the other hands, what type of surface layer is ideal when the active material is surface treated?

Depending on the shape, there are 3 main types: rough surface, core-shell, ultra-thin film as shown in Figure 1.10[26]. Ultra-thin film would be near the most ideal surface layer. However, it is mainly implemented by atomic layer deposition (ALD), chemical vapor deposition (CVD) and other deposition methods, and these methods have limitations that are difficult to be considered in industry.

1.5 The aim of this thesis

Layered oxides such as OLO and Ni-rich layered oxides are the most balanced material to meet the high energy density and safety requirement.

In Figure 1.7, lithium-rich Li(Ni,Co,Mn)O_2 phase diagram and electrochemical reaction showing dramatically high capacity above 250 mAh/g[38]. There are several obstacles for commercialization which are irreversible structural changes by the oxygen evolution at the high voltage, the voltage decay from phase instability during charge-discharge condition, low electron conductivity and cycleability as shown in Figure 1.8. To overcome those problems, various approaches have been tried. Doping, surface coating, and composite structure improved the performance even though much improvement is strongly needed.

Among layered ternary cathode materials, Ni-rich layered oxides (Ni-rich NCM with $\geq$70 mol.% of Ni and the remainder Co and Mn), are also good candidates as cathode materials due to their high capacity. However, challenges such as poor cyclability and gas evolution from the surface of Ni-rich NCM during charge–discharge cycles limit commercialization of this material. because of the presence of reactive and unstable Ni^{4+} ions in the delithiated state.[39–41] The presence of surface residual lithium, which source of gas evolution, is an inevitable result of the manufacturing process of Ni-rich layered oxides. Therefore, it is necessary to

understand and optimize the chemical behavior of residual lithium to successfully commercialize this material [42,43].

In chapter 2, several post-treatment approaches including conventional post treatment are suggested and analyzed the phenomena,

Firstly, I examined the effect of wet coating–deposited TM phosphates on the electrochemical performance of $Li_{1.0}Ni_{0.8}$ $Co_{0.15}Mn_{0.05}O_2$ (NCM) positive electrode materials, anticipating a synergistic effect between the removal of Li residuals by their reaction with the coating material and protective layer formation during wet coating. As a result, I demonstrate that surface modification can improve the capacity and cycling performance of NCM and effectively reduce the amount of Li residuals

Secondly, I investigated the factors affecting the efficiency of the washing process for Ni-rich layered oxides. I studied the changes that occur at the surface of washed Ni-rich layered oxide cathodes, including the residual lithium layer.

Finally, $VOPO_4$, which have the high potential of 3.8 V, is beneficial to reserve the energy density of the positive electrode. $VOPO_4$ can provide sites for the insertion of Li that is otherwise irreversibly lost during OLO discharge. Furthermore, it is well known that the PO_4^{3+} polyanion is highly thermally stable owing to the strong bond between P and O. In this view, the multi-functional coating of $VOPO_4$ was used to improve the first-cycle irreversibility,

cycling stability, and thermal stability of OLO

In chapter 3, using the MOF (a metal-organic framework (MOF) containing Co, zeolitic imidazolate framework-67 (ZIF-67)), additional Co ions could be introduced onto the surface of Ni-rich NCM, leading to extensive molecular-level surface rearrangements during a post-heat treatment, via reactions considered to be galvanic replacement reactions. Differing from the layered-to-spinel transformation in the middle of charge–discharge cycling, the introduction of an optimum amount of spinel-like phase into the surface lattice structure of Ni-rich NCM before cycling is beneficial for enhancing the Li-ion kinetics and stability of the layered active materials. The resultant Co- and Ni-rich domain with a stable spinel-like phase formed on the surface improved the cyclability and thermal stability of the MOF-treated Ni-rich NCM.

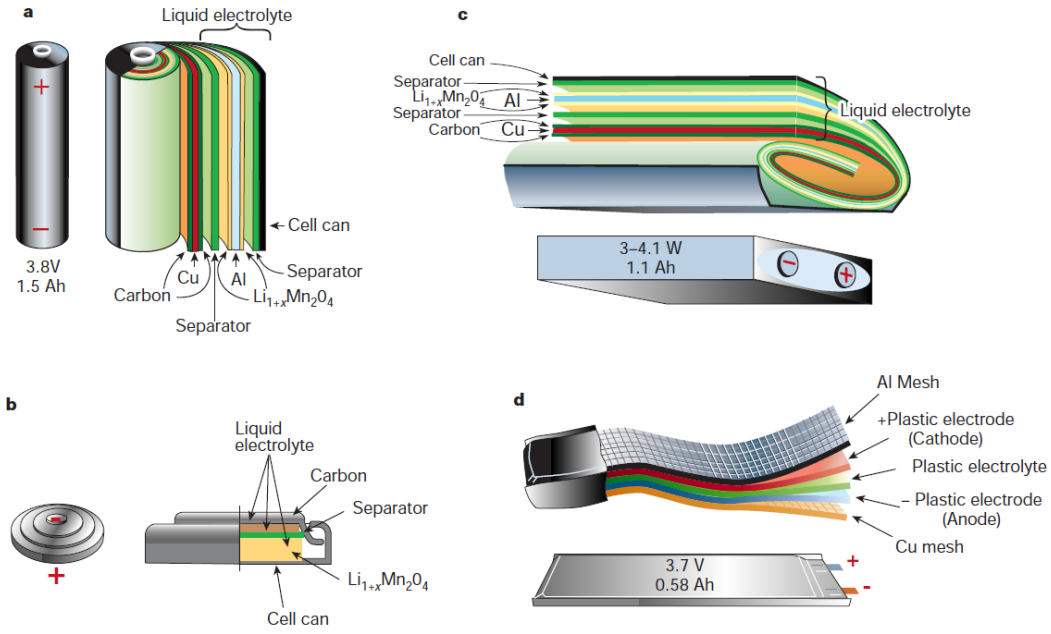

Figure 1.1 various type of the Li-ion battery construction (a) cylindrical-, (b) coin- (c) prismatic- and (d) pouch- type cells. [1]

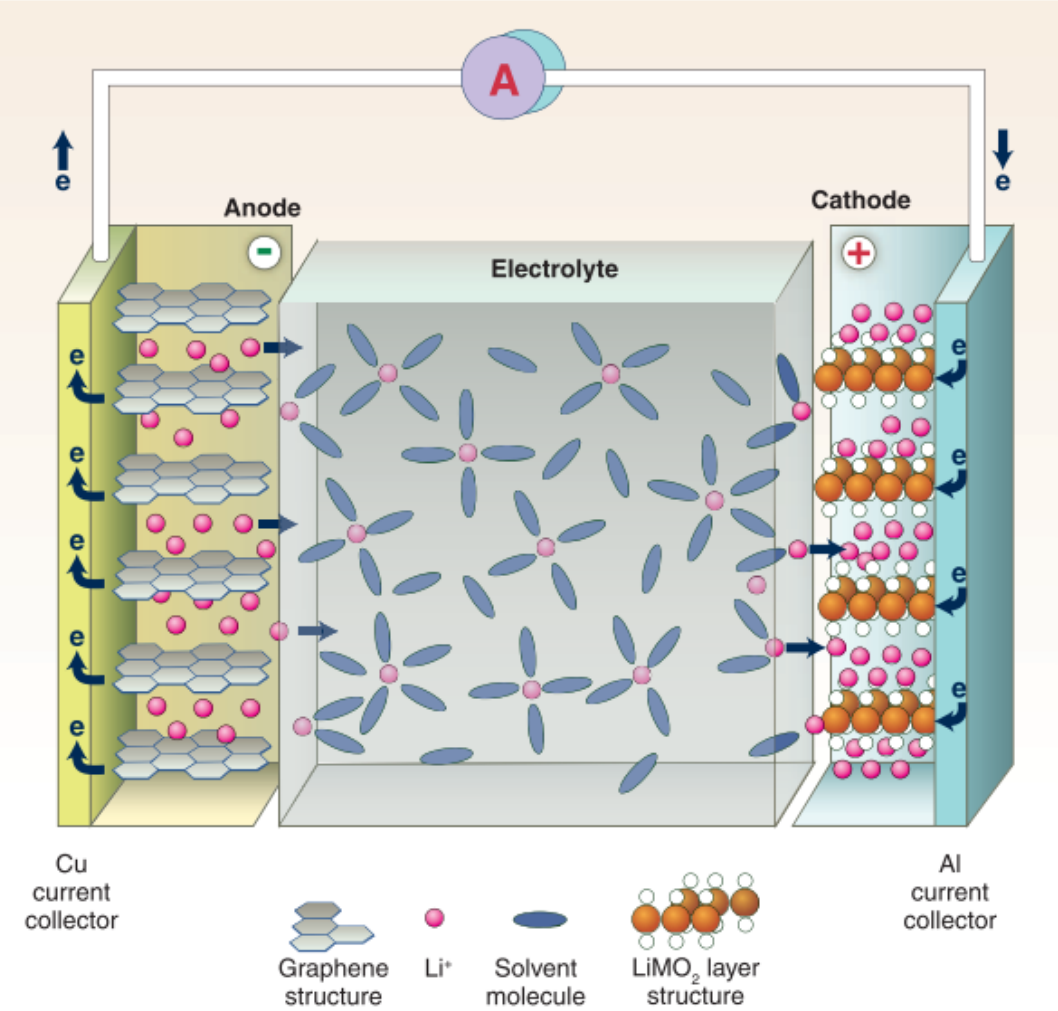

Figure 1.2 Schematic description of lithium ion battery operation. [2]

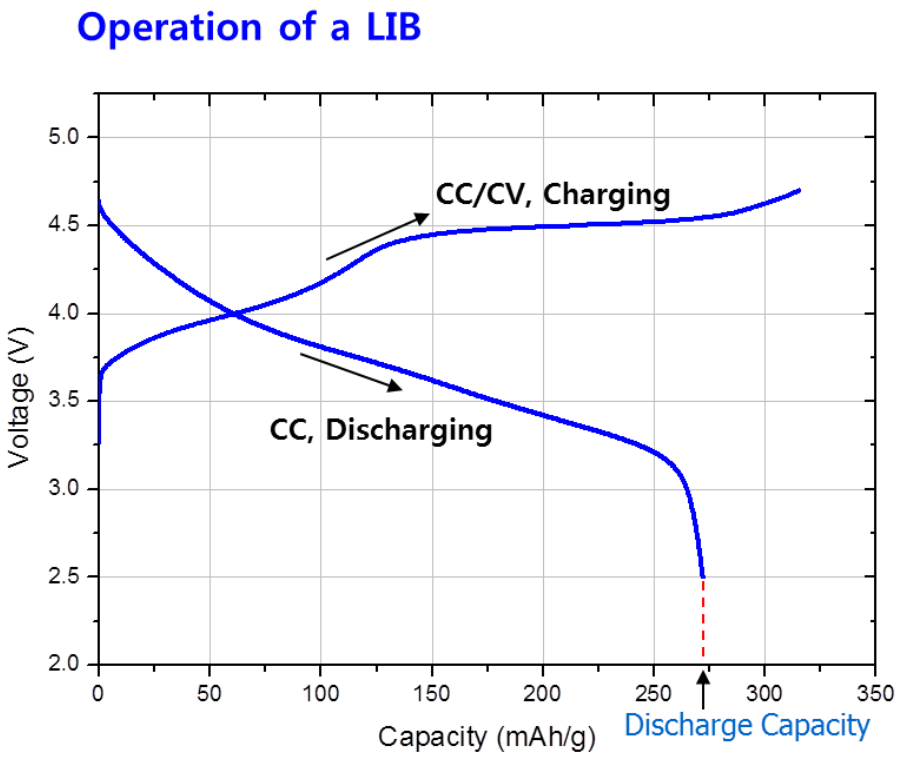

Figure 1.3 Initial charge-discharge profiles measured upon galvanostatic cycle.

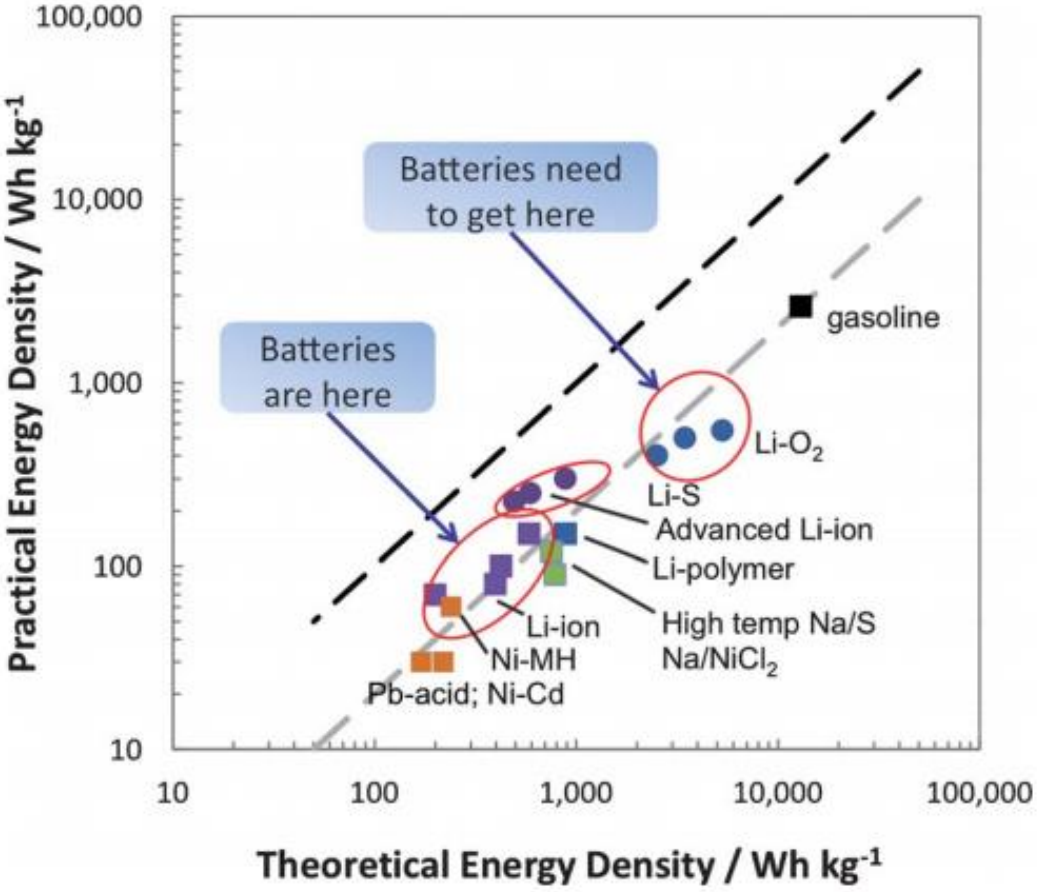

Figure 1.4 A Plot of the theoretical specific energy of various battery systems vs. their practical specific energy density.[3]

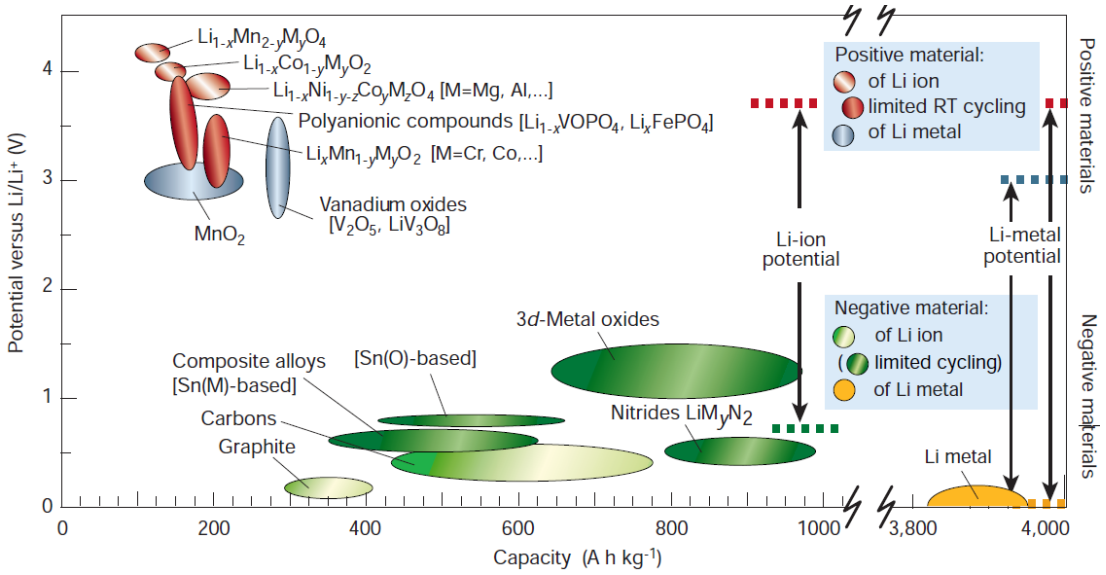

Figure 1.5 Schematics of operational voltage difference versus capacity for various cathode and anode materials.[1]

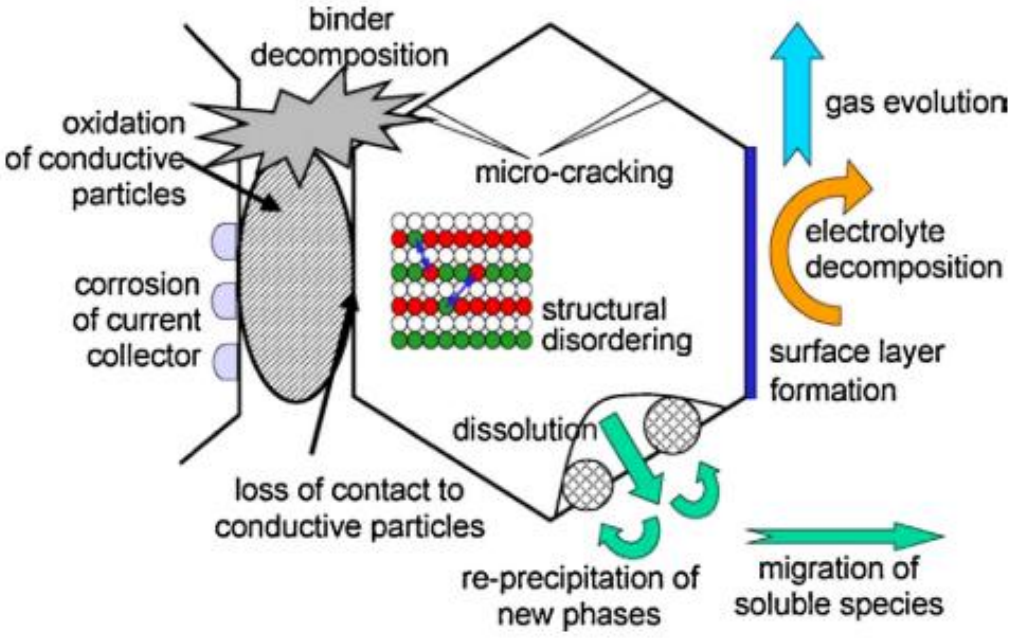

Figure 1.6 Schematic descriptions for degradation mechanism of cathode materials [4].

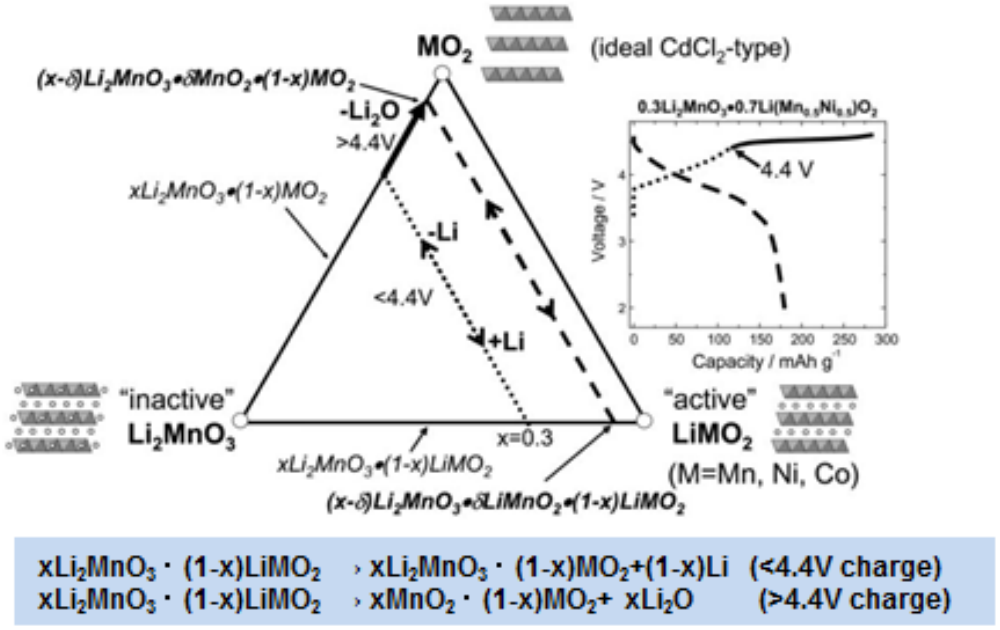

Figure 1.7 Compositional phase diagram of lithium-rich Li(Ni,Co,Mn)O_2.[8]

(a)

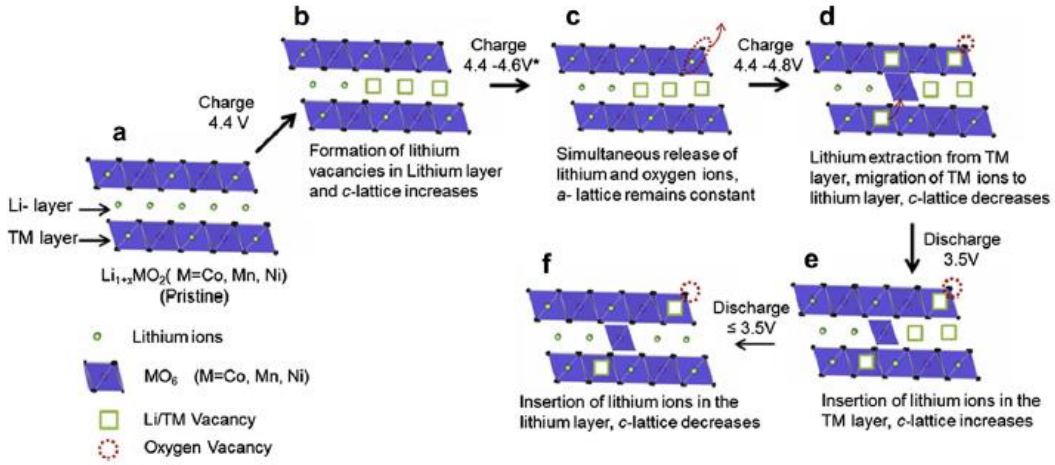

(b)

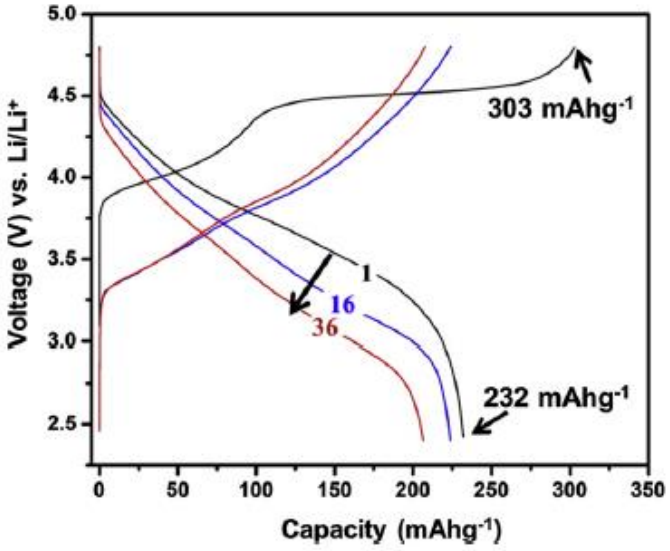

Figure 1.8 (a) structural change depends on voltage and (b) voltage drop of OLO during cycling [5].

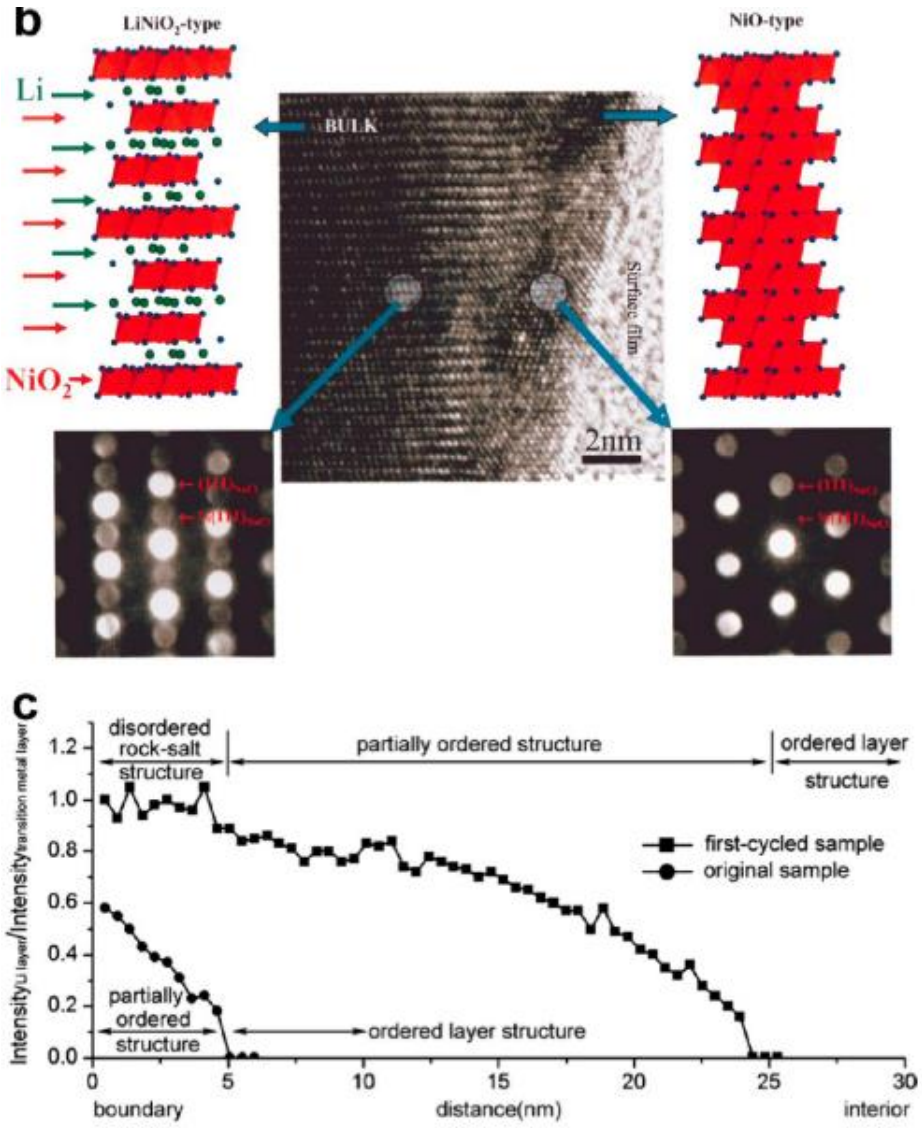

Figure 1.9 schematic description of structural differences between surface and bulk of layered oxides [6].

Figure 1.10 Schematic of three types of surface coating: rough coating, core- shell structure, and ultra-thin film [26]

Chapter 2.
Conventional post-treatment (Wet/Dry process)

2.1 Introduction

High-energy-density layered cathode materials such as over-lithiated layered oxides ($xLi_2MnO_3 \cdot (1-x)LiMO_2$) and Ni-rich layered oxides ($LiMO_2$ with ≥70 mol.% of Ni among Ni, Co and Mn) were designed and fabricated for the high-performance lithium ion batteries.

Degradation of the cathode materials for lithium ion batteries mainly introduced from the surface. Furthermore, understanding and improving surface of the layered cathode materials is most important for maximizing cell performances.[26,44] Herein, several post-treatment approaches including conventional post treatment are suggested and analyzed the phenomena. In addition, it was confirmed that cell performance were improved by those suggested post treatment in various way such as coin type half cells, 18650 cylindrical type full cells, thermal stability test, etc.

2.1.1 Wet processes for Ni-rich layered oxides

Nickel-rich layered oxides ($LiNi_xM_{1-x}O_2$; M=Mn, Co, and Al; x>0.5) are among the most promising candidate materials because of their high capacity, excellent rate capability, and low cost. However, Ni-rich layered oxides show poor cyclability at high operating temperatures (>45^{o}C) and high voltages (>4.3 V) because of the presence of reactive and unstable Ni^{4+} ions in the delithiated state.[39–41] The presence of unreacted lithium on the surface of Ni-rich

layered oxides leads to the formation of lithium impurities

(termed residual lithium) such as lithium carbonates (Li_2CO_3) and lithium hydroxides (LiOH). These species are extremely prone to reactions with atmospheric carbon dioxide (CO_2) and moisture.[45] The presence of the compounds produced in reactions with residual lithium causes unwanted side reactions, such as reductive decomposition at high voltages, which affect the irreversible capacity loss and gas evolution and cause gelation during the slurry process[42,43]. The presence of surface residual lithium is an inevitable result of the manufacturing process of Ni-rich layered oxides. Therefore, it is necessary to understand and optimize the chemical behavior of residual lithium to successfully commercialize this material. Several recent reports detail attempts to reduce the residual lithium content by post-treatment strategies such as washing and surface treatments.[42] However, these reports do not provide a complete description of residual lithium. The lack of a fundamental understanding of residual lithium may prevent the use of many commonly used surface-coating compounds such as metal oxides, metal fluorides, and metal phosphates with Ni-rich layered oxides, which have high residual lithium content.[46] Y. Yang et al. showed that Ni-rich layered oxides such as $LiNiO_2$ are easily affected by contact with air during storage.[47] Cho et al. analyzed the active cathode materials by FTIR spectroscopy and titration methods, and they found that the residual lithium content decreased after multiple washes with water.[48]

2.1.1.1 Surface treatment with evaporation

Significant effort has been directed at removing Li residuals to achieve stable electrochemical performance, with a representative effective strategy featuring washing these residuals away using solvents such as deionized (DI) water or ethanol. However, this process suffers from the concomitant dissolution and loss of Li in the layered structure, leading to a sharp performance drop. Another method features the formation of a physical barrier, using inert materials such as Al_2O_3 to coat the positive electrode surface and suppress the reaction between the positive electrode and the electrolyte. Although this strategy avoids the above side effect, it results in capacity loss and lowers the rate performance of the electrode due to the poor electrical conductivity of the coating layer. In addition, transition metal (TM) phosphates such as $AlPO_4$, $CoPO_4$ and $FePO_4$ are another type of promising coating materials, and they have been found to improve the cycle performance and thermal stability when applied to $LiCoO_2$ and layered oxides [49]. As shown in Figure 2.1.9, Al, Co and Fe were selected with reference to the calculated values of reactivity and efficiency of residual lithium represented by LiOH and Li_2CO_3[7]. In addition, metal phosphate is known to be electrochemically stable in the NCM potential window, as well as being able to conduct Li ion. Therefore, unlike conventional coating materials such as metal oxides, metal phosphates; there is an advantage that the

capacity reduction effect by the inert coating materials and resistance increase problems can be minimized. Although these surface coating methods have been shown to enhance the electrochemical performance of cathodes, they do not entirely prevent side reactions on the cathode surface and there have not been many studies about transition metal phosphates coating effect for nickel-rich layered oxides. Moreover, the previous studies were not focused on the removal of Li residuals [50]. Herein, I examine the effect of wet coating–deposited TM phosphates on the electrochemical performance of $Li_{1.0}Ni_{0.8}$ $Co_{0.15}Mn_{0.05}O_2$ (NCM) positive electrode materials, anticipating a synergistic effect between the removal of Li residuals by their reaction with the coating material and protective layer formation during wet coating as shown in Figure 2.1.10. As a result, I demonstrate that surface modification can improve the capacity and cycling performance of NCM and effectively reduce the amount of Li residuals.

2.1.1.2 Filtering

Washing the active cathode materials with water is by far the most effective method to reduce the residual lithium content. However, factors such as the amount of water used for washing and the temperature used to dry the material after the washing process have a significant effect on the properties of the active material. Despite these impacts, no studies of the washing process, or of the relationship between residual lithium and gas evolution, have been reported.

In this study, I investigated the factors affecting the efficiency of the washing process for Ni-rich layered oxides. I studied the changes that occur at the surface of washed Ni-rich layered oxide cathodes, including the residual lithium layer.

2.1.2 Dry processes for OLO

The practical specific capacity of conventional positive electrode materials such as $LiCoO_2$ and $LiNi_{0.33}Co_{0.33}Mn_{0.33}O_2$ is less than 160 $mAh \cdot g^{-1}$, with the scarcity of high capacity alternatives explained by the complex bulk crystal structure of the host matrix enabling the high equilibrium potential of lithium (de)insertion at the positive electrode.[51,52] An example of a promising high-capacity (250 $mAh \cdot g^{-1}$) positive electrode material is presented by $xLi_2MnO_3 \cdot (1-x)LiMO_2$ (M = Ni, Mn, Co), or over-lithiated layered oxide (OLO), wherein Li2MnO3 exists as a nano-composite or solid solution within $LiMO_2$, with additional Li ions occupying transition metal sites, compared to conventional positive electrode having the layered structure. Recently, there have been new attempt to explain the unexpectedly large capacity of OLO by the reversible oxygen redox. Tarascon et al. have shown that the electrochemical reaction of oxygen redox is connected to coupling with structural evolution such as the formation of peroxide/superoxide-like species[53]. On the other hands, Chueh et al. have suggested that the local oxygen coordination associated with the transition metal

migration [54].

Although OLOs are considered to be promising positive electrode materials for next-generation LIBs due to exhibiting high energy densities, they suffer from several drawbacks, such as the occurrence of irreversible electrochemical reactions during initial charging, which need to be addressed prior to the practical application [55,56]. Since Mn ions in Li_2MnO_3 cannot be oxidized to compensate for Li removal, oxygen ions are oxidized to oxygen gas during first charging, which results in a part of released Li ions not being able to reversibly re-enter the positive electrode during discharge due to the structural change induced collapse of suitable lithium sites (Figure 2.3.1(a)). Moreover, side reactions between the OLO positive electrode surface and the electrolyte observed upon charging above 4.6 V lose the lithium ions during the charge process [57]. Although the above problems can be mitigated by employing surface modification agents such as Al_2O_3, AlF_3, carbon nano tubes, Li_2TiF_6, and $AlPO_4$, their applications result in specific capacity loss owing to the inertness for lithium ion reactions and decrease rate capability due to increasing positive electrode surface resistance as shown in Figure 2.3.8 [56,58]. For conventional LIBs, the low first coulombic efficiency greatly decreases the usable energy density, since after the first charging, a certain fraction of the active material cannot participate in (de)lithiation reactions for electrochemical energy storage. Therefore, the irreversibility of the first OLO cycle caused by oxygen gas evolutions induced

Li consumption can negatively affect capacity and cycling stability, which are important parameters determining the performance of all practical batteries [59].

$VOPO_4$, having an operating potential of 3.8 V, has not been extensively investigated as a positive electrode material due to not containing any lithium source, i.e., the positive electrode should feature a certain amount of lithium ion resources due to their absence at the graphite negative electrode [60]. Furthermore, the high potential of 3.8 V is beneficial to reserve the energy density of the positive electrode. $VOPO_4$ can provide sites for the insertion of Li that is otherwise irreversibly lost during OLO discharge (Figure 2.3.1(b)). Furthermore, it is well known that the PO_4^{3+} polyanion is highly thermally stable owing to the strong bond between P and O. In this view, the multi-functional coating of $VOPO_4$ was used to improve the first-cycle irreversibility, cycling stability, and thermal stability of OLO.

2.2 Experimental details

2.2.1 Sample preparation

2.2.1.1 Surface treatment with evaporation

NCM was synthesized by a co-precipitation method. Suitable amounts of Ni, Mn, and Co precursors (Ni/Co/Mn = 91:6:3) were dissolved in DI water, and a chelating agent (NH_4OH) along with a stoichiometric amount of NaOH solution were added to precipitate

$(NiMnCo)(OH)_2$ upon stirring. The precipitated $(NiMnCo)(OH)_2$ was ground with LiOH, and the obtained mixture was calcined at 750 ^oC in a flow of O2. The thus produced NCM powder was suspended in DI water, and the suspension was stirred for 20 min. The NCM powder mixture was dried at 120 ^oC and calcined at 700 ^oC for 5 h in a flow of O_2 (30 L min^{-1}). Figure 2.1.1 illustrates the TM phosphate coating process. The TM source was dissolved in DI water, followed by the sequential addition of NCM powder and a solution of $(NH_4)_2HPO_4$ (dropwise). The obtained mixture was stirred and concentrated to dryness at 80 ^oC, and the resulting coated NCM was heated at 720 ^oC for 5 h in a flow of O_2 (30 L min^{-1}).

2.2.1.2 Filtering

$Li_{1.0}Ni_{0.80}Co_{0.15}Mn_{0.05}O_2$ powder (NCM) was prepared by mixing co-precipitated $Ni_{0.80}Co_{0.15}Mn_{0.05}(OH)_2$ powder with $LiOH \cdot H_2O$ and calcining the mixture at 750^oC for 24 h in O_2. The washing process involved stirring NCM powder in deionized water with a mechanical stirrer for 10 min, followed by filtration within 5 min. The weight ratio between the NCM and the washing water was varied from 0.7:1 (powder/water) to 1:5 over 10 min. After washing and filtering, the water was removed by evaporation in an air convection oven at 80, 120, or 190^oC overnight. The residual moisture after overnight drying with different temperatures was confirmed by TGA (Figure 2.2.10). Following drying, heat treatment (HT) at 720^oC for 5 h in

flowing O_2 gas was applied to the powders.

2.2.1.3 Dry process

$VOPO_4$ was prepared by a reflux method as reported elsewhere [60]. Briefly, V_2O_5 (10 g, Aldrich) and H_3PO_4 (Aldrich, 60 mL, 85 vol.%) were refluxed in deionized water (240 mL) at 373 K for 24 h, and the obtained solids were filtered and sequentially washed with deionized water (200 mL) and acetone (200 mL, Aldrich). The obtained $VOPO_4 \cdot 2H_2O$ was refluxed in 2-butanol (150 mL, Aldrich) at 373 K for 18 h to afford a yellow powder of $VOPO_4 \cdot 0.5H_2O$, which was subsequently annealed at 773 K for 14 h and dried in vacuum at 393 K for 2 h. For nano-size $VOPO_4$, $VOPO_4$ particles were planetary milled, with 400 rpm for 24 h.

OLO powder (average particle diameter = 6 μm, $Li_{1.18}Ni_{0.17}Co_{0.1}Mn_{0.56}O_2$) was prepared by oxalate co-precipitation followed by 12-h annealing at 1173 K under ambient conditions [21,55]. The as-synthesized $VOPO_4$ was applied to OLO using mechanochemical coating(shown in Figure 2.3.9(a)) or simple mixing methods. In the former method, nano-size $VOPO_4$ was mechanically dry-coated onto OLO using a Nobilta mini mechanofusion system (Hosokawa Micron Corporation, shown in Figure 2.3.9(b)) operated for 30 min at 300W and 300 rpm. The latter method involved simple mixing of nano-size $VOPO_4$ and OLO powders using a pestle and an agate mortar.

2.2.2 Characterization

The materials were analyzed by XPS (Physical Electronics Quantum 2000 Scanning ESCA Microprobe spectrometer) using focused monochromatic AlKa radiation at 1486.6 eV as the X-ray source. The samples were etched for depth profile measurements by Ar^+ sputtering at 1 kV at intervals of 1 min. The elemental concentrations of Li, Mn, Co, and Ni in the NCM were determined by inductively coupled plasma-atomic emission spectrometry (ICP-AES) (Shimadzu ICPS-8100 sequential spectrometer). All samples were transferred under inert gas from the glove box to the analysis equipment using a specialized transfer vessel to avoid external contamination and oxidation. The changes in the surface morphology of the NCMs that resulted from the washing process and HT were imaged using SEM (Hitachi S-4700N). The washed and dried powders were analyzed by thermogravimetric analysis (TGA, TA Discovery) at temperatures of 30–210^{o}C in air. The residual lithium layers were observed directly by TEM (FEI Titan Cubed 60-300 equipped with Cs correctors) by dropping NCM particles onto a TEM grid directly, without any solvent. The amount of residual lithium was estimated by an acid–base titration method. The change in the pH value of the filtered water from the washing process was monitored during constant stirring while adding 0.1m HCl. Most of the observed Li content was expected to originate from Li_2CO_3 and LiOH, as these

species are also soluble in water [17,48]. The combined attributes of high spatial resolution (< 10 nm) and near-surface (< 50 A) chemical information makes AES a powerful tool for comprehensive surface analysis. AES measurements were performed in an ultrahigh vacuum (UHV, 1×10^{-8} Pa) chamber at room temperature using a Scanning Auger Microscope (SAM, ULVACPHI PHI 710) with a cylindrical mirror analyzer and field emission electron gun at an acceleration voltage of 10 keV. The powders were also examined using a ToF-SIMS surface analyzer (TRIFT V, Ulvac PHI, Japan) operated at a pressure of 10^{-9} Torr, equipped with liquid Bi^{+} ion source and pulse electron flooding. During the analysis, the targets were bombarded with the 30 keV Bi+ beams with a pulsed primary ion current of -1 pA. Differential scanning calorimetry (DSC) curves were recorded on an Auto Q20 instrument (TA Instruments). To prepare DSC samples, coin cells were charged to 4.6 V (vs. Li/Li^{+}) at 0.5C (1C = 230 $mA\cdot g^{-1}$) and disassembled to extract the charged positive electrodes that were sealed in the DSC pan and heated at a rate of 10 $^{o}C\cdot min^{-1}$.

2.2.3 Electrochemical measurements.

The electrochemical performance of the Ni-rich layered cathode materials was assessed in a CR2032 coin-type cell. The cell consisted of an NCM cathode and a lithium metal anode separated by a porous ceramic-coated polyethylene film. The composite cathode was fabricated by spreading a slurry consisting of the active material (92 wt.%), Denka black (4

wt.%), and polyvinylidene difluoride (PVDF) (4 wt.%) in N-methyl-2-pyrrolidone (NMP) on aluminum foil, which was used as the current collector. The electrodes were dried at 120 ^{o}C under vacuum and roll-pressed. The electrolyte solution consisted of LiPF6 (1.0 M) dissolved in a mixture of fluoroethylene carbonate (FEC) and dimethyl carbonate (DMC). All cell fabrication, including the slurry casting and assembly of coin cells, was conducted in a dry room.

The assembled cells were discharged/charged galvanostatically at a constant current. Three samples were tested for each variation of the preparation method, at a loading level of 10 mAh·cm^{-2}. The electrochemical activity of the cathodes was characterized by electrochemical impedance spectroscopy (EIS), using a Solartron 1260 frequency response analyzer with an applied frequency ranging from 10 mHz to 1 MHz. EIS measurements were performed in the initial state and the discharged state after one charge/discharge cycle.

Electrochemical performance of OLO cathode materials was evaluated using 2032 coin type cells comprising a composite electrode, metallic Li metal, a separator (Celgard), and an electrolyte (1.3M $LiPF_6$ in ethylene carbonate:diethyl carbonate:ethyl methyl carbonate (3:5:2 v/v, Panaxetec)). The composite electrode was prepared by casting a slurry of 86 wt% active material (either pristine or $VOPO_4$-impregnated OLO), 8 wt% Denka black, 6 wt.% polyvinylidenefluoride (PVDF, 6020, Solvay), and N-methylpyrrolidinone (NMP, Aldrich)

onto Al foil and thoroughly dried under vacuum at 120 ^{o}C before use.

Cylindrical-type 18650 cells were fabricated to analyze the long-term cyclability and quantify the evolution of gas from NCM/graphite full-cells. The electrochemical performance of the cylindrical-type 18650 cell was tested in a temperature-controlled chamber at 458C. The cells were cycled between 2.8 and 4.35 V at a rate of 1 C for up to 300 cycles. A specific capacity check was performed every 100 cycles during long-term cycling. A gas sampling system (Mulim Tech, shown in Figure 2.2.12) was used to measure the amount of gas generated in a cell. This system consisted of a vessel (with a cell jig and manifold) to contain the gas released by the cell, a pressure sensor to measure the amount of gas released into the vessel, and a vacuum pump to evacuate the apparatus (vessel and gas capture tube), both before and after measurement. After 300 cycles, the cell was put in the cell jig, and a vacuum was applied. The gases generated in the cell were then released into the vessel by puncturing the cell with a needle located at the top of the cell jig. The total amount of generated gas in the cell was calculated from the change in pressure and the known inner volume of each part of the apparatus using the ideal gas law. The composition of the released gas was analyzed using a refinery gas analyzer (RGA, Agilent Technologies 7890B model). The gas was moved to a gas capturing tube and then transferred to the RGA for composition measurements. A flame ionization detector (FID) was used to detect hydrocarbon components, and two thermal

conductive detectors (TCD) enabled the detection of other gases such as H_2, N_2, O_2, CO_2, and CO. The real amount of each gas component was calculated by integrating the peak of the RGA trace to find the peak areas. The measurements were compared against a calibration gas mixture with a known composition (Agilent P/N 5190-0519).

2.3 Results and discussion

2.3.1 Wet processes for Ni-rich layered oxides

2.3.1.1 Surface treatment with evaporation

Figure 2.1.2 compares the XRD patterns of pristine, Al/P-coated, Co/P- coated, and Fe/P-coated NCM (metal/P ratio = 1:1), with all observed peaks indexed to hexagonal a-$NaFeO_2$ (R3m space group). All coated samples showed well-defined characteristics with no impurity peaks matching that of the layered structure. The successful deposition of coating layers was confirmed by ICP-MS (Table 2.1.1) analysis, which revealed that the Li/Ni/Mn/Co ratio was nearly constant for all samples within the instrument tolerance, implying the absence of coating-induced composition changes. The XRD patterns of Co/P and Fe/P coated NCMs was similar to that of pristine. However, the reflections at ca. 65^o for Al/P coated NCM showed difference splitting. For better understanding, the rietveld analysis was conducted. The results were listed in Table 2.1.2. The Al/P coated NCM showed the change of lattice parameters. That

might be because some of Al was doped into NCM. The results of other samples were similar to pristine.

Figure 2.1.3 show SEM images of pristine, Al/P-, Co/P-, and Fe/ P-coated NCM samples with various TM/P ratios, with some particles covering the surface of pristine NCM ascribed to Li residuals (LiOH and Li_2CO_3). Island-shaped particles present on the surface of coated samples were believed to be composed of compounds produced by reactions between coating materials and Li residuals, as confirmed by the data in Table 2.1.3, which lists the amount of Li residuals determined by titration. Coating decreased the content of Li residuals in all samples, implying that these species reacted to form other compounds during this process, as demonstrated in our previous study [7]. Interestingly, NCM with P-rich coatings exhibited the lowest content of Li residuals, probably due to the ease of $LiPO_3$ and Li_3PO_4 formation [61,62]. Moreover, Al/P-coated NCM samples exhibited lower Li residual contents than other ones, which was correlated to the lower formation energies of $LiAlP_4O_{12}$ and $AlPO_4$ compared to those of other transition metal compounds [7]. The film-shaped coating layer was uniform, having a thickness of ~20 nm (Figure 2.1.4). The coating layer was not clearly distinguishable from NCM, but is uniformly coated on the surface. SEM imaging revealed that P-rich NCM coatings featured smoother primary particles than other ones, implying that thicker coating material was covered on NCM powder because of formation of Li/P compound by reaction

with Li residuals, as indicated by the corresponding Li residual contents. Coated NCM samples were further characterized by XPS, with their Al 2p, Co 2p, Fe 2p, and P 2p spectra shown in Figure 2.1.6 (a)–(f). The non-shifted binding energies of major peaks indicated that the ion structural environment was unaffected by the coating process. Al 2p spectra featured strong Al_2O_3 peaks at 73.9 eV, and Co and Fe spectra showed peaks of Co_3O_4 (779.7 eV) and Fe_2O_3 (712 eV), respectively. In addition, the prevalence of metal oxide states increased with increasing metal content of the coatings, with these oxide peaks ascribed to compounds produced by reactions between Li residuals and TMs (e.g., $LiAlO_2$ and $LiCoO_2$) or between Li residuals and TM/P (e.g., $LiCoPO_4$ and $LiFePO_4$). The possibility of formation of TM/P on the positive electrode surface was reported in previous our group [7]. The results in reference showed that formation of lithium phosphate and lithium transition metal phosphate by reaction between Li residuals and coating material was energetically preferred reaction [7]. The peak at 133.5 eV observed in P 2p spectra (Figure 2.1.6) was assigned to PO_4, possibly originating from Li_3PO_4 formed by the reaction of Li residuals with P and P_2O_5 [62]. According to a previously calculated study, it is judged that the outermost layer with the surface by metal phosphate treatment is compound of $LiCoPO_4$, Li_3PO_4 and CoO as shown in Figure 2.1.11 [7].

Figure 2.1.7 compares the cycling performances of cells based on various active materials determined at 25 ^oC and a charge/ discharge rate of 1C (1.75 mA cm^{-2}). Cycling tests were

performed after rate performance evaluation, with the results listed in Table 2.1.4. All coated NCM samples showed higher initial capacities and coulombic efficiencies, which was ascribed to the increase of electrical conductivity due to the removal of Li residuals [63]. The capacity of these samples at high current density was also increased, despite the small gap. However, the capacity retention upon cycling was significantly enhanced compared to capacity itself. In particular, Al/P-coated NCM samples showed very high capacity retention, probably due to the increased chemical stability of Al-containing compounds such as Al_2O_3, whereas no capacity increase was concomitantly observed. Fe/P-coated NCM showed a performance similar to that of pristine NCM. Capacity retention was not increased when P-rich TM/P coatings were used, probably due to the occurrence of side reactions at the NCM surface caused by the formation of P_2O_5 from P, which might offset the electrochemical performance increase induced by the removal of Li residuals. However, enhanced capacity retention was observed in the case of TM-rich coatings due to the presence of inert oxide materials. Considering the removal of Li residuals in addition to capacity and capacity retention, a 1:1 Co/P coating proved to be most effective for surface modification. To further elucidate the effect of the above coating, it was applied to the more Ni-rich $Li_{1.0}Ni_{0.91}Co_{0.06}Mn_{0.03}O_2$ (h-NCM), with its loading increased to 2 wt% due the expected large amount of Li residuals. Figure 2.1.8 compares the cycling performance of pristine and Co/P-coated h-NCM cells at 25 ^oC and a charge/discharge rate of

1C. SEM imaging confirmed that h-NCM was well covered by the Co/P coating, as shown in Figure2.1.5. Fig. 2.1.7 further reveals that Co/P-coated h-NCM cells exhibited a larger capacity retention (86.3%) than those based on pristine material (65.4%), additionally featuring the advantage of increased initial capacity (by 12 mAh g^{-1}). This behavior might be due to the formation of $LiCoPO_4$ and the removal of Li residuals, in line with the results observed for NCM cells (see Figure 2.1.6). Thus, it was confirmed that the Co/P coating of NCM rich in Li residuals improved the electrochemical performance of the corresponding cells.

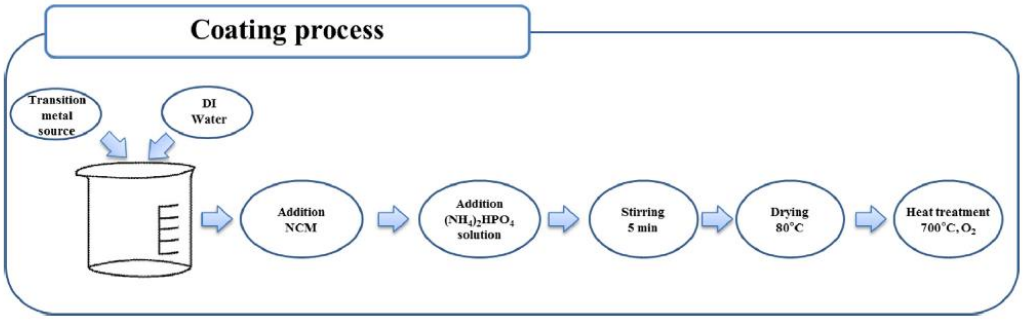

Figure 2.1.1 Schematic flow of the coating process based on evaporation.

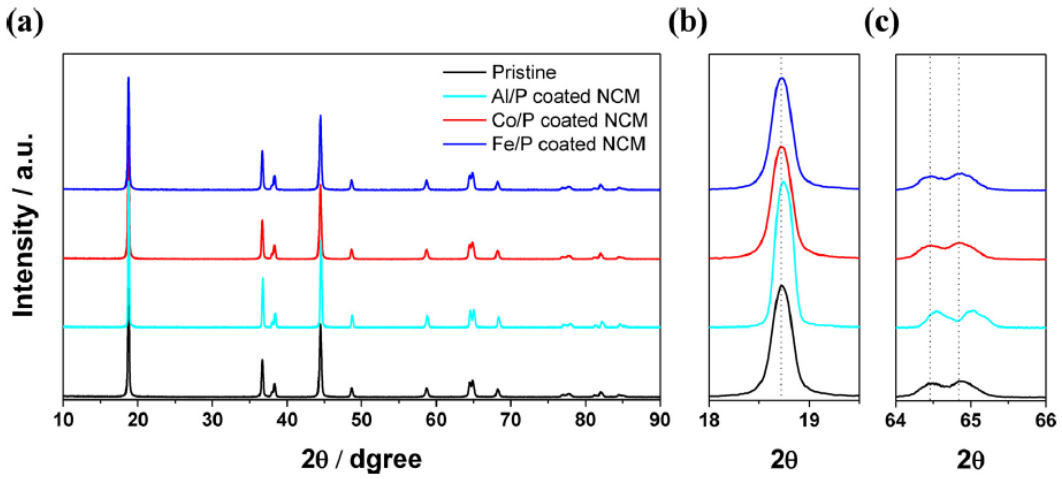

Figure 2.1.2 (a) XRD patterns of NCM and TM/P-coated NCM and (b)-(c) enlarged XRD peaks

NCM sample	Mole ratio						
	Li	Mn	Co	Ni	Al	P	Fe
Pristine	1.04	0.100	0.099	0.801	0.0000	0.0000	0.0000
Al/P-coated	1.03	0.099	0.099	0.796	0.0009	0.008	0.0000
Co/P-coated	1.04	0.099	0.101	0.794	0.0000	0.008	0.0000
Fe/P-coated	1.04	0.100	0.099	0.792	0.0000	0.008	0.0009

Table 2.1.1 ICP-AES analysis results of pristine and TM/P-coated NCM samples.

NCM sample	Space Group	*a* (nm)	*c* (nm)
Pristine	*R*-3*m*	0.2871	1.4198
Al/P-coated	*R*-3*m*	0.2866	1.4185
Co/P-coated	*R*-3*m*	0.2872	1.4200
Fe/P-coated	*R*-3*m*	0.2873	1.4200

Table 2.1.2 Rietveld analysis results for the pristine NCM and coated NCM samples.

Metal : Phosphorus	1 : 0.5	0.5 : 1	1 : 1	1 : 0
Al	b	c	d	e
Co	f	g	h	i
Fe	j	k	l	m

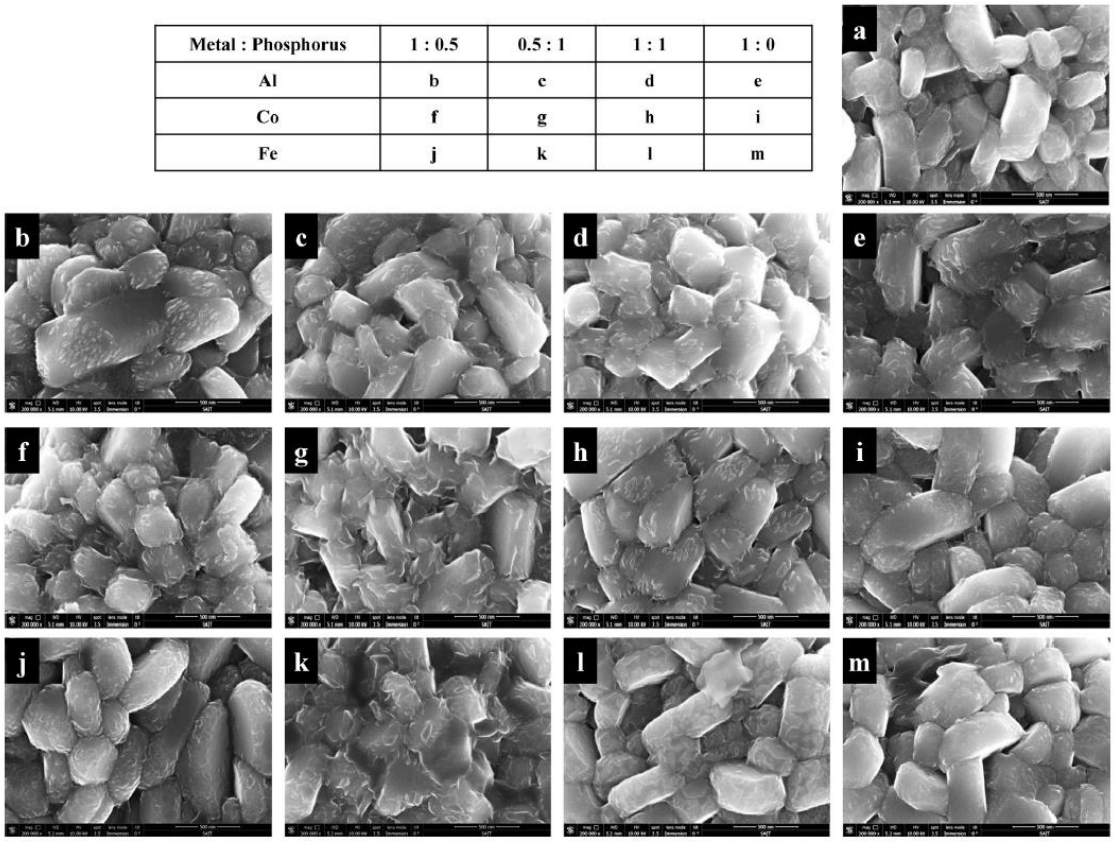

Figure 2.1.3 SEM images of pristine and TM/P-coated NCM with various TM/P ratios (a) NCM, (b)–(e) Al/P-coated NCM, (f)–(i) Co/P-coated NCM, (j)–(m) Fe/P-coated NCM.

		Li_2CO_3 (ppm)	LiOH (ppm)	Total (ppm)*
Pristine		9561	6555	3693
Al/P-coated	1:0.5	4002	4443	2037
	0.5:1	4255	4423	2079
	1:1	9849	5438	2297
	1:0	6616	4726	2610
Co/P-coated	1:0.5	4010	6002	2490
	0.5:1	3312	5238	2151
	1:1	3814	5546	2321
	1:0	6263	5816	2859
Fe/P-coated	1:0.5	5078	5578	2568
	0.5:1	3924	5177	2235
	1:1	4409	5311	2365
	1:0	6240	5669	2813

*-

$$\text{Total Li}(ppm) = \frac{Atomic\ weight\ of\ Li}{molecular\ weight\ of\ Li_2\ CO_3} \times Li_2\ CO_3\ (ppm) + \frac{Atomic\ weight of\ Li}{molecular\ weight\ of\ LiOH} \times LiOH(ppm)$$

Table 2.1.3 Content of Li residuals in pristine and TM/P-coated NCM samples with various TM/P ratios.

		1st cycle (0.1C)		Discharge rate @ 0.5C charge			Capacity retention (%) @ 50th cycle
		Charge ($mAh\,g^{-1}$)	Discharge ($mAh\,g^{-1}$)	0.2C ($mAh\,g^{-1}$)	1C ($mAh\,g^{-1}$)	2C ($mAh\,g^{-1}$)	
Pristine		223.38	209.82	206.48	191.69	189.07	90.91
Al/P-coated	1:0.5	223.98	207.32	204.18	190.45	187.18	93.0
	0.5:1	222.54	208.3	205.39	191.7	188.1	90.84
	1:1	222.38	208.72	205.55	192.0	188.04	92.6
	1:0	222.9	206.19	203.87	189.2	186.02	92.83
Co/P-coated	1:0.5	224.0	209.78	207.67	195.23	188.91	91.39
	0.5:1	224.03	208.35	205.24	192.61	187.85	91.2
	1:1	222.76	208.87	206.08	194.96	189.75	92.46
	1:0	223.37	209.13	206.2	193.28	187.75	91.14
Fe/P coated	1:0.5	223.25	208.57	205.11	190.20	187.18	91.37
	0.5:1	222.96	207.51	204.26	191.1	186.32	91.12
	1:1	223.88	207.48	204.37	191.78	187.39	90.86
	1:0	224.11	207.72	204.48	191.63	187.5	91.3

Table 2.1.4 Electrochemical performances of pristine and TM/P-coated NCM samples with various TM/P ratios.

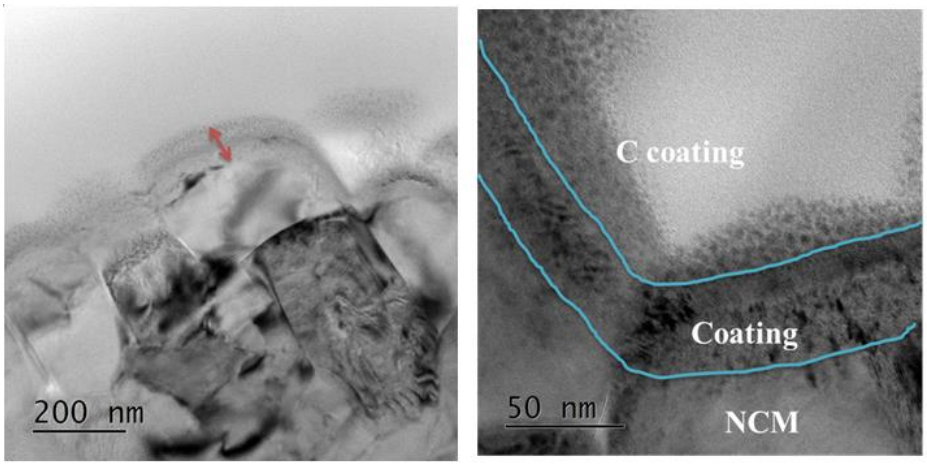

Figure 2.1.4 TEM image of *Tm*/P coated NCM

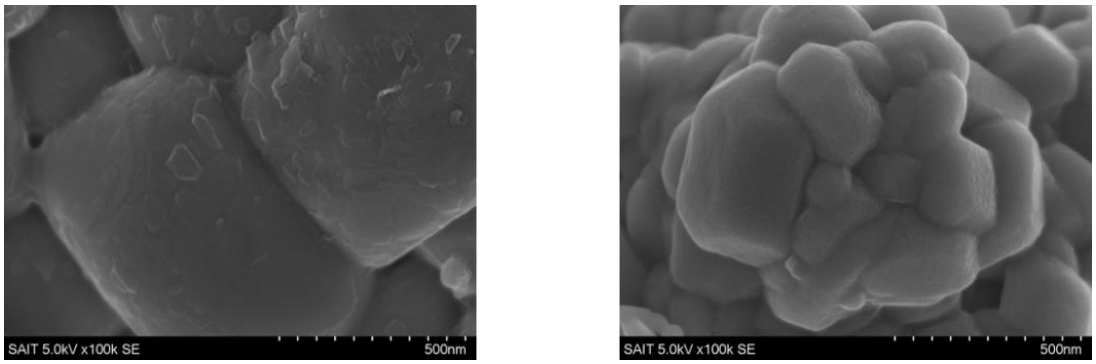

Figure 2.1.5 SEM images of Co/P coated h-NCM

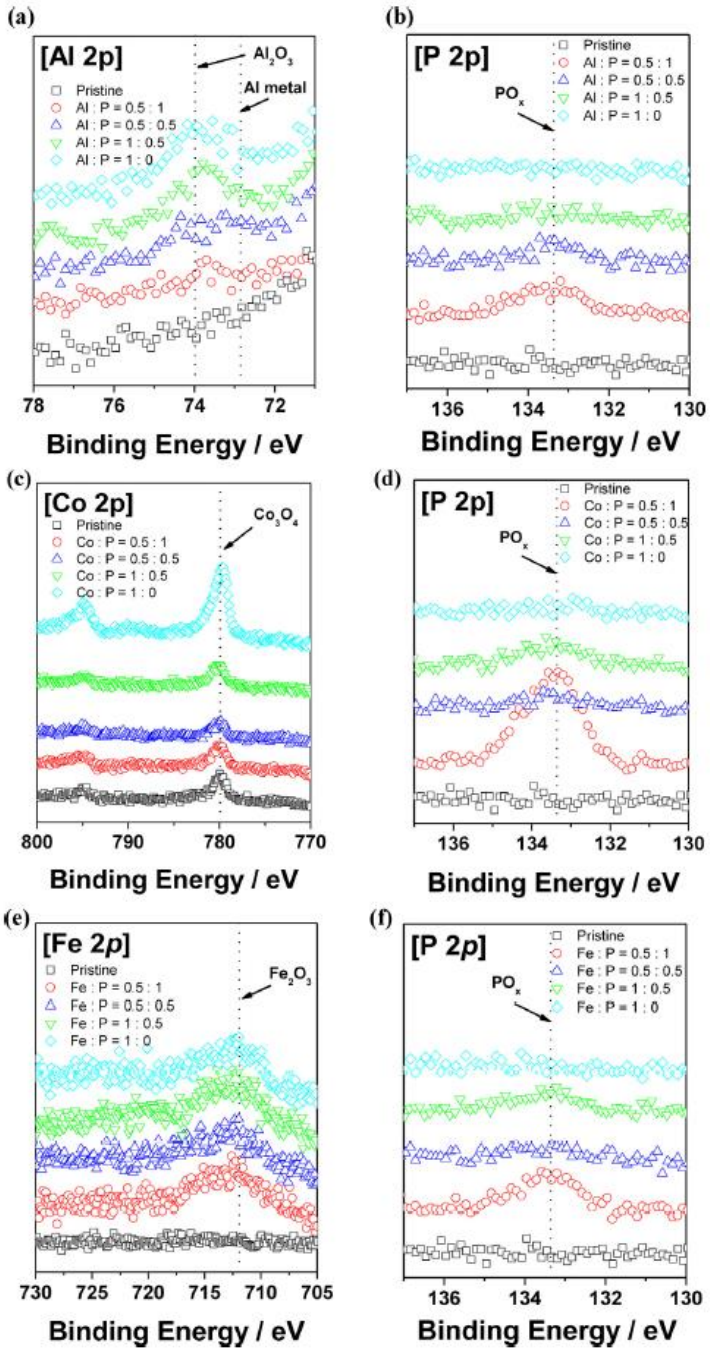

Figure 2.1.6 (a) Al 2p and (b) P 2p XPS spectra of Al/P-coated NCM; (c) Co 2p and (d) P 2p XPS spectra of Co/P-coated NCM; (e) Fe 2p and (f) P 2p XPS spectra of Fe/P-coated NCM.

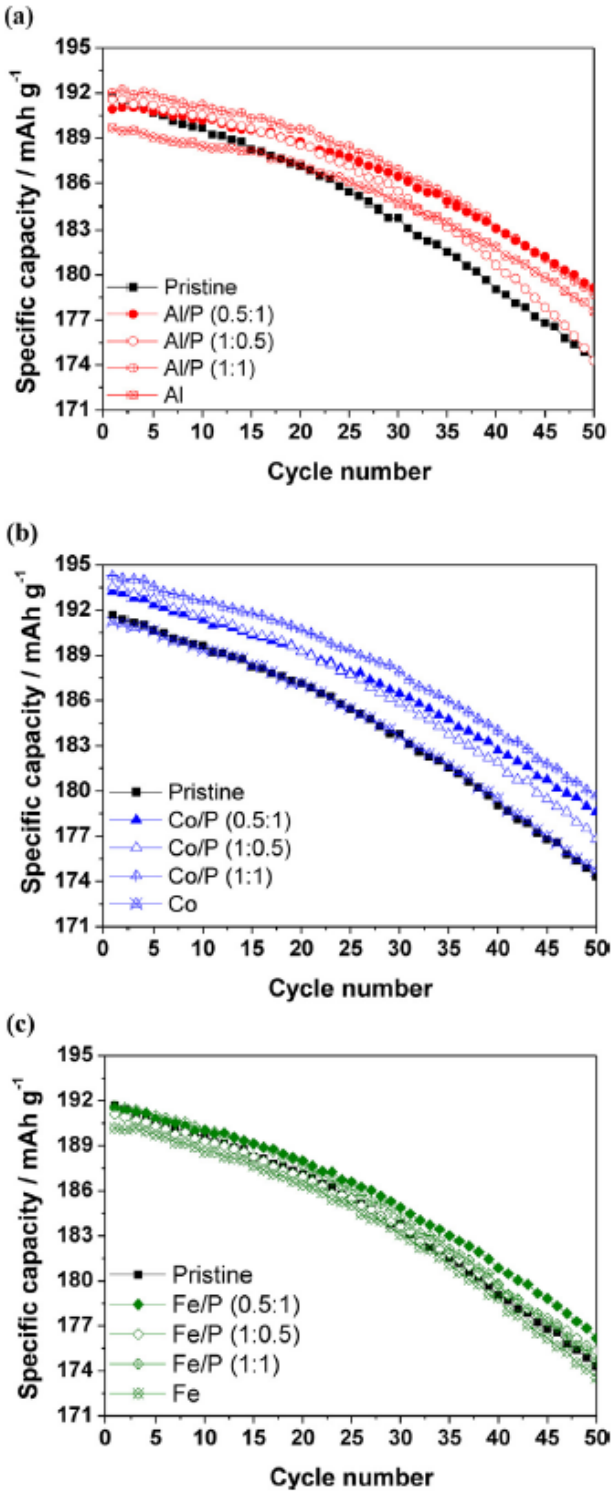

Figure 2.1.7 Cycling performances of pristine and TM/P-coated NCM samples with various TM/P ratios (a) Al/P coated NCM (b) Co/P coated NCM (c) Fe/P coated NCM.

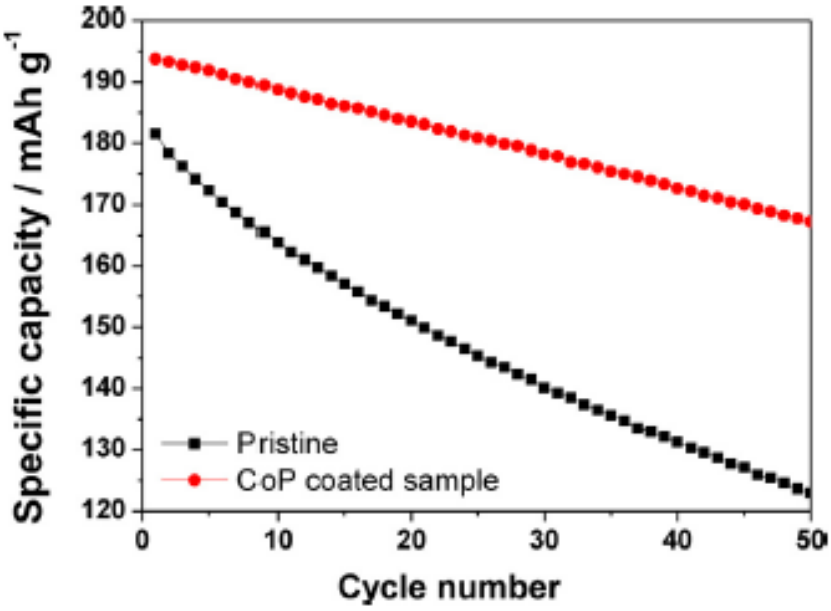

Figure 2.1.8 Cycling performances of pristine and Co/P-coated h-NCM samples.

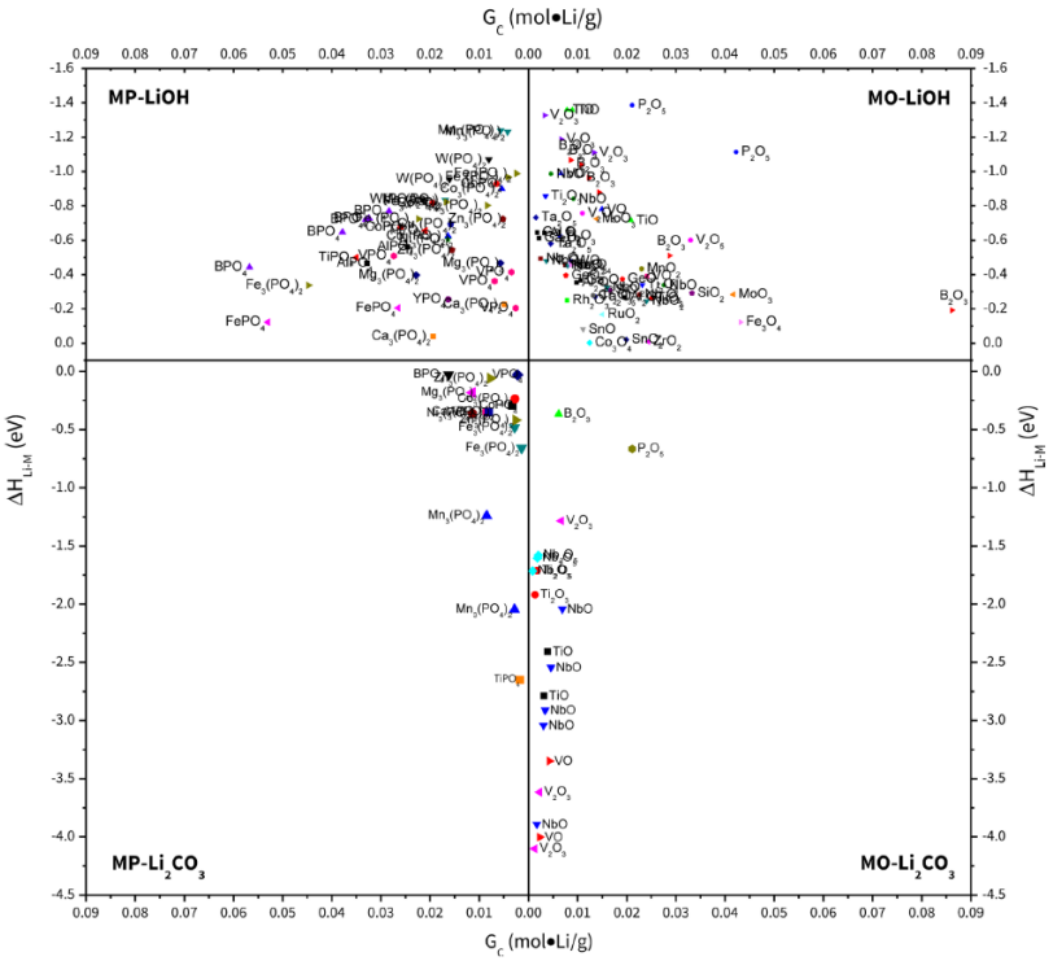

Figure 2.1.9 Overall design chart for the reaction between MP/MO and LiOH/Li_2CO_3.[7]

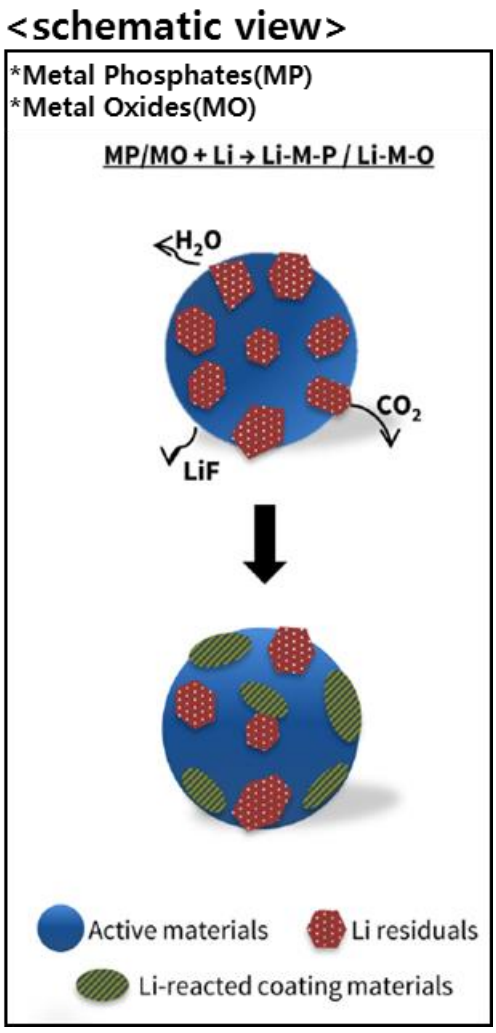

Figure 2.1.10 A schematic view of removing residual lithium at the surface of the cathode materials during the surface treatment[7].

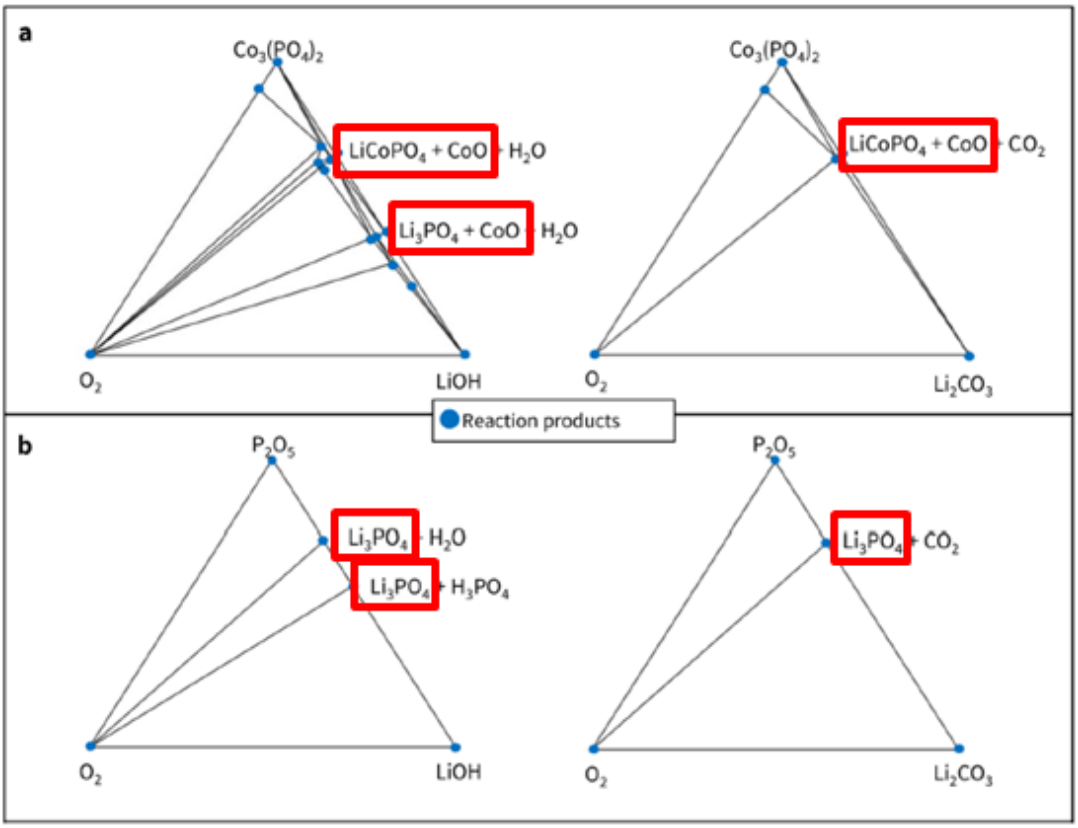

Figure 2.1.11 Phase diagram for (a) $Co_3(PO_4)_2$−LiOH/Li_2CO_3−O_2 and (b) P_2O_5−LiOH/Li_2CO_3−O_2[7].

2.3.1.2 Filtering

The effects of varying the amount of water used to wash the NCM materials were investigated first. Figure 2.2.1 shows the electrochemical performance and residual lithium content for different weight ratios of active material to water, which were varied from 0.7:1 to 1:5.0. Figure 2.2.1(a) shows that the initial capacity loss increased from 1 to 3 mAh/g as the amount of water used increased. Furthermore, the capacity retention after 50 cycles, as compared with the initial capacity, dramatically diminished as the amount of water used increased. The excessive use of water for washing can cause unexpected changes in the active material, such as leaching of lithium ions from the NCM lattice. NCM lattice is influenced by excessive washing water, and this have effect on the (003) peak position and c-axis parameter owing to variation of the interlayer distance as shown in Figure 2.2.8. (003) peak position slightly shift to lower two-theta and the lattice parameter c-axis is increasing with washing water amount because excessive water amount leach lithium from NCM lattice. On the other hand, the use of a greater amount of water produces a greater lithium concentration gradient between the surface of the active material and the water which based on Fick's first law for diffusion[64]. Furthermore, the use of less water can lead to rapid saturation of the washing water with dissolved lithium. Previous reports also have suggested that the frequency and duration of the interactions between the active materials and water have a strong influence on

the surface and bulk structures of the active materials[17,65]. The use of water in amounts greater than twice the mass of the NCM (1:2 NCM to water) caused a severe decrease in the capacity retention. The electrochemical performance and the amount of residual Li suggested that ratios of 0.7:1 or 1:1 of NCM to water were optimal for these materials. Figure 2.2.1(b) shows that a residual lithium concentration of less than 1000 ppm can be achieved even when the material is washed with a small amount of water, which avoids the loss of capacity retention. In addition, clear surface of NCM without lithium impurities by washing can be also observed in Figure 2.2.9 (b-d) compared to the bare in Figure 2.2.9 (a). As shown by the ICP-mass spectrometry data in Table 2.2.2, the chemical composition of the Ni, Co and Mn remained mostly unchanged while lithium gradually decreased with increasing water amount. Overall, these results show that an excess of water lowers the efficiency of the washing process because the small amount of water such as the ratio of 0.7:1 or 1:1 of NCM to water can effectively remove residual lithium with minimizing the capacity loss. However, the use of less water than the mass of the active material led to difficulties when scaling up the process; these circumstances cause a lack of homogeneous mixing with associated reproducibility problems. Therefore, a ratio of water to NCM of 1:1 is proposed to be optimal.

Examination of the freshly washed surface revealed that the residual lithium layer was reformed during drying in a convection oven through contact with air and moisture. The drying

temperature affects the extent to which the residual lithium layer reformed on the surface, and is thus relevant to the electrochemical performance and gas evolution of the cell. The surface morphologies of submicron-sized particles of NCM materials that were either bare (not treated with the washing or HT processes) or had been washed and dried at various temperatures (80, 120, 190 ℃) and the following HT processes were investigated by SEM, as shown in Figure 2.2.2. The noticeable differences between the surface morphologies of the bare material (Figure 2.2.2(a)), the material after washing and drying (Fig. 2.2.2(b)-(d)), and the post heat treatment (HT) powder (Figure 2.2.2(e)-(g)) were mainly due to the varying presence of the residual lithium layer on the surface of the active materials.

The surface morphology of the bare sample showed primary particles that were covered by irregular thickness and scattered impurities, which are suggested to be residual lithium layer. Figure 2.2.2(b)-(d) show NCM particles that were treated by the washing and drying processes; the edges of the primary particles appear sharp and cleanly defined, which suggests that the residual lithium layer has been removed.

The presence of the nanoscale spheroid impurities on the surface of the primary particles decreased as the drying temperature was increased from 80 ℃ (Figure 2.2.2(b)) to 120 ℃ (Figure 2.2.2(c)) and 190 ℃ (Figure 2.2.2(d)). A change in the surface morphology was seen in particles that underwent the HT process (Figure 2.2.2(e)-(g)). The particles that underwent the

HT process were covered by a greater amount of rough surface layer than the non-heat treated powder (Figure 2.2.2(b)-(d)), which suggests that the layer was caused by the reformation of a residual lithium layer during the HT process. The SEM images indicate that the particles of powders that were dried at a lower temperature (80 ℃) and underwent HT were covered by a smooth surface layer; while those dried at higher temperatures (120 ℃ and 190 ℃) were covered by a rough surface layer with more closed to islands-type of impurities. The length of time that the active material is exposed to water is much greater when it is dried at 80 ℃ compared to drying at higher temperatures (120 ℃, 190 ℃); this increased exposure time can result in increased lithium leaching from the bulk to the surface. Thus, the use of drying temperatures below the boiling point of water causes these changes in morphology. The effects of drying temperatures above and below the boiling point of water are also shown by the TGA analysis in Figure 2.2.10. The samples for TGA analysis did not undergo the HT process. Furthermore, weight loss differences between the different drying temperature means the residual moisture content of the powder. The materials dried at temperatures of 120 ℃ and 190 ℃ showed similar weight loss curves, owing to their different moisture contents. However, the weight loss of the material dried at 80 ℃ was greater (about 0.4 wt.%) than the powder dried at 190 ℃ (less than 0.2 wt.%) at 200 ℃ of TGA. This TGA result showed that the materials dried at temperatures above the boiling point of water had similar moisture contents,

while those dried at lower temperatures retained more moisture. The relationship between the residual lithium content and the drying temperature and HT process could be demonstrated by the residual Li contents of each material, as shown in Table 1. These data showed that the residual Li was effectively reduced by all the washing and post-HT processes. These processes removed LiOH more effectively than Li_2CO_3, as shown by the titration data in Table 2.2.3. This selectivity is attributed to the higher solubility of LiOH in water (12.8 g per 100 mL) compared with Li_2CO_3 (1.3 g per 100 mL) at room temperature.[53] Although the powders were assumed to have the same residual lithium content directly after washing, the residual lithium content was gradually reduced for the non-heat-treated materials with increasing drying temperatures. The moisture content of the freshly washed and filtered powder was less than 0.4 wt.% from the TGA (Figure 2.2.10), which is enough to leach lithium from the layered structure.

The presence of residual lithium was reduced after HT at 720 ℃ in O_2, because the NiO layer was re-oxidized and could then react with residual lithium species during the HT process. The materials dried at lower temperatures showed greater reductions in their residual lithium content than those dried at a higher temperature. Since a relatively large amount of lithium can be re-inserted into the bulk structure after leaching, the capacity loss may be caused by re-insertion of intermediate phases such as $LiNiO_2$ [66,67].

The leaching of lithium from the bulk structure has a strong effect on the crystal structure at the NCM surface, as well as its surface morphology. The cation-disordering effects of leaching were evident from the X-ray diffraction (XRD patterns) of bare and washed samples before and after HT, as shown in Figure 2.2.11; these did not show any secondary phases or significant changes except for slight changes in peak intensities. All washed samples had an I(003)/I(104) intensity ratio that was greater than 1.4[40,68]. The amounts of Li_2CO_3, which was used to indicate residual lithium and oxygen from the NCM lattices ($O_{lattice}$) that were present throughout the active material, were investigated by XPS depth profiles; the results are shown in Figure 2.2.3. The thickness and the distribution of the residual lithium layer were inferred from the changes in the relationship between the peak intensities for these species with depth. Two main peaks were observed in the O 1s XPS spectra shown in Figure 2.2.3(a)-(g). The peak at the lower binding energy of 528.8 eV was assigned to the $O_{lattice}$, and the peak at the higher binding energy of 531 eV was assigned to residual lithium species, such as Li_2CO_3 and LiOH[69,70]. The intensities of these peaks changed as Ar^+ sputtering proceeded and the depth at which measurements were taken increased. All the washed samples (Figure 2.2.3 (b)-(d)) showed the dramatic decrease in the residual lithium peak intensity compared to the bare, while the corresponding $O_{lattice}$ peaks showed little change. The residual lithium peak intensity of the samples dried at 120 ℃ and 190 ℃ (Figure 2.2.3 (c), (d)) was consistently lower than

that of the $O_{lattice}$ peak for all the depth profiles. This result indicates the effective removal of residual lithium, and confirms the findings from the SEM (Figure 2.2.2(b)-(d)) and residual lithium titration (see the "Before HT" row of Table 1) analyses. The residual lithium peaks of the samples that were measured after HT (Figure 2.2.3(e)-(g)) dramatically increased, while the corresponding $O_{lattice}$ peaks decreased. This is also similar result from the SEM (Figure 2.2.2(e)-(g)) that reformation of the residual lithium layer during HT process. The high intensities of the residual lithium peaks in samples that were dried at 80 ℃ significantly decreased with increasing depth. It is expected that the surface region contains a higher distribution of residual lithium in the outermost layer, but a thinner residual lithium layer, compared with the other drying conditions, as suggested by the reduced residual lithium content seen in the titration data for this sample (Table 2.2.1, after HT).

The sample surface morphologies were further analyzed by TEM to investigate the residual lithium distribution, the thickness of the residual lithium layer produced by different drying conditions, and the effects of HT. The presence of impurity layers was noticeable on the surface of the active material, and the impurities varied in shape depending on the different drying and post-treatment conditions. The layer on the surface of the active material was assigned as residual lithium. Its thickness was 10–100 nm; it appeared to be inhomogeneous and porous, and showed a lower contrast than the active materials. This observation suggests

that the constituent elements of the layer are of low density, for example, Li, C, and O. This residual lithium layer on the surface of the NCM was rapidly damaged under the electron beam and disappeared quickly, requiring images to be taken quickly and at low magnification. The thickness of the amorphous layer varied slightly with drying temperature and following HT. as shown in Figure 2.2.4(b)-(d), the amorphous layer assigned as residual lithium was still present on the NCM surface after the washing and drying processes. This finding is in agreement with earlier conclusions that, although impurity particles regarding residual lithium are effectively removed by the washing and drying processes, the residual lithium layer is reformed on the outermost layer after drying because of leaching during drying. Samples dried at 80 ℃ had a more uniform residual lithium layer, with a thickness of 50–100 nm, which is thicker than that seen at the higher drying temperatures. After HT, the residual lithium layer was thinner and more uniform than in the dried samples, as shown in Figure 2.2.4 (e)-(f). The sample dried at 80 ℃ followed by HT (Figure 2.2.4 (e)) showed a uniformed surface layer.

The results of SEM, XPS, titration, and TEM analyses were used to suggest a process for the observed changes in the surface layer in response to washing, drying, and HT, as shown schematically in Figure 2.2.5. The initial state of the material is depicted in Figure 2.2.5(a) as a cross-section of the bare surface covered by residual lithium species, including LiOH and Li_2CO_3. Most the LiOH species in the residual lithium layer were removed by washing (Figure

2.2.5(b)), from the results of SEM, XPS and its 10 times higher water solubility compared to Li_2CO_3. Meanwhile, shown in Figure 2.2.8, some of the lithium leached from the bulk structure reacted with atmospheric CO_2 to form additional Li_2CO_3 during drying.[65] Most of the residual lithium on the surface was activated during HT at 720 ℃, which was a high enough temperature for LiOH and Li_2CO_3 melt to react with surface layer of NCM (Figure 2.2.5(c)) [71]. Some of the lithium leached from the bulk structure by washing and drying were recovered into the bulk at this stage. A Li_2CO_3 layer was expected to reform by reaction with atmospheric CO_2 in the furnace at first, followed by the formation of LiOH through reaction with moisture during cooling after HT due to their different melting temperature (Figure 2.2.5(d)).

The electrochemical performances of the bare, post heat treated samples after various temperatures drying are shown in Figure 2.2.6. All dried and HT samples adopted the ratio of water to NCM is 1:1. The charge/discharge voltage profiles of the initial cycle at a rate of 0.1 C are shown in Figure 2.2.6(a). The Coulombic efficiency of the initial cycles of HT after the washed and dried samples (89.5% to 92.4%) was lower than for the bare materials (93.2%). The HT samples dried at 80 ℃ showed a larger polarization during initial charging (~3.58 V) and at the end of discharge (~3.49 V), owing to their high resistance. The reconstruction of the residual lithium layer during the post heat treatment processes thus affects the resistance of the

material. I propose that the reconstructed residual lithium, which mainly consists of a dense layer of Li_2CO_3. This residual lithium changes to porous LiF by the following pathway, when it encounter the lithium salt of the electrolyte such as $LiPF_6$ in the cells.[72]

$$LiPF_6 + Li_2CO_3 \rightarrow POF_3 + CO_2 + 3LiF$$

LiF is a well-known protective coating material with high resistance,[19,73–77] and this product covers the NMC surface after charging. The cycling performances of the bare, washed, and dried samples were also measured at 1C, as shown in Figure 2.2.6(b). All washed samples showed a lower initial cycle capacity and their capacity retention rate (CRR) also gradually decayed. Samples dried at 80 ℃ showed good CRRs. Thus, the homogeneous and dense residual lithium layer shown by our previous analyses to form for samples dried at 80 ℃ contributes to the formation of a protective LiF coating. Samples dried at 120 ℃ nevertheless had the highest discharge capacities during 50 cycles among the washing samples.

EIS tests were performed for bare and washed NCM electrodes after drying at various temperatures to further investigate the effects of drying temperature. The impedance of a two-electrode coin cell was measured before and after the first cycle; the EIS plots and corresponding circuits are depicted in Figure 2.2.6(c). The measured EIS spectra were interpreted by considering three elements of the charge/discharge process. The DC resistance (R_s in the equivalent circuit) mainly arises from the resistance of the electrolyte. The

impedance in the high-frequency region, which corresponds to the Li-ion migration resistance (R_{sf}), is related to the impedance to Li-ion migration through the solid electrolyte interphase (SEI) film. The impedance in the intermediate-frequency region, i.e., the charge transfer resistance (R_{ct}), is related to the charge transfer at the cathode/electrolyte interface and the interfacial capacitance at the electrode/electrolyte interface. The impedance in the low-frequency region is attributed to the migration of Li^+ ions by diffusion through the electrolyte, a phenomenon referred to as Warburg impedance.

The impedance spectra of the samples appeared as a single semicircle, which was formed from two merged semicircles, as shown in Figure 2.2.6(c). Most of the impedance of the semicircle could be modeled by the element R_{ct}. After the initial cycle, all washed NCM materials showed smaller radii for the first semicircle than did the bare sample. This behavior was seen because the residual lithium layer that reformed after the washing process became a low-resistance layer during the first cycle. This transformation is attributed to the activation of NCM during cycling, as the electrolyte diffuses into the cathode material. However, the reduction in radii of the semicircles was caused by the suppression of the reaction between the cathode and the electrolyte by the thin, uniform residual lithium layer formed in all the washed samples (as shown in Figure 2.2.4), as well as by the decline of the resistive layer caused by residual lithium.

A comparison of the full cell cyclability and gas evolution of the cylindrical-type 18650 cells is shown in Figure 2.2.7. Samples were treated with the optimal washing (1:1 ratio of NCM to water) and HT after drying (temperature of 120 ℃) conditions, as determined by our electrochemical performance due to its highest discharge capacity among the samples after 50 cycles. As shown in Figure 2.2.7(a), the CRR of the washed material (86.1%) was slightly improved compared with the bare material (84.6%), which was the opposite effect to that found in the coin-type half cells shown in Figure 2.2.1(a) and Figure 2.2.6(b). Unlike the coin-type half cell, the cylindrical-type 18650 cell was strongly affected by gas evolution during cycling. The cylindrical-type 18650 cells were tested for longer cycles and at a higher temperature (45 ℃) with more electrolyte than the coin-type half cells, and these factors can accelerate gas evolution. The volume of gas evolved from a cylindrical-type 18650 cell was measured by RGA over 300 cycles; the results are shown in Figure 2.2.7(b). The total amount of gas evolution was reduced by 25% for washed samples (3.3 mL/g) compared with bare samples (4.4 mL/g). The evolution of CO and CO_2 from Li_2CO_3 were reduced by washing, while the evolution of other gas species was unaffected.

The main components in the generated gas at high temperatures for NCM with free lithium compounds were CO and CO_2.[35,78] The mechanism of CO and CO_2 generation is as follows:

$$2LiOH + LiPF_6 \rightarrow 3LiF + POF_3 + H_2O \qquad (1)$$

$$LiPF_6 \rightarrow LiF + PF_5 \quad (2)$$

$$PF_5 + H_2O \rightarrow POF_3 + 2HF \quad (3)$$

$$Li_2CO_3 + 2HF \rightarrow 2LiF + H_2O + CO_2 \quad (4)$$

$$2CO_2 + 2Li^+ + 2e^- \rightarrow Li_2CO_3 + CO \quad (5)$$

The formation of water from LiOH leads to the production of HF by hydrolysis of the electrolyte. Then, CO_2 is evolved from the reaction between HF and Li_2CO_3. Subsequently, the generated CO_2 can react with lithium to produce Li_2CO_3 and CO gas.[35,53,70]

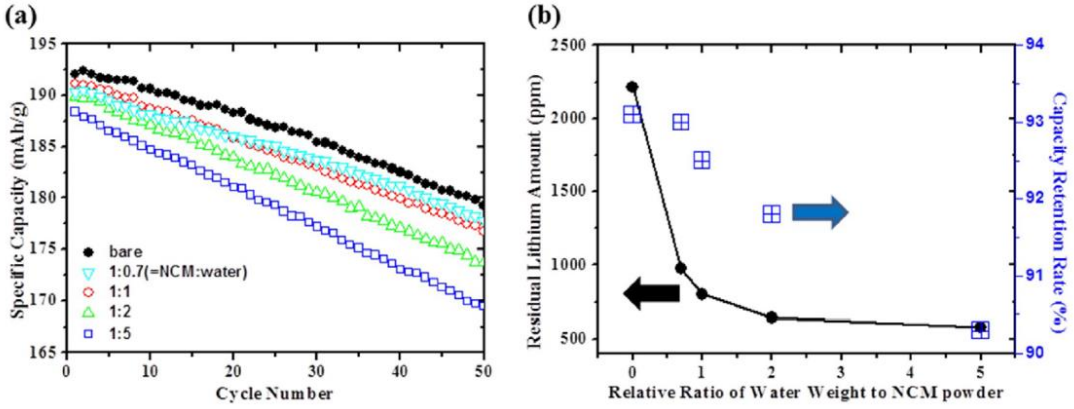

Figure 2.2.1 (a) Plot of the discharge capacity vs. cycle number for coin-type half cells. (b) Plot of the residual lithium and capacity retention vs. the amount of water used for washing

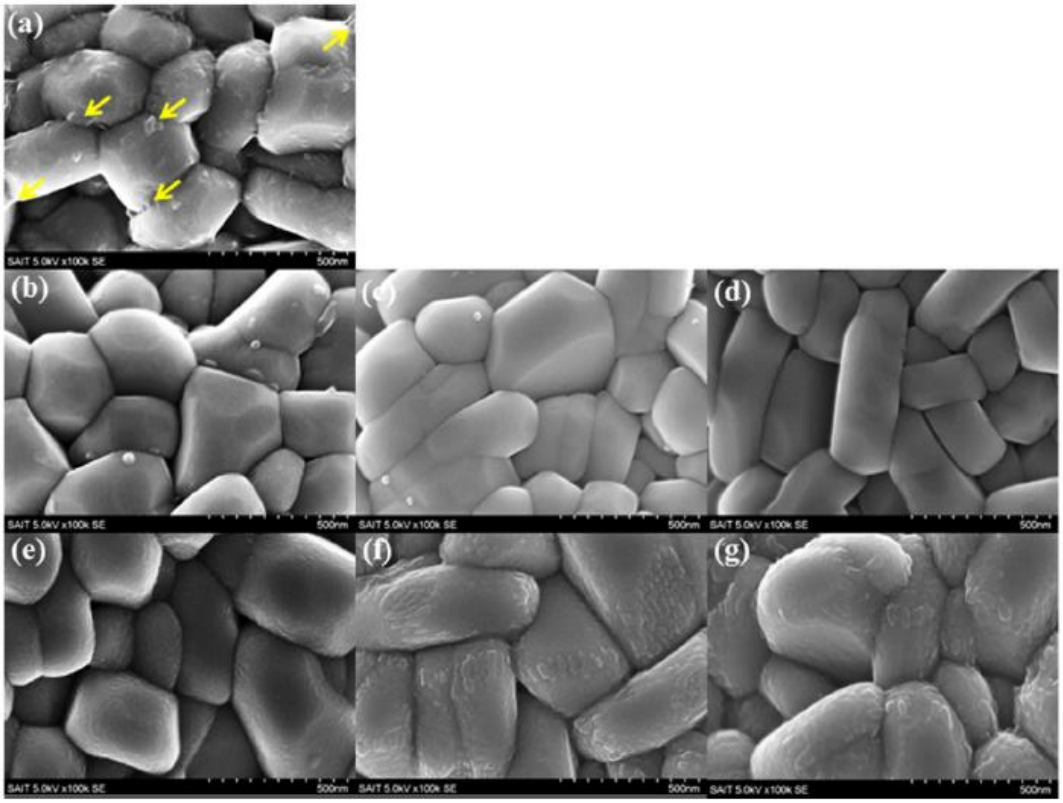

Figure 2.2.2 SEM images of (a) bare, and washing and drying at (b) 80 ℃, (c) 120 ℃, and (d) 190 ℃ without post heat treatment and post heat treated powder after drying at (e) 80 ℃, (f) 120 ℃, and (g) 190 ℃. The ratio of water to NCM is 1:1.

Drying temperature (℃)	Residual lithium (ppm)	
	Before HT	**After HT**
bare	2319	2215
80 ℃	1203	512
120 ℃	1130	799
190 ℃	916	825

$*$ Total Li $(ppm) = \frac{Atomic\ weight\ of\ Li}{\boldsymbol{molecular\ weight\ of}\ Li_2CO_3} \times Li_2CO_3(ppm) + \frac{Atomic\ weight\ of\ Li}{\boldsymbol{molecular\ weight\ of}\ LiOH} \times LiOH(ppm)$

Table 2.2.1 Total amount of residual lithium by titration of bare NCM, and NCM that was washed and dried at 80 ℃, 120 ℃, and 190 ℃ according to the before/after post heat treatment(HT). The ratio of water to NCM is 1:1.

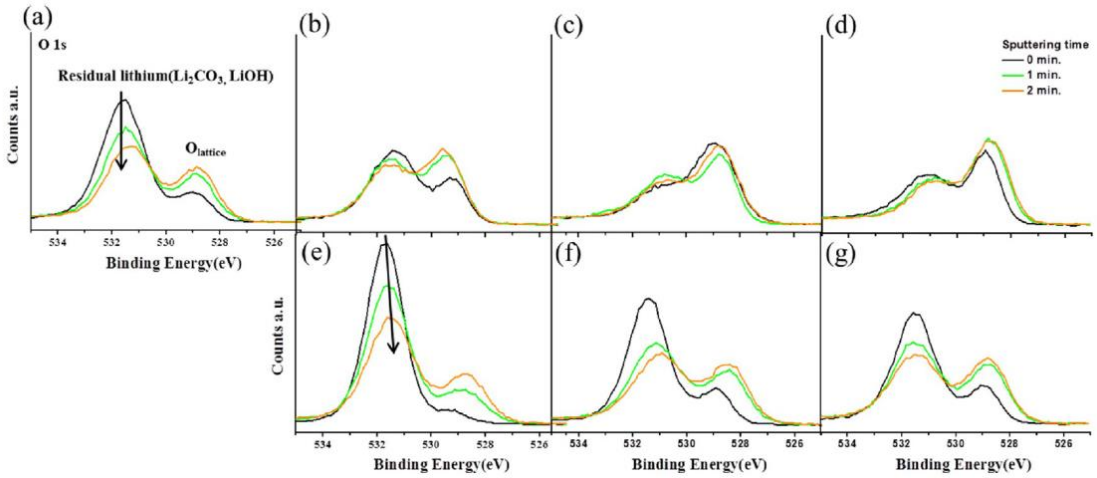

Figure 2.2.3 XPS results for the O1s peak of NCM samples with increasing sputtering time: (a) bare (b) dried at 80 ℃ (c) 120 ℃ (d) 190 ℃ without post heat treatment and post heat treated powder after drying at (e) 80 ℃ (f) 120 ℃ (g) 190 ℃. The ratio of water to NCM is 1:1.

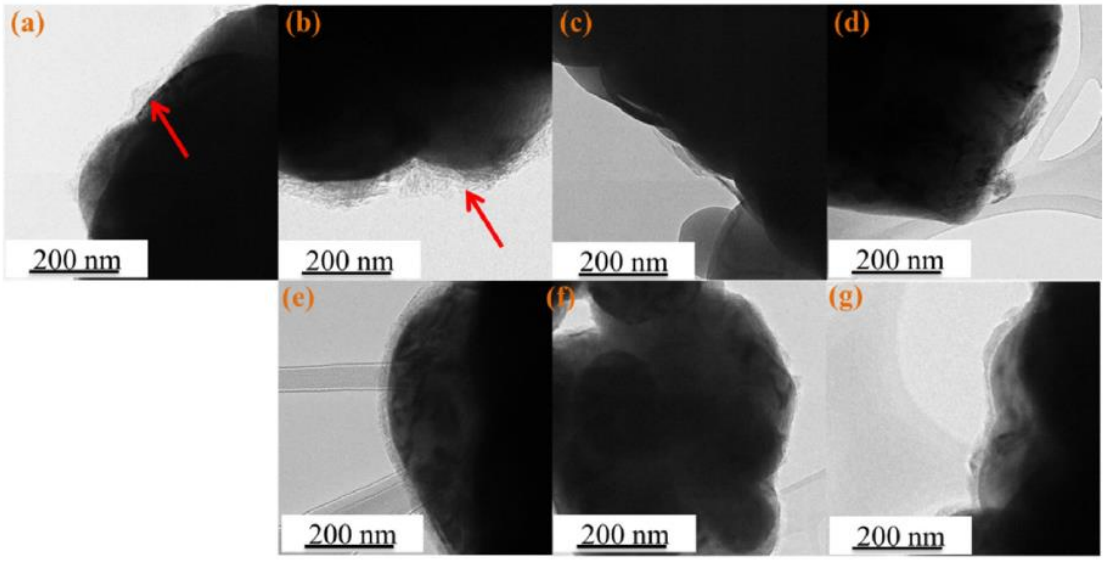

Figure 2.2.4 TEM images of (a) bare, and after washing and drying at (b) 80 ℃, (c) 120 ℃, (d) 190 ℃ without post heat treatment and post heat treated powder after drying at (e) 80 ℃, (f) 120 ℃, and (g) 190 ℃. The ratio of water to NCM is 1:1.

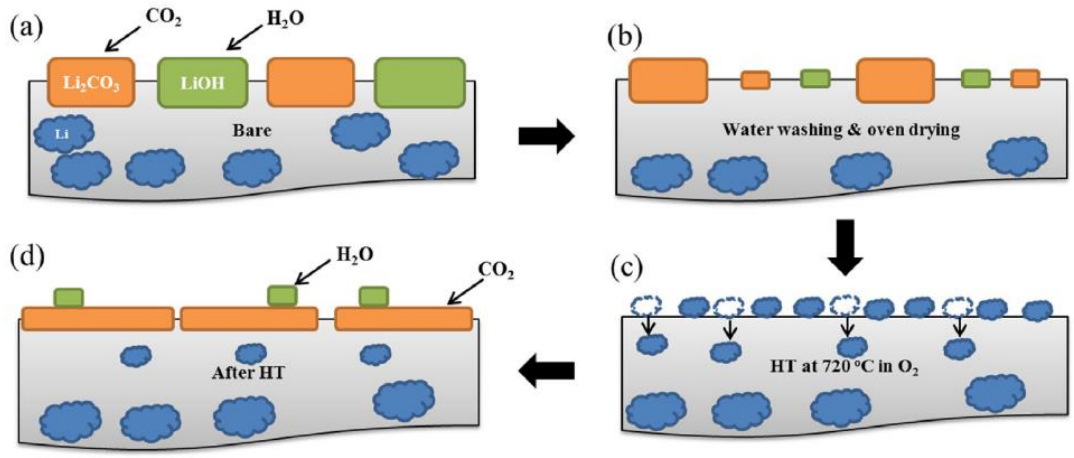

Figure 2.2.5 Schematic illustration of the observed surface changes for NCM during the washing, drying, and post heat treatment (HT) processes.

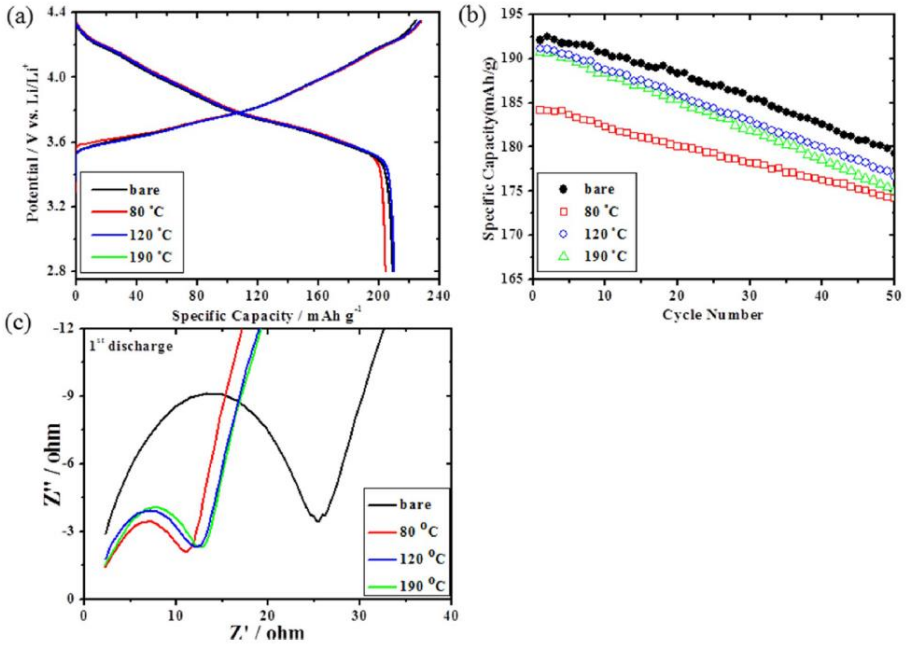

Figure 2.2.6 (a) Voltage profiles vs. capacity for coin-type cells at a rate of 0.1 C between 2.8–4.35 V for the bare and HT after drying at 80 ℃, 120 ℃, and 190 ℃. (b) Cycleability tests at a rate of 1 C in the coin-type half cells. (c) Electrochemical impedance spectroscopy (EIS) comparison of the first discharge state of bare, and after HT after drying at 80 ℃, 120 ℃, and 190 ℃.

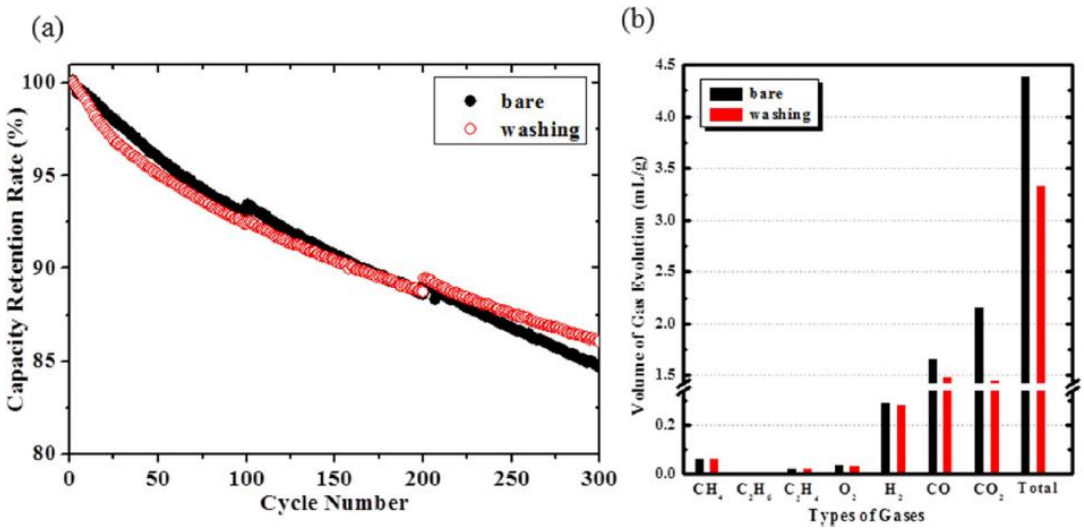

Figure 2.2.7 (a) Plot of the cyclability of 18650 type cell at a rate of 1 C. The ratio of water to NCM is 1:1 and HT after 120 ℃ drying sample is used as a cathode. (b) Comparison of the gas evolution after cycling an 18650 cell 300 times for a bare NCM cathode and a washed cathode (using a water amount of 1:1 water to NCM and HT after drying at 120 ℃).

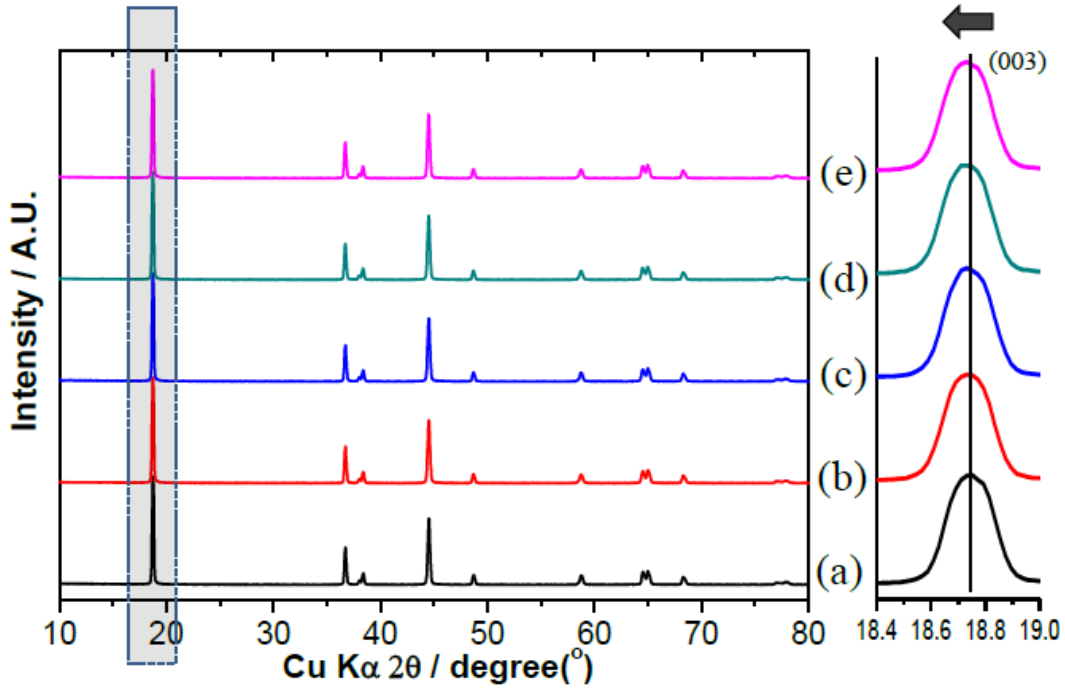

(f)

Sample conditions	Lattice parameter, Å		
	a-axis	c-axis	c/a
bare	2.8682	14.1888	4.9469
0.7:1 (powder : water)	2.8678	14.1917	4.9486
1:1	2.8679	14.193	4.9489
1:2	2.8677	14.1936	4.9495
1:5	2.8679	14.1952	4.9497

Figure 2.2.8 Powder XRD patterns for (a) bare and washing water amount of (b) 0.7:1 (powder : water), (c) 1:1, (d) 1:2, (e) 1:5 and magnified image for the dashed line rectangle at the right side, and (f) corresponding lattice parameters.

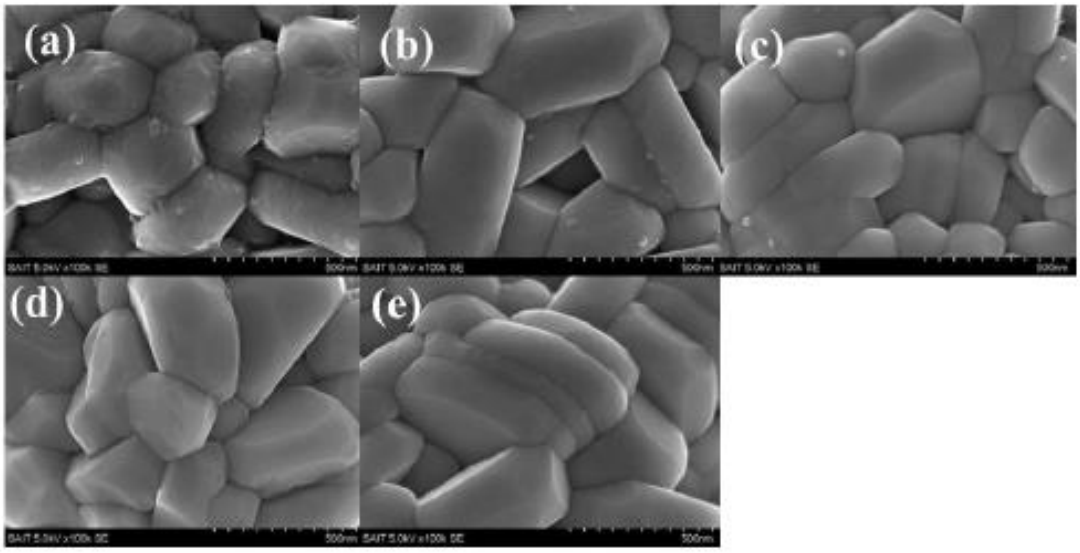

Figure 2.2.9 SEM images of (a) bare and washing water amount ratio of (b) 1:0.7 (powder : water) (c) 1:1 (d) 1:2 and (e) 1:5

Sample conditions	Mole ratio, %			
	Li	Mn	Co	Ni
Bare	1.03	0.050	0.149	0.802
0.7:1 (powder : water)	1.02	0.049	0.149	0.802
1:1	1.00	0.049	0.148	0.803
1:2	1.01	0.049	0.148	0.804
1:5	1.00	0.049	0.148	0.804

Table 2.2.2 ICP-MS data to confirm the chemical compositions of the bare and washed powders

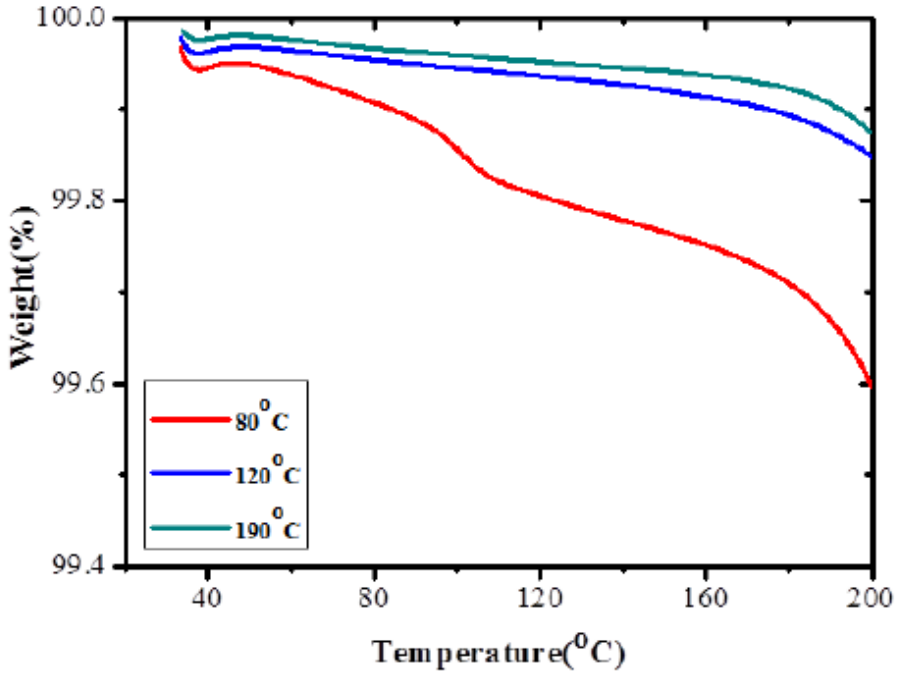

Figure 2.2.10 TGA profiles of the washed powders dried at 80 ℃, 120 ℃ and 190 ℃ without post heat treatment. The ratio of water to NCM is 1:1.

Drying temperature (℃)	Before HT		After HT	
	Li_2CO_3 (wt%)	LiOH (wt%)	Li_2CO_3 (wt%)	LiOH (wt%)
bare	0.73	0.56	0.46	0.62
80	0.73	0.18	0.23	0.10
120	0.43	0.25	0.30	0.18
190	0.71	0.09	0.32	0.18

Table 2.2.3 Li_2CO_3, LiOH amount by titration; total amount of residual lithium by titration with no washing/heat treatment (bare), and drying at 80 ℃, 120 ℃ and 190 ℃ according to the before/after post heat treatment (HT). The ratio of water to NCM is 1:1.

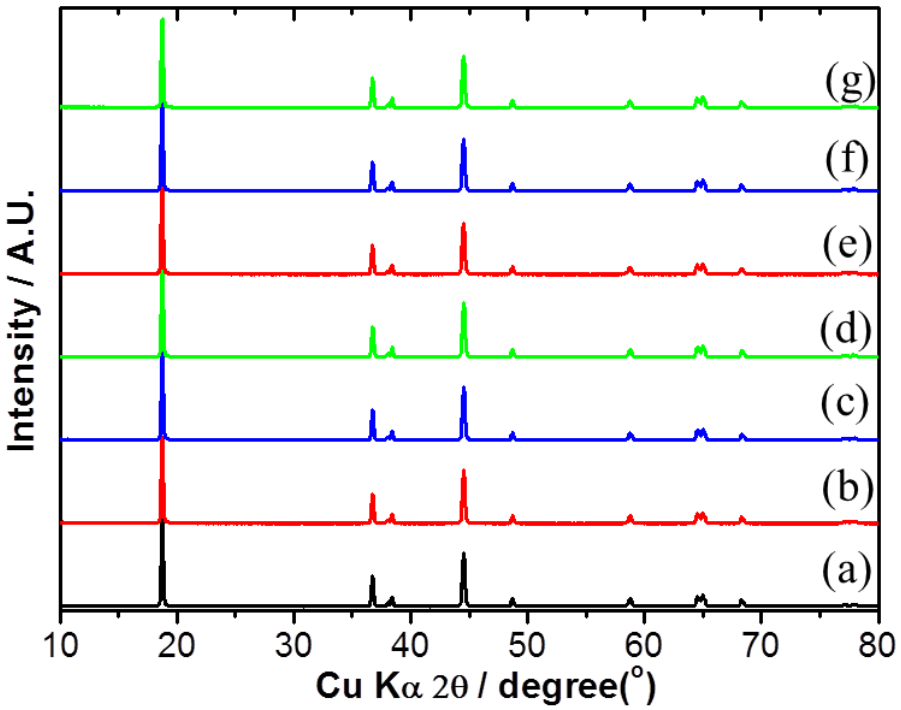

Figure 2.2.11 Powder XRD patterns for (a) no washing/drying (b) drying temperature of 80 ℃ (c) 120 ℃ (d) 190 ℃ (e) post-heat-treatment(HT) after 80 ℃ (f) 120 ℃ (g) 190 ℃ drying

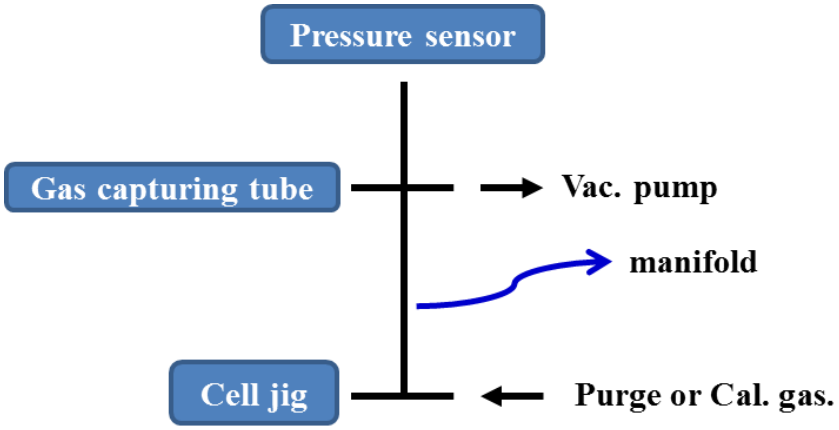

Figure 2.2.12 Schematic diagram of gas sampling system (valves at each end of manifold are omitted for simplicity)

2.3.2 Dry process (blending & mechano-fusion)

To check the synthesized materials, XRD analyses were performed with synthesized $VOPO_4$ and OLO powder. Figure 2.3.2(a) shows that the XRD pattern of as-synthesized $VOPO_4$ powder was in good agreement with that of δ-vopo4 (JCPDS card # 47-0951) and that of δ-$VOPO_4$ previously synthesized using the same method [60]. Among the several polymorphs of $VOPO_4$, δ-$VOPO_4$ is reported as the one most suited for the positive electrode material application in terms of energy density, showing high capacity and initial coulombic efficiency exceeding those of other polymorphs [60]. $VOPO_4$ has various phases such as α_I, α_{II}, β, γ and δ. Despite the all crystalline initially has the same oxidation number of V^{4+}, the electrochemical behaviors are different to each other. As shown in Figure 2.3.2(b), the $VOPO_4$ used in the manuscript has d phase, which has the best performance among the $VOPO_4$ [79].

On the other hand, Figure 2.3.2(b) shows that the prepared OLO also exhibit a pattern highly corresponding to that of hexagonal structure, and it also describes Li_2MnO_3 (JCPDS card # 01-084-1634) exists as a nanocomposite or solid solution within $LiMO_2$ (JCPDS card # 01-070-4314). As shown in Figure 2.3.2(c) and (d), as-synthesized $VOPO_4$ and OLO powder contained thin flake-like particles and round aggregated particle with ~5 μm diameter. Figure 2.3.3(a) shows the first and second charge/discharge curves of a $VOPO_4$-only positive electrode, revealing that the electrochemical oxidation capacity during initial charging was negligible (<3

$mAh \cdot g^{-1}$). Even at a high potential of 4.4 V vs. Li/Li^+, $VOPO_4$ could not be electrochemically oxidized (due to V being already present in the pentavalent state of V^{5+}), maintaining its structure upon charging and thus acting as a good passivation material. During the subsequent first discharge step, a long plateau was observed, corresponding to the lithiation of $VOPO_4$ (specific capacity = 86.1 $mAhg^{-1}$). As reported previously, $VOPO_4$ can accommodate lithium ions at a voltage of ~3.8 V (vs. Li/Li^+), as illustrated in Figure 2.3.3(a), with this intercalation resulting in an oxidation state change from V^{5+} to V^{4+} to form $LiVOPO_4$ [58]. Considering that other vanadium oxides such as VO_2 and V_2O_5 series materials operate at less than 3 V of lithiation behavior, the high operating voltage of $VOPO_4$ is beneficial, which can effectively increase energy density when used for the supporting material of high energy density positive electrode materials. Furthermore, $VOPO_4$ only participated in the first discharge step due to not initially containing any Li. $VOPO_4$ was reversibly delithiated in subsequent cycles. To demonstrate the effect of $VOPO_4$ in the positive electrode, the OLO simply mixed, not coated, with $VOPO_4$ powder was evaluated. Figure 2.3.3(b) shows the first charge and discharge curves of bare OLO and OLO mixed with various amounts of $VOPO_4$, revealing that all initial charging capacities normalized with respect to pure OLO mass were similar to each other. As the content of mixed $VOPO_4$ increased from 0 to 20 wt%, the discharge capacities increased owing to the increasing number of additional lithium intercalation sites provided by $VOPO_4$.

The first delithiation curve featured two regions with different slopes, which was explained by the participation of the conventional layered structure at voltages below 4.4 V, with the region above 4.4 V reflecting the activation of Li_2MnO_3 in the OLO structure. After full charging to 4.5 V, the above two plateaus were not observed due to the changed structure of Li_2MnO_3. Since the charge and discharge capacities were normalized to pure OLO mass, the increased discharge capacity was ascribed to the effect of blended $VOPO_4$. Furthermore, the initial charge-discharge coulombic efficiency gradually increased with increasing $VOPO_4$ content, equaling 86.8, 90.2, and 93.1 % for 0, 10 and 20 wt.% $VOPO_4$ loadings, respectively. Considering the electrochemical behavior of $VOPO_4$ in the first cycle, it was concluded to contribute to the specific capacity only during discharge. The dQ/dV graph, shown in Figure 2.3.7, reveals that increased $VOPO_4$ loadings enhanced the peak from 3.7 to 3.2 V owing to the presence of $VOPO_4$ in the mixed samples. Although no distinct peak was observed at 3.6-3.9 V (vs. Li/Li^+), which is regarded as the voltage range of $VOPO_4$ activation (based on the plots of initial differential charge-discharge capacity vs. voltage), the deviation of the discharge curve in the above range (Figure 2.3.3(b)) was attributed to blended $VOPO_4$. This mixed voltage behavior inhibited the probable loss of energy density due to potential lowering. To apply $VOPO_4$ as a surface stabilizer, the mechanochemical coating method was introduced onto OLO material. So far, the annealing-based coating has been commonly used to surface modify the

electrode powder after the co-precipitation of the coating material precursor. However, this method exhibits the drawback of pristine and coating material deterioration by possible thermal side reactions. Furthermore, $VOPO_4$ should be synthesized in an Ar atmosphere to inhibit oxide impurity formation, and heat treatment in an Ar atmosphere will form the oxygen defects in OLO material, accelerating degradation of performance of OLO. Therefore, it is difficult to coat $VOPO_4$ on OLO by the conventional heat treatment coating method. Herein, the coating of $VOPO_4$ to OLO was performed using a mechanochemical instrument (Figure 2.3.9(a)), which allowed one to control the applied shear stress as shown in Figure 2.3.9(b) [55]. In the prepared $VOPO_4$-coated OLO composite, the structure of $VOPO_4$ was largely preserved, since mechanochemical coating does not require costly heat treatment. The nano-sized $VOPO_4$ powder was prepared by ball milling for the coating material of mechenochemical coating (Figure 2.3.4(a)), since the particles of the coating should have a smaller diameter than the core material of the OLO powder (of the order of microns). The surface analyses comprising SEM (Figure 2.3.4(b)), EDS (Figure 2.3.4(c)), and XPS (Table 2.3.1) revealed that the OLO surface was successfully covered with $VOPO_4$. At the first glance, the SEM image in Figure 2.3.4(b), showing the surface morphology of nano-sized $VOPO_4$ particles coated OLO has similar surface morphology to that of the pristine OLO. However, the coated $VOPO_4$ particles are well visualized by the vanadium and phosphate EDS map in Figure

2.3.4(c and d) as dots well distributed all over the OLO surface. Furthermore, Table 2.3.1 presents the XPS-determined atomic concentrations of C, O, P, V, and Mn in the surface of the prepared samples, revealing that the atomic concentrations of V and P, which come from the surface coated $VOPO_4$, increased, and that of Mn decreased with increasing $VOPO_4$ coating. Considering that XPS is a surface analyses method, it reflects that $VOPO_4$ greatly covers the surface of OLO and hinders photoelectrons generated from the core material of OLO. Thus, it was concluded that the proposed method was well suited for the preparation of $VOPO_4$-coated OLO.

Figure 2.3.5 shows the initial voltage curves of $VOPO_4$-coated OLO, with those in Figure 2.3.5(a) showing the first-charge/discharge profiles normalized with respect to OLO mass. Notably, the 0.5 wt%-coated OLO exhibited an initial Coulombic efficiency of 87.6%, which was higher than those of other samples, including 86.7% of the bare OLO. Although the large coatings of 1 and 2 wt.% of $VOPO_4$ were also applied, but the initial coulobmic efficiencies of the coated samples were less than the pristine OLO. Their initial charge specific capacities as well as subsequent discharge specific capacities decrease as the coating amount increases. It was thought that the thick coating of $VOPO_4$ on OLO surface caused polarizations by hindering lithium ion (de)intercalation. Figure 2.3.5(b) shows the cycling performances of bare and $VOPO_4$-coated OLO. Despite being small, the capacities of 0.5, 1, and 2 wt.% $VOPO_4$-

coated OLO were relatively highly preserved, whereas that of bare OLO sharply decreased with increasing cycle number. As shown Figure 2.3.5(a), high $VOPO_4$ loadings resulted in decreased capacity due to promoting polarization [80,81]. Notably, 0.5 wt% $VOPO_4$-coated OLO, which showed the highest initial charge-discharge capacity, still showed a larger capacity than bare OLO even after 170 cycles. On the other hand, the capacity and coulombic efficiency of the blended OLO with the same amount of $VOPO_4$ sharply decreased with cycling, which was ascribed to the aggregated $VOPO_4$ powder in the electrode not having the beneficial effect of coating. The coating also improved cycling performance, as confirmed by comparison of coulombic efficiencies of coating- and blending-produced electrodes. Despite containing identical amounts of $VOPO_4$, the above electrodes showed different characteristics, e.g., after 100 cycles, the average efficiencies of bare OLO, 0.5 wt.% $VOPO_4$-blended, and 0.5 wt.% $VOPO_4$-coated electrodes equaled 98.8, 96.0, and 98.9%, respectively. Similarly, 1 and 2 wt. % $VOPO_4$-coated electrodes exhibited high coulombic efficiencies of 98.9 and 99.0 %, respectively. Thus, all $VOPO_4$-coated samples showed a better efficiency than the pristine and the simple blended one, probably due to the coated $VOPO_4$ acting as a barrier between the electrolyte and OLO and thus inhibiting undesirable side reactions between them. On the other hand, the low efficiency observed for 0.5 wt.% $VOPO_4$-blended OLO was explained by $VOPO_4$ agglomeration leading to large resistance upon charge-discharge. To trace the

polarization behavior of the prepared electrode, I performed the high current density discharge. And the result voltage curves are shown in Figure 2.3.5(c). It is found that the bare OLO exhibited a less polarization at the beginning of discharge than the coated sample. With the voltage curve of 0.5 wt.% coated sample, the discharge capacity was almost same with that of the pristine material even though it has higher polarization at the beginning of the discharge. The coating of 0.5 wt.% brought a small polarization however, the $VOPO_4$ coating participated the discharge capacity, and therefore the discharge capacity was almost same at the end of discharge. As the coating amount increased, the polarization behavior also accelerated. Considering this unfavorable polarization behavior of $VOPO_4$ coating, the optimized coating amount should be found for high performance of the LIBs. Another concern is the thermal stability enhancement of $VOPO_4$-coated OLOs. Figure 2.3.6 shows the DSC curves of bare and 0.5 wt % OLOs, allowing the thermal stabilities of these charged positive electrode materials in electrolytes to be assessed based on the decomposition onset temperature, peak temperature, and amount of released heat. The obtained results reveal that surface modification with 0.5 wt% $VOPO_4$ results in thermal stability improvement, with the $VOPO_4$ coating suppressing the exothermic reaction of OLO with the electrolyte. Furthermore, coating shifts the peak temperature from 240.1 to 244.6 ^{o}C and reduces the amount of released heat from 1894 to 1441 J g^{-1}.

2.4 Conclusions

Transition metal (TM = Al, Co, and Fe) phosphate coatings prepared by wet chemical deposition were used to enhance the electrochemical performance of $Li_{1.0}Ni_{0.8}Co_{0.15}Mn_{0.05}O_2$ (NCM) positive electrode materials, with the observed effects depending on the used metal and the TM/P ratio. In all cases, coating decreased the content of Li residuals, implying that these species were converted into other compounds during the coating process. Al/P was the most effective coating material, whereas Fe/P-coated NCM samples showed performances similar to that of pristine NCM. Considering the removal of Li residuals in addition to capacity and capacity retention, a 1:1 Co/P coating proved to be most effective for surface modification, achieving initial capacity and capacity retention increases of 10 mAh g^{-1} and 3%, respectively, as compared to the pristine material. Moreover, the beneficial effect of this coating was also confirmed for the more Ni-rich $Li_{1.0}Ni_{0.91}Co_{0.06}Mn_{0.03}O_2$.

Reducing the amount of residual lithium by washing the Ni-rich NCM is an important process to facilitate the commercialization of this promising cathode material. A fundamental understanding of the reactions associated with washing is required to optimize the washing process, which was the focus of this investigation. The surface composition of the Ni-rich NCM, which includes a residual lithium layer, was dramatically altered by the parameters used

in the washing process, and these effects were examined by TEM, SEM, XRD, XPS, electrochemical tests, and EIS. Although the residual lithium is most effectively removed by increasing the amount of water used for washing, the cycling performance decreases with increasing water use. The optimal water/NCM ratio for washing was determined to be 1:1.

Drying temperatures of 80, 120, and 190 ^{o}C were investigated and observed to induce the reformation of a residual lithium layer on the surface of NCM. The residual lithium layer that was removed by washing with water was reformed by the HT and drying processes. The use of different drying temperatures caused differences in the thickness and morphology of this reformed residual lithium layer. Li_2CO_3, especially, can be turned into porous LiF which can be a resistive or protective layer, upon Li_2CO_3 reaction with lithium salt in the electrolyte. The decrease of the coulombic efficiency following the first cycle is regarded as this reaction due to the reformed residual lithium layer. The optimal drying temperature was determined to be 120 ^{o}C by investigating the electrochemical performance and the amount of remaining residual lithium from titration data. The full cell electrochemical performance and gas evolution of cylindrical-type 18650 cells were evaluated using the optimized conditions. The resulting CRR was improved from 84.6% to 86.1%, and the gas evolution was reduced by ~25% compared with the unwashed sample. Future work will focus on finding surface treatments to control the presence of residual lithium, with the aim of enhancing the electrochemical performance by

understanding the characteristics of residual lithium on Ni-rich layered oxides.

Nanosized δ-$VOPO_4$ synthesized using a reflux method and a ball milling was coated onto OLO to produce LIB positive electrode materials using a mechanofusion technique. As a result, the irreversibility of the first charge-discharge cycle, which is an intrinsic problem of OLO positive electrodes, was considerably reduced by the application of $VOPO_4$, which provided additional lithium intercalation sites for discharge. Importantly, surface-coated $VOPO_4$ positively affected cycling lifetime and thermal stability, which suggests that this phosphate can be used as a bi-functional coating for positive electrodes employed in electric transportation vehicles.

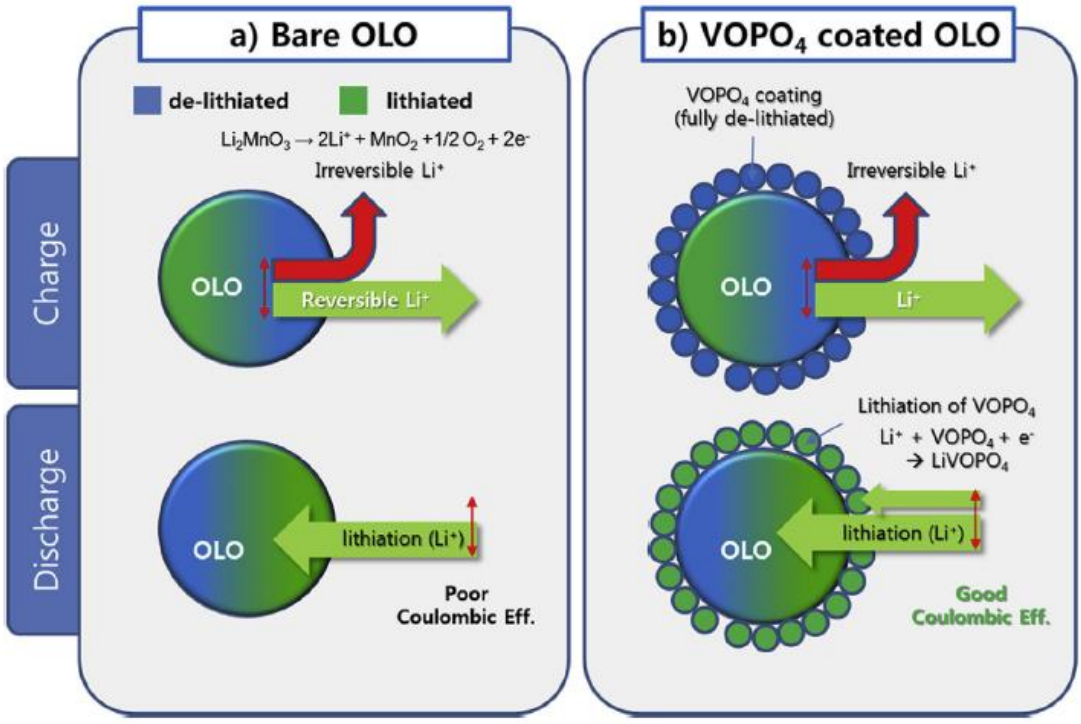

Figure 2.3.1 Schematic figures showing the process for initial lithation and de-lithiation of (a) OLO and (b) $VOPO_4$ coated OLO.

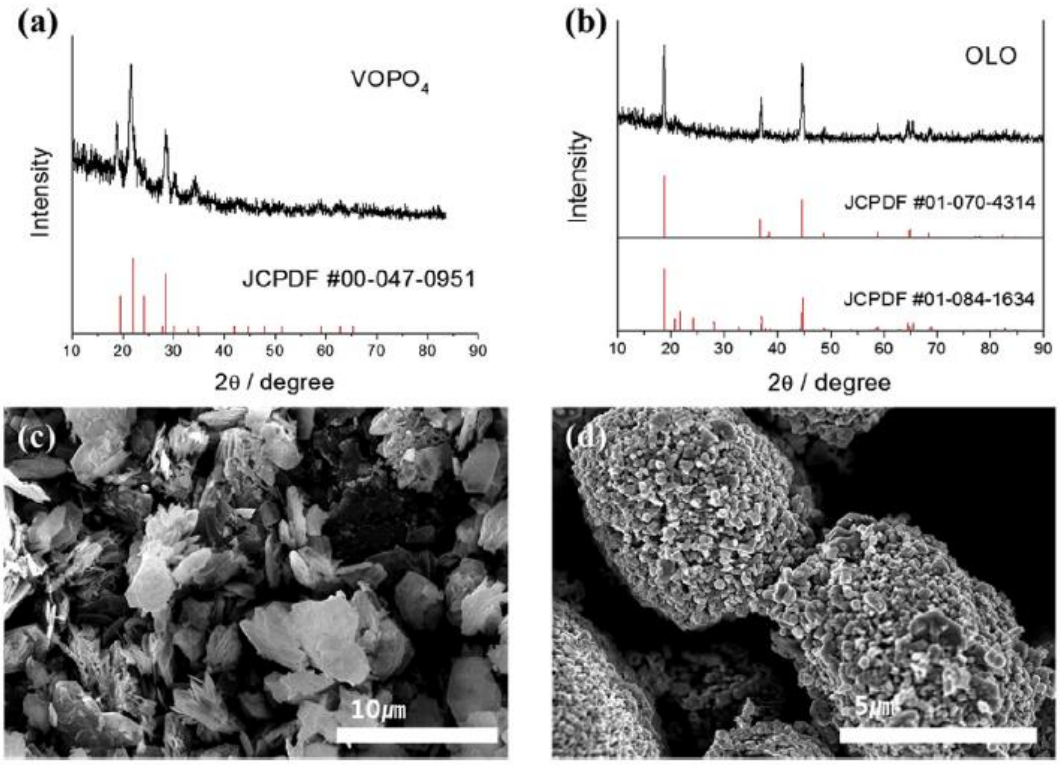

Figure 2.3.2 XRD diffraction patterns of (a) as-synthesized $VOPO_4$ and (b) OLO. SEM micrographs of (c) as-synthesized $VOPO_4$ and (d) OLO.

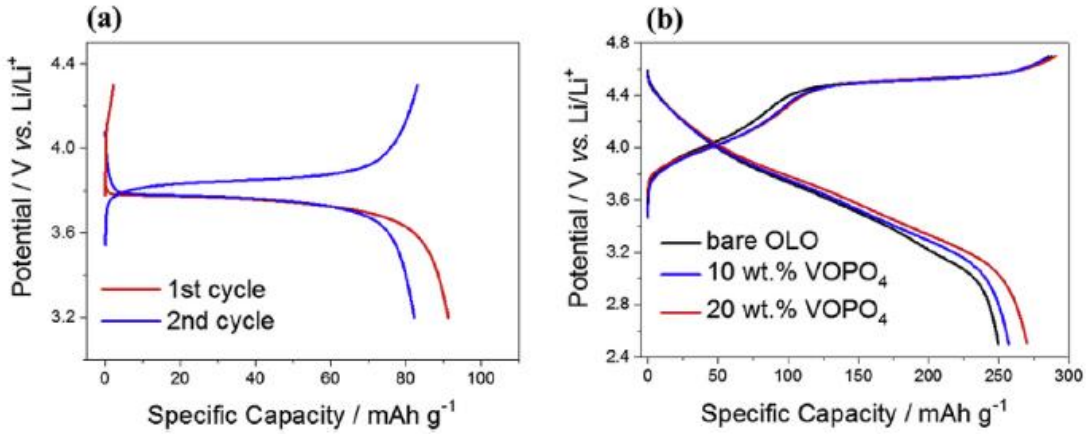

Figure 2.3.3 First- and second-cycle voltage profiles at 0.1C of 2032 coin type half-cells with (a) $VOPO_4$ and (b) OLO positive electrodes having 0, 10 and 20 wt.% of VOPO4 in the blended state. (Temperature; 25 ^{o}C, electrolyte; 1.3M $LiPF_6$/EC:DEC and the electrode capacity areal density; 1 mAh cm^{-2}.)

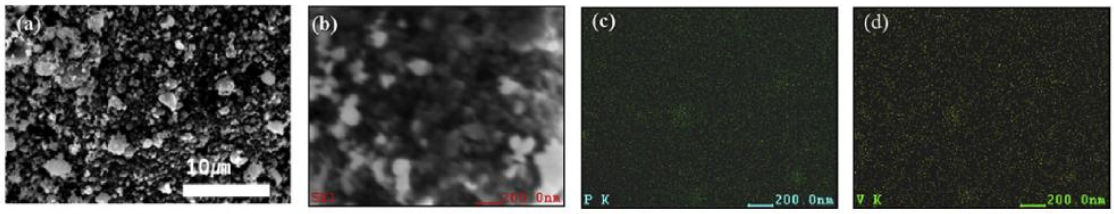

Figure 2.3.4 SEM images of (a) ball-milled $VOPO_4$ and (b) 1 wt.% $VOPO_4$-coated OLO. (c) Phosphate and (d) Vanadium EDX mapping image of Figure 2.3.4(b).

	C1s	O1s	P2p	V2p	Mn2p
Bare OLO	17.84	62.44	0.00	0.00	19.72
0.5 wt% $VOPO_4$	16.90	63.96	1.00	0.87	17.27
1 wt% $VOPO_4$	17.39	62.71	3.11	2.13	14.66
2 wt% $VOPO_4$	19.79	60.88	5.50	4.12	9.72

Table 2.3.1 XPS-determined elemental compositions of bare and δ-$VOPO_4$-coated OLO.

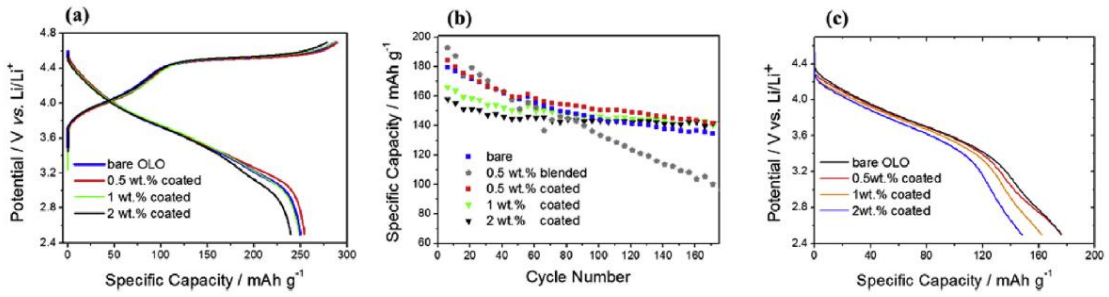

Figure 2.3.5 (a) Initial voltage curves of the bare OLO and the 0.5, 1 and 2 wt.% $VOPO_4$ coated OLO at a current density of 25 $mA \cdot g^{-1}$ and (b) discharge voltage curves of 2032 coin type half-cells with bare and $VOPO_4$-coated OLO recorded at a current density of 450 $mA \cdot g^{-1}$ after the controlled charge sequence (current density: 125 $mAh \cdot g^{-1}$; constant voltage mode was inserted to the end of charge until 12.5 $mA \cdot g^{-1}$) (c) the discharge voltage curves under 2C current density of the 2032 coin type half cells

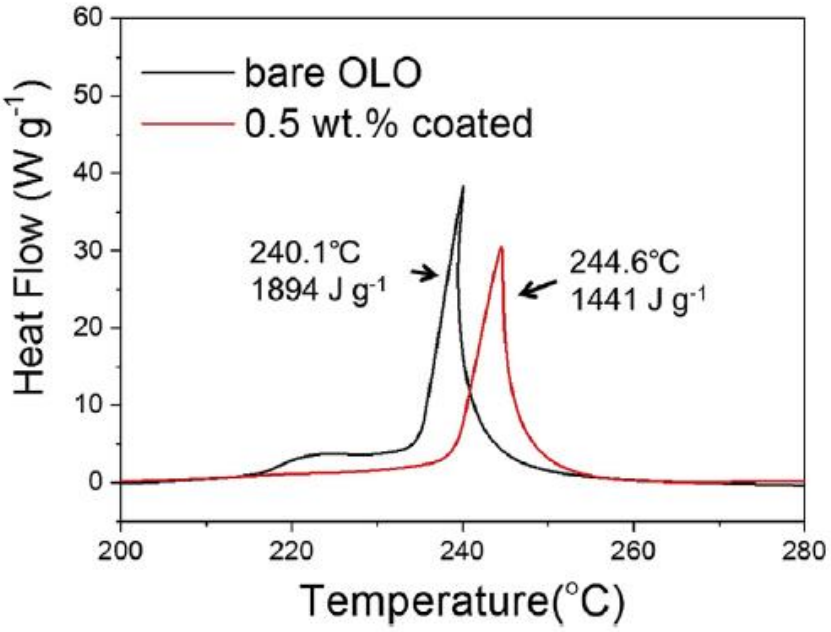

Figure 2.3.6 Differential scanning calorimetry (DSC) graphs of the fully charged bare and 0.5 wt.% $VOPO_4$-coated OLO.

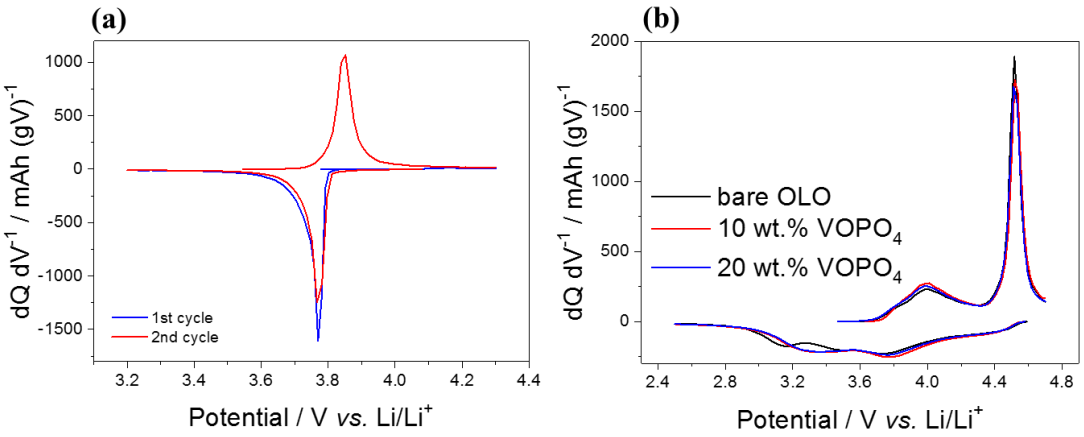

Figure 2.3.7 Differential capacity versus voltage curves of (a) 1st and 2nd cycle for $VOPO_4$ and (b) 1st cycle for $VOPO_4$ blended OLO

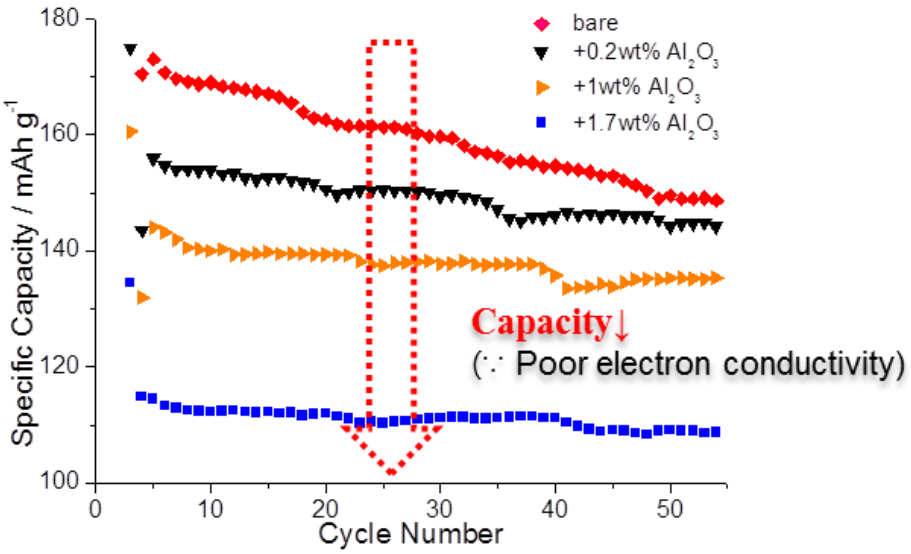

Figure 2.3.8 Capacity loss(2032 coin type half-cell cycling at 1C rate) by conventional surface coating materials (Al_2O_3)

(a)

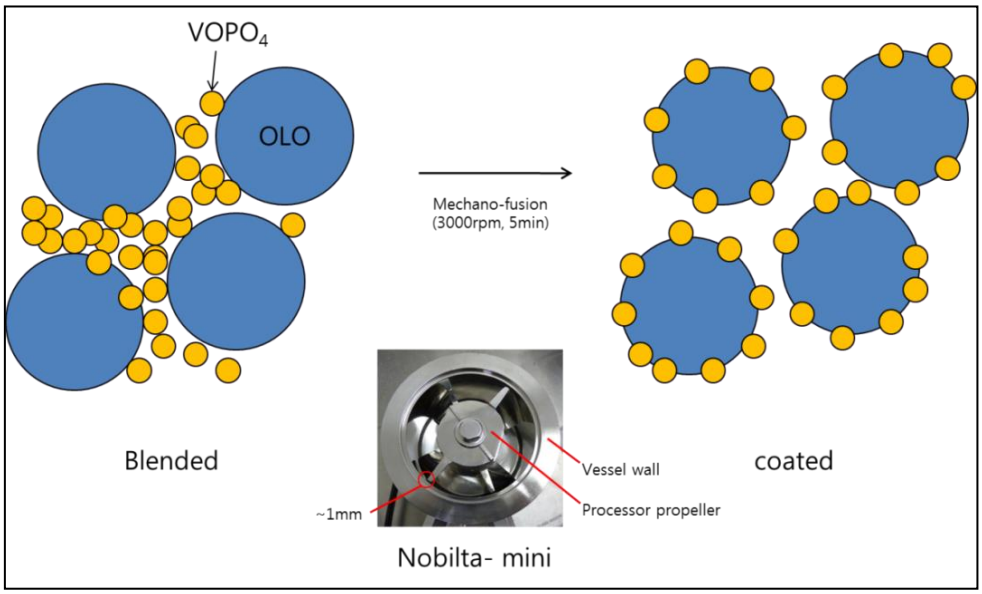

(b)

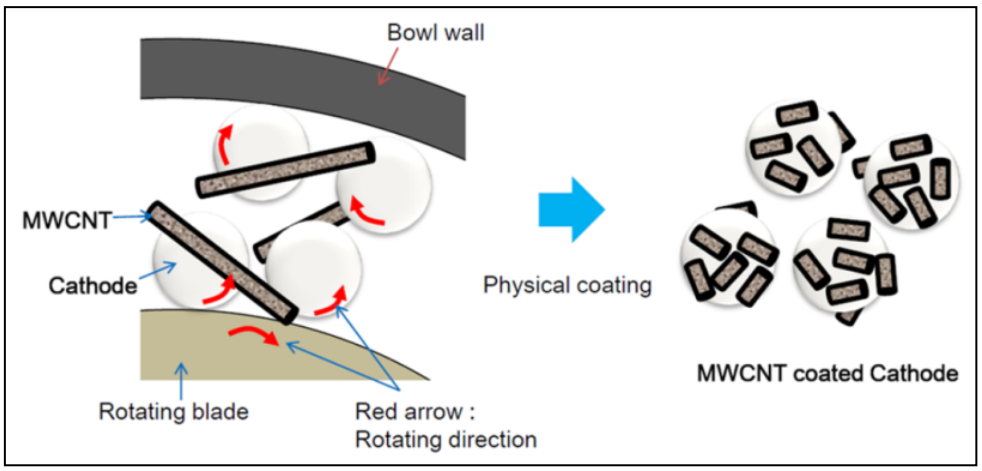

Figure 2.3.9 Schematic flow of (a) mechano-fusion process [55] and (b) dry coating method.

Chapter 3.
Molecular-level Surface Rearrangements for High-stability Ni-rich Layered Oxide Cathode Materials using Metal-organic Frameworks

3.1 Introduction

Among layered ternary cathode materials, Ni-rich layered oxides, such as $LiNi_{0.80}Co_{0.15}Mn_{0.05}O_2$ (Ni-rich NCM with ≥70 mol.% of Ni and the remainder Co and Mn) are good candidates as cathode materials of the lithium-ion batteries (LIBs) for use in electric vehicles [8,14,46]. The requirements of the cathode materials are high specific capacity, good cyclability, high chemical stability, material that can be mass-produced and cost effective. Because of its higher Ni content, full oxidation of Ni^{2+} to Ni^{4+} can deliver higher specific capacity (~200 mAh/g) than other cathode materials, such as $LiCoO_2$ and $LiNi_{1/3}Co_{1/3}Mn_{1/3}O_2$. However, challenges such as poor cyclability and gas evolution from the Ni-rich NCM during charge–discharge cycles limit commercialization of this material [82]. In particular, irreversible changes in crystal structure occur at the surfaces of the active particles during cycling: the original layered phase (R-3m) transforms into a NiO-type rocksalt secondary phase (Fm-3m) via the migration of transition metal ions [20,78] In addition, facile Li^+/Ni^{2+} intermixing owing to the similar atomic size of Ni^{2+} (0.69 Å) and Li^+ (0.76 Å) and the presence of unreacted residual lithium on the surface of the Ni-rich NCM deteriorates the electrochemical performance [44,83].

Surface protection and modification of the surface chemistry have been used to enhance the cycle performance and thermal stability of cathode materials, including oxides,

fluorides, and phosphates[84–86]. These typical surface modification methods have also been considered for improving the surface stability of Ni-rich NCM. Compositionally graded Ni-rich NCM (with a continuous compositional change from the core of the active particles to the surface) form a Co- and/or Mn-rich layered surface differing from that of the pristine Ni-rich layered material[82]. These previous studies demonstrated improved cycling with an increase in the surface content of Co and/or Mn, which resulted in high structural and thermal stability of the Ni-rich NCM. However, in the case of cathode materials with compositional heterogeneity, it is very difficult to precisely control the composition gradient in Ni, Co, and Mn ions throughout the active particles due to the different inter diffusion coefficients between the transition metal ions as a function of their oxidation states[87].

Physical surface protection by coating the surface with oxides, phosphates, fluorides, carbons, and conducting polymers[28,34,49,51,81,88], is another useful strategy for stabilizing the surface structure of the Ni-rich NCM by mitigating direct contact and unwanted side reactions between the active material (including residual lithium on the particle surface) and the organic electrolyte during battery operation. In addition, the coating layers possibly suppress the irreversible structural transition from the layered to NiO-type rocksalt phase on the surface of the layered materials that leads to large lattice strain followed by the breakdown of the original layered lattice. However, the mechanism by which the surface coating protects

the active particles is complex and still not fully understood as most electrochemically inactive and thick coating layers impede Li ion transfer at the interfaces between the particles and electrolyte[89]. Hence, none of these coating methods have provided an efficient solution for improving the electrochemical performance of the Ni-rich NCM cathode materials.

In this study, I introduced a Co-containing MOF, zeolitic imidazolate framework-67 (ZIF-67), into Ni-rich NCM ($LiNi_{0.80}Co_{0.15}Mn_{0.05}O_2$) as a novel surface-modifying agent for the first time. It is possible to mass produce ZIF-67 as it can be easily synthesized in water at room temperature and under atmospheric pressure at a low cost[90]. Siwu et al. previously reported superior cell cycling performance of a $LiNi_{0.6}Co_{0.2}Mn_{0.2}O_2$ cathode material by introducing an Al-based metal organic framework (MOF), thereby deriving a well-dispersed coating layer (5–7 nm thick) of amorphous alumina with no surface structural rearrangements[91]. Unlike the previous study, using ZIF-67 as a coating agent, Co ions are introduced onto the surface of the Ni-rich NCM during a post-heat treatment, leading to extensive molecular-level surface rearrangements by galvanic replacement reactions[92]. Such reactions between the Co and Ni ions on the surface of Ni-rich NCM result in a transformation from the layered (R-3m) to spinel-like phase (Fd-3m) as some Ni ions migrate to the neighboring vacant Li sites due to the incorporation of Co ions onto Ni sites. Here, surface Li sites are present due to the Li-deficient Ni-rich NCM ($Li_{1-x}Ni_{0.80}Co_{0.15}Mn_{0.05}O_2$) stoichiometry

and the melted residual lithium on the surface provides a pathway for exchanging Ni and Co ions at high temperatures. Moreover, the substitution of Ni by Co ions can stabilize the structure of the layered oxides by reducing the cation disorder and mitigating multi-phase transitions during cycling[84–86]. Differing from the layered-to-spinel transformation in the middle of charge–discharge cycling, the introduction of an optimum amount of spinel-like phase into the surface lattice structure of Ni-rich NCM before cycling is also beneficial for improving the Li-ion kinetics and stability of the layered active materials.[14,83] Therefore, the resultant Co- and Ni-rich domain with a more stable spinel-like phase formed on the surface improved the cyclability and thermal stability of the MOF-treated Ni-rich NCM.

3.2 Experimental Procedure

3.2.1 Synthesis of MOFs

The zeolitic imidazolate framework-67 (ZIF-67) MOF material was chosen as the reagent for the surface treatment of the $LiNi_{0.80}Co_{0.15}Mn_{0.05}O_2$ (Ni-rich NCM) powder. ZIF-67 was synthesized according to the following procedure: N-methylimidazole (MeIm) was dissolved in methanol and $Co(NO_3)_2{\cdot}6H_2O$ was added under stirring. Excess MeIm was present as I used a stoichiometric ratio of MeIm to $Co(NO_3)_2{\cdot}6H_2O$ of 2:1. The solution turned deep purple and turbid within 10 min. The mixture was stirred overnight, and the synthesized nanocrystals were

then separated from the solution by centrifugation and dried overnight at 100 ℃.

3.2.2 Synthesis and surface treatment of Ni-rich layered oxides

Ni-rich NCM powder was prepared by mixing a co-precipitated $Ni_{0.80}Co_{0.15}Mn_{0.05}(OH)_2$ powder with $LiOH{\cdot}H_2O$ and firing at 750 ℃ for 24 h in O_2 atmosphere. Then, $LiNi_{0.80}Co_{0.15}Mn_{0.05}O_2$ and the prepared ZIF-67 MOF were mixed in a Henschel mixer to achieve homogeneous mixing. The dried powder was heat-treated at 700 ℃ for 5 h under flowing O_2 gas.

3.2.3 Physicochemical Characterization

The phase change in the bulk structure of the active material was analyzed using X-ray diffraction (XRD). The elemental compositions of Li, Mn, Co, and Ni in the Ni-rich NCM powder were determined using inductively coupled plasma-atomic emission spectrometry (ICP-AES; Shimadzu ICPS-8100 sequential spectrometer). All samples were transferred under inert gas from a glove box to the analysis equipment using a specialized transfer vessel to avoid external contamination and oxidation. The Ni-rich NCM and MOF-treated powder were analyzed using thermal gravimetric analysis (TGA; TA Discovery) in the temperature range of 50–800 ℃ under air. The morphological changes due to the MOF treatment were observed by

scanning electron microscopy (SEM; SU-9000). The surface structure and crystal defects of the Ni-rich NCM particles were observed directly by transmission electron microscopy (TEM; FEI Titan Cubed 60-300 equipped with Cs correctors) by loading Ni-rich NCM particles directly onto a TEM grid, without any solvent. For differential scanning calorimetry (DSC; Q2000, TA Instruments) measurements, the 2032 coin-type half cells were fully charged to 4.35 V (vs. Li^+/Li) and opened in a dry room. After washing the positive electrodes with dimethyl carbonate, the electrode powder was carefully collected from the electrodes. A sealed stainless steel pan with a gold-plated copper seal was used to collect equal weights of the electrode powder and a fresh electrolyte. The measurements were conducted over the range of 50–400 ℃ at a heating rate of 10 ℃·min^{-1}.

3.2.4 Electrochemical measurements

The electrochemical performance of the cathode materials was evaluated in a CR2032 coin-type cell. The cell consisted of an NCM cathode and a lithium metal anode separated by a porous ceramic-coated polyethylene film. The composite cathode was fabricated by spreading a slurry consisting of the active material (92 wt.%), Denka black (4 wt.%), and polyvinylidene difluoride (4 wt.%) in N-methyl-2-pyrrolidone on aluminum foil, which was used as the current collector. The electrodes were dried at 120 ℃ under vacuum and roll-pressed. The

electrolyte solution consisted of $LiPF_6$ (1.0 M) dissolved in a mixture of fluoroethylene carbonate and dimethylene carbonate. All the cell fabrication steps, including the slurry casting and assembly of coin cells, were conducted in a dry room.

The assembled cells were discharged/charged galvanostatically at a constant current. Three samples were tested for each type of sample, and the loading level was 10 mA h/cm^2. The electrochemical activities of the cathodes were characterized via EIS with a Solartron 1260 frequency response analyzer with an applied frequency ranging from 10 mHz to 1 MHz. EIS measurements were performed in the initial state and then the discharged state after one charge-discharge cycle.

3.2.5 Long-term cyclability test using cylindrical-type 18650 full cells

Cylindrical-type 18650 cells were fabricated to analyze the long-term cyclability and quantify the evolution of gas from NCM/graphite full cells. The electrochemical performances of the cylindrical-type 18650 cells were evaluated in a temperature-controlled chamber at 45 ℃. The cells were cycled up to 300 cycles between 2.8 and 4.35 V at a rate of 1 C. A specific capacity check was made every 100 cycle during long-term cycling.

3.2.6 Computational details

In order to understand the effect of introduction of MOF on Ni-rich NCM, the surfaces of $LiNiO_2$ are modeled using $LiNiO_2$ slabs and the first principle calculations are carried out. The $LiNiO_2$ slabs contain 6 Li layers, 6 Ni layers and 12 O layers and O layers are located between Li layer and Ni layer, where the slabs have (0003) surface of (R3m) $LiNiO_2$ structures. Each layer has 4 atoms and so the $LiNiO_2$ slabs are composed of 24 Li, 24 Ni and 48 O atoms. The positions of atoms in the lower 3 Li layers, 3 Ni layers and 6 O layers are fixed to reflect the bulk properties and the other atoms in upper parts are relaxed. The first principle calculations are performed using the Vienna ab initio simulation package (VASP) [93,94] within the Projector-Augmented-Wave (PAW) method[95]. The exchange correlation interactions are included with the generalized gradient approximation Perdew-Burke-Ernzerhof (GGA-PBE) functional [96] and the plane wave cutoff energy is set to be 500 eV. The structure relaxations are carried out with a criteria of 10^{-4} eV for the total energy and 0.02eV/Å for the forces on each atom. The effective on-site Hubbard Ueff correction, 6.885eV and 5.96eV on the 3d electrons for Ni and Co atoms is employed, respectively.[97]

3.3 Results and discussion

3.3.1 Material Characterization

The properties of Ni-rich NCM ($LiNi_{0.80}Co_{0.15}Mn_{0.05}O_2$) during heat treatment were investigated in order to elucidate the surface modification by ZIF-67. Figure 3.1 shows thermal gravimetric analysis (TGA) curves of bare and 6 wt.% MOF-treated Ni-rich NCM, along with schematic illustrations describing the corresponding mechanisms. The TGA curve of ZIF-67 is also presented in Figure 3.8. First, the TGA curve of MOF-treated Ni-rich NCM showed a dramatic change at ~350 ℃. ZIF-67 also emitted CO_x, NO_x, and H_2O as products of oxidative decomposition in air from 350 ℃ (Figure 3.8)[90,98,99]. This indicates that dodecahedral ZIF-67 crystals, ~250 nm in size, on the surface of the active particles began to decompose upon heating (Figure 3.1(b)). Furthermore, immediately after the decomposition of ZIF-67 (Figure 3.1(c)), only the Co ions of ZIF-67 remained on the surface of Ni-rich NCM at higher temperatures. The remaining Co ions can diffuse through the surface of the NCM particles; it can be seen from the thermodynamic calculation as shown in Figure 3.14 that the Co-O bond in this process is more thermodynamically stable than other bonds such as Ni-O in the MOF. Up to 800 ℃, MOF-treated Ni-rich NCM showed 4.3 wt.% mass loss, in contrast to 0.6 wt.% loss from the bare sample. According to inductively coupled plasma atomic emission spectroscopy (ICP-AES) analysis, ZIF-67 consists of ca. 23 wt.% cobalt (Table 3.1). In the

case of 6 wt.% ZIF-67 being applied, 2.3 wt.% of CoO_x (corresponding to ca. 1.38 wt.% of Co ions) was finally dispersed on the surface of Ni-rich NCM. After thermal decomposition, The Co of CoO_x is likely to be a mixed form of divalent and trivalent as shown in Figure 3.16(a). Because Co_3 (II, III) O_4 (Figure 3.16(b)), is known to be stable at around from 600 to 700 ^oC and Co (II) O is stable at over 900 ^oC [100].

$$2Co_3O_4 \leftrightarrow 6CoO + O_2$$

The morphology of the primary/secondary particles of Ni-rich NCM after MOF treatment was investigated by scanning electron microscopy (SEM). The SEM images of bare Ni-rich NCM, and 1 and 6 wt.% MOF-treated Ni-rich NCM are shown in Figure 3.2 along with magnified images in the inset. The rough surface of the bare sample was covered with lithium impurities (such as Li_2CO_3 and LiOH), which changed to a relatively smooth surface for the 1 wt.% MOF-treated Ni-rich NCM (Figure 3.2 (a) and Figure 3.2 (b) without smaller MOF particles on the surface (Figure 3.2 (d). Furthermore, a drastic change in the morphology of the primary particles was observed for 6 wt.% MOF-treated Ni-rich NCM; it has a distinct polygonal shape with a completely clear surface as shown in the magnified image in Figure 3.2(c).

The microstructural changes in 6 wt.% MOF-treated Ni-rich NCM were further investigated by high-angle annular dark field scanning transmission electron microscopy (HAADF-STEM)

and electron energy loss spectroscopy (EELS) (Figure 3.3), respectively. The shape and atomic distribution (Ni and Co) of Ni-rich NCM primary particles barely changed after a small amount (1 wt.% MOF) was added (Figure 3.9). Hence, I focused on the physical properties of 6 wt.% MOF-treated Ni-rich NCM to understand the effects of 1 wt.% MOF treatment on the microstructure. As shown in Figure 3.3(e) and 3.3(f), the cross-sectional image of the Ni-rich NCM showed a considerable change in the polygonal shape with the introduction of 6 wt.% MOF, as confirmed by the SEM images in Figure 3.2. In addition, the primary particles of 6 wt.% MOF-treated Ni-rich NCM contained numerous micropores with various sizes compared to the bare sample (Figure 3.3(a) and 3.3(b)). Irregular pores were newly formed between the primary particles. The density of the micropores in 6 wt.% MOF-treated Ni-rich NCM and the total surface area determined via Brunauer-Emmett-Teller (BET) analysis increased (Table 3.2), which was also confirmed by the pore volume distribution (Figure 3.10), whereas untreated and 1 wt.% MOF-treated Ni-rich NCM showed similar low surface areas. On the other hand, when 6 wt.% MOF is introduced, the introduction amount of pure Co was about 1wt.% from the previous TGA result (Figure 3.8). I compared the particle shape of Ni-rich NCM (Figure 3.17) with 8wt.% of Co through conventional surface treatment based on evaporation method. The pore formation by MOF shown in Figure 3.3 was much bigger change than the phenomenon that occurs when 8 times as much Co amount is applied as the evaporation

method based on the amount of Co introduced. In other words, using thermal decomposition of MOF can be a very effective way to make a bigger change than the existing processes even with less amount of surface treatment material.

In contrast to the concentration gradient of Ni and Co in the primary particles of untreated Ni-rich NCM (Figure 3.3(c) and 3.3(d), a higher Co content, especially on the surface and pore boundaries of the primary particles, was observed for the 6 wt.% MOF-treated sample (Figure 3.3(g) and 3.3(h) due to the additional Co from the MOF coating the particle surfaces. These significant changes in the morphology and Co ion distribution could be induced by galvanic replacement reactions [92,99,101]. The porous microstructure of the 6 wt.% MOF-treated Ni-rich NCM shown in Figure 3.3(e)–3.3(h) also resulted from the galvanic replacement reactions that are relevant to Kirkendall effect[101]. The driving force for this reaction is the difference between the reduction potential of Ni and Co, where exchange is enhanced by the sub-micron size of the primary particles; Ni and Co can easily diffuse through melted residual lithium (e.g., Li_2CO_3-LiOH) during heat treatment [26]. I also model $LiNiO_2$ structure (Figure 3.14(a)) and calculate the heat of formation of Co atoms for the first three surface Ni layers and bulk $LiNiO_2$ (3.14(b)). The heats of formation are -0.34eV, -0.28eV, -5.81eV and -0.692eV for Co atoms at the first, the second, the third Ni layer from surface and bulk $LiNiO_2$, respectively. Co atoms are mainly located inside the cathode particles rather than around the surface.

The morphological change in the primary particles indicated a possible change in the crystal structure of Ni-rich NCM by the MOF treatment. Therefore, the structural changes of Ni-rich NCM induced by the MOF addition were studied by X-ray diffraction (XRD) analysis. Figure 3.4 shows the normalized XRD patterns of the bare Ni-rich NCM, and 1 and 6 wt.% MOF-treated samples. The main peaks of the MOF (Figure 3.11) disappeared after the heat-treatment of 1 and 6 wt.% MOF-treated Ni-rich NCM due to oxidative decomposition of the MOF at high temperatures (>350 ℃) in air. The variation in the characteristic peak intensities and evolution of other peaks (as labeled in Figure 3.4) for 6 wt.% MOF-treated Ni-rich NCM was a result of some parts of the layered structure being transformed into secondary phases after MOF treatment; both the spinel- and rocksalt-like secondary phases were observed in the material [14]. The changes in the XRD profiles and morphology (Figure 3.2, 3.3, and 3.4) indicated the formation of a new phase after the addition of MOF.

Further investigations of the phase transition of the untreated and MOF-treated samples were performed using high-resolution (HR)-TEM and fast Fourier transform (FFT) pattern analysis, as presented in Figure 3.5. Based on the changes in the shape of primary particles and the XRD pattern of Ni-rich NCM after MOF treatment, phase transitions were expected. In general, changes in phase and morphology of the particles induced by the surface treatment of the cathode materials are limited to the outermost surface layer[83]. Therefore, magnified

images of the surface region of the primary particles (Figure 3.5(b) and 3.5(f) and their corresponding FFT images (Figure 3.5(c)–3.5(d) and 3.5(g)–3.5(i)) were analyzed to compare the phases in the inner and outer regions. The inner region of the primary particles of untreated (Figure 3.5(c)) and MOF-treated Ni-rich NCM (Figure 3.5(g)) commonly showed a layered structure (R-3m, rhombohedral) from the FFT analysis. However, after MOF addition, another hexagonal structure, such as the spinel-like (Fd-3m) mixed with the rocksalt-like phase (Fm-3m), was sparsely observed at the edge region near the surface of primary particles for the 6 wt.% MOF-treated Ni-rich NCM (Figure 3.5(h) and 3.5(i)) while maintaining the layered structure (Figure 3.5(d)) of the bare sample. In particular, a spinel-like phase was stabilized between the layered and rocksalt-like phase, as shown in Figure 3.5(h). Hence, a stable Co- and Ni-rich domain with a spinel-like phase could be formed on the surface of the 1 wt.% MOF-treated Ni-rich NCM, considering that layered phase transforms to an intermediate spinel-like phase and then rocksalt-like phase in stages through the migration of the transition metal ions [69], although a small portion of spinel-like domain was rarely found (Figure 3.12). The phase transformation on the surface of MOF-treated Ni-rich NCM particles is also closely related with the galvanic replacement reactions[92,101]. There were several indications for these phenomena during the surface treatment of MOF. First, during the post-heat treatment at 700 ℃, individual Co ions were released from the thermally decomposed MOF (ZIF-67)

structures, which were finally oxidized to reactive CoOx with molecular-scale size. The difference between the electrochemical potential of Co ions released from the MOF and the Ni ions in the active material is the major driving force initiating this reaction. Hence, the Co^{2+} ions in the CoOx could be oxidized to Co^{3+} ions and then be incorporated into the octahedral sites of Ni^{3+} in the surface layered structure of Ni-rich NCM due to the similar ionic radius and electronic configuration of Co^{3+} and Ni^{2+} (Co^{3+} = 0.55 Å and Ni^{3+} = 0.56 Å)[44,103]. Furthermore, it is favorable for the Ni^{3+} ions to undergo reduction during the galvanic replacement reactions between Co and Ni ions to achieve charge compensation; some of the Ni^{3+} ions (≤ 1.38 wt.% of Co ions confirmed by the TGA analysis in Figure 1) were converted to Ni^{2+} ions. The Ni^{2+} ions (0.69 Å) readily migrate to the neighboring vacant Li^{+} ion (0.76 Å) sites by the incorporation of Co^{3+} ions into the original Ni^{3+} sites[84–86]. Here, the vacant Li^{+} sites on the surface lattice structure of the active material were a result of the formation of Li-deficient Ni-rich NCM ($Li_{1-x}Ni_{0.80}Co_{0.15}Mn_{0.05}O_2$) structure and melted residual Li on the surface of the active material, which acted as pathways for exchanging Ni and Co ions at high temperatures. These variations in the oxidation states and atomic migration of Ni^{2+} and Co^{3+} ions contributed to the transformation of the surface of the Ni-rich NCM from a layered oxide phase (R-3m) to a more stable spinel-like phase (Fd-3m)[104].

3.3.2 Electrochemical performances and thermal stability

The charge–discharge cycling tests for bare Ni-rich NCM, and 1 and 6 wt.% MOF-treated Ni-rich NCM were performed using coin-type 2032 half cells and cylindrical-type 18650 full cells (Ni-rich NCM|graphite) in the voltage range of 2.8–4.35 V (vs. Li^+/Li), and the results are presented in Figure 3.6. It was confirmed from the results of half-cell tests that 1 wt.% MOF-treated Ni-rich NCM showed higher charge–discharge capacity (210 mA·h/g) than the untreated sample (207 mA·h/g) at the current density of 0.1C-rate. However, 6 wt.% MOF-treated Ni-rich NCM showed low irreversible charge–discharge capacity, which is attributed to an excessive amount of rocksalt-like secondary phase, as previously confirmed in the crystallographic analyses (Figure 3.4 and 3.5). Moreover, the 1 wt.% MOF-treated Ni-rich NCM with a minor amount of stable Co- and Ni-rich spinel-like phase shows better cyclability (1C-rate) than the bare sample (95.1 and 92.5% after 50 cycles, respectively) at room temperature (Figure 3.6(b). Further, the long-term cycle performance (1C-rate) of 18650 full cells at a high temperature of 45 ℃ was evaluated to examine the accelerated changes in the structure of the cathode material during cycling (Figure 3.6(c). The capacity retention of the 1 wt.% MOF-treated Ni-rich NCM increased from 71.0% to 81.5% after 300 cycles. To further understand the improved electrochemical performance of the MOF-treated Ni-rich NCM, electrochemical impedance spectroscopy (EIS) analysis was performed for the untreated and 1

wt.% MOF-treated Ni-rich NCM. The EIS data after 50th cycles are shown in Figure 3.13. The impedance spectra of the samples showed semicircles, which were related to the resistance of charge transfer at the cathode–electrolyte interface. The lower charge transfer resistance (ca. 23.5 Ω) for the 1 wt.% MOF-treated Ni-rich NCM than that (ca. 30.4 Ω) for the untreated material originated from the stabilized surface layer with less structural degradation on the cathode after MOF treatment.

In Figure 3.7, the changes in the phase and thermal stability of untreated and MOF-treated Ni-rich NCM were evaluated by differential scanning calorimetry (DSC) analysis. Two main exothermic peaks were observed at 220 and 280 ℃. The thermal stability improved after MOF treatment, indicated by the intensity of both peaks decreasing with increasing MOF content. The heat capacity, which is the integral value of heat flow, was also decreased with increasing MOF content, showing values of ~2160, 2147, and 1511 J/g, for 0, 1, and 6 wt.% MOF treatment, respectively. Delithiated Ni-rich layered oxides are known to thermally decompose to the spinel structure at ~220 ℃, and then transform into the rocksalt structure at ~280 ℃ [17,40,69]. Both peak intensities related to the thermal decomposition decreased with increasing MOF content as some spinel- and/or rocksalt-like secondary phases existed on the surface. Furthermore, the extent of phase transition from the layered structure to the spinel- or rocksalt-like structure during thermal decomposition decreased during MOF treatment, finally

contributing to the improved thermal stability. These results agree well with the electrochemical tests described above indicating that the formation of the stable spinel-like domain on the layered surface structure of Ni-rich NCM with 1 wt.% MOF treatment imparts improved structural stability to the material even at elevated temperatures. Consequently, these brand-new MOF-assisted phase-transitions contribute to the improvements in thermal and electrochemical stability of the Ni-rich layered cathode materials.

3.4 Conclusions

A novel approach of introducing Co on the surfaces of Ni-rich NCM cathode materials for Li-ion batteries using Co-embedded ZIF-67 (a mass-producible MOF) was developed, which enhanced their charge–discharge performance and thermal stability. During the post-heat treatment, ZIF-67 on the surface of the Ni-rich NCM thermally decomposed and the residual Co was incorporated into the layered Ni-rich NCM, followed by structural changes via phase transformation from the layered to a spinel-like structure. Electrochemical tests indicated enhanced cyclability of MOF-treated Ni-rich NCM. In particular, the capacity retention (1C-rate) of the cylindrical-type 18650 full cell (Ni-rich NCM/graphite) increased from 71.0% to 81.5% after 300 cycles at 45 ℃. The thermal stability of MOF-treated Ni-rich NCM also

increased with increasing MOF content, as determined by DSC. Finally, the phase transition induced by the MOF treatment formed thermally and electrochemically stable spinel-like structure on the Ni-rich NCM cathode materials.

Sample	ICP-AES, %w/w			
	Li	Mn	Co	Ni
ZIF-67	-	-	22.76	-

Table 3.1 Inductively coupled plasma-atomic emission spectrometry (ICP-AES) results for MOF (ZIF-67).

Sample	$a_{s,BET}$ [m^2 g^{-1}]
Bare Ni-rich NCM	0.47954
1 wt.% MOF-treated	0.48603
6 wt.% MOF-treated	1.4141

Table 3.2 Results of Brunauer-Emmett-Teller (BET) analysis of N_2 adsorption–desorption isotherms for bare, 1 wt.% MOF-treated, and 6 wt.% MOF-treated Ni-rich NCM.

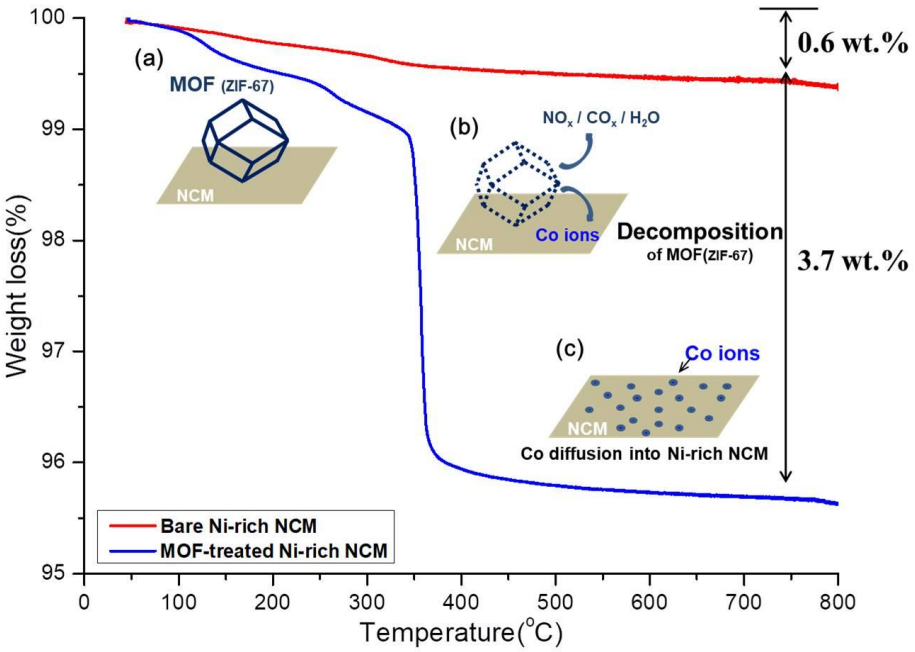

Figure 3.1 TGA curves and schematic diagrams showing the corresponding mechanisms up to 800 ℃ to the MOF-treated Ni-rich NCM compared to the uncoated control sample. (a) MOF (ZIF-67) attached to the Ni-rich NCM surface, (b) oxidative decomposition of MOF (ZIF-67) during heat treatment in air, and (c) remnant Co ions embedded on the Ni-rich NCM surface.

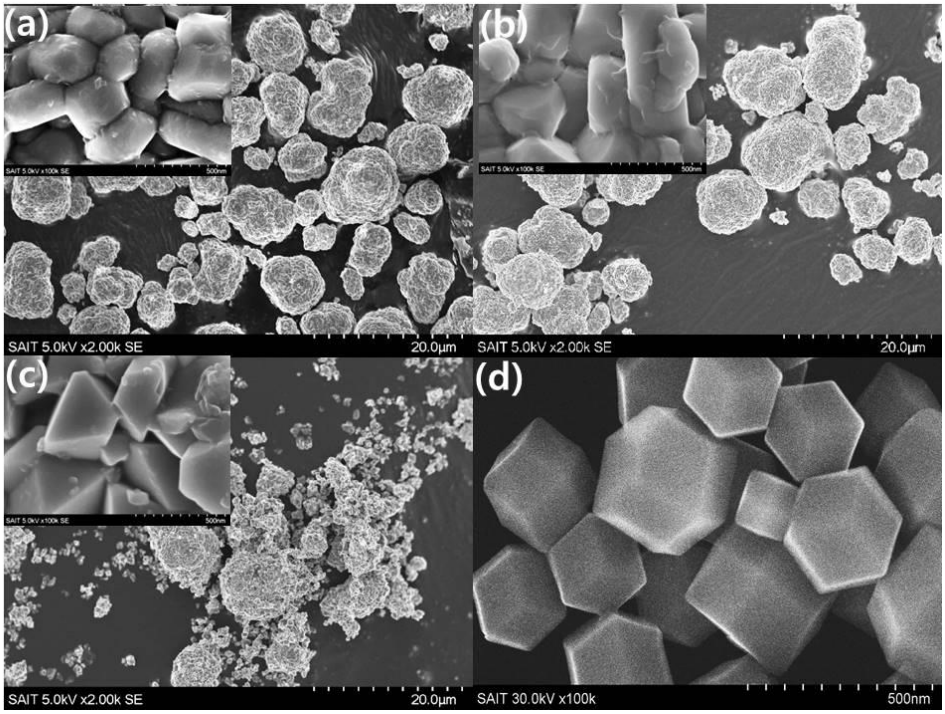

Figure 3.2 SEM images of (a) bare Ni-rich NCM, (b) 1 wt.% MOF-treated Ni-rich NCM, (c) 6 wt.% MOF-treated Ni-rich NCM, and (d) as-synthesized MOF. The insets show magnified images.

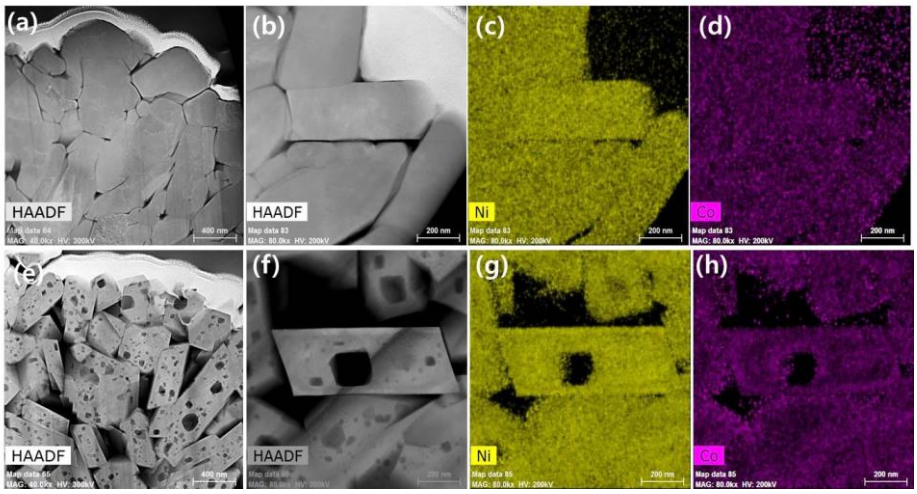

Figure 3.3 Cross-sectional high-angle annular dark field scanning transmission electron microscopy (HAADF-STEM) images and magnified images of (a,b) bare Ni-rich NCM and (e,f) 6 wt.% MOF-treated Ni-rich NCM. The corresponding EELS spectra (Ni, Co) of (c,d) bare and(g,h) 6 wt.% MOF-treated Ni-rich NCM.

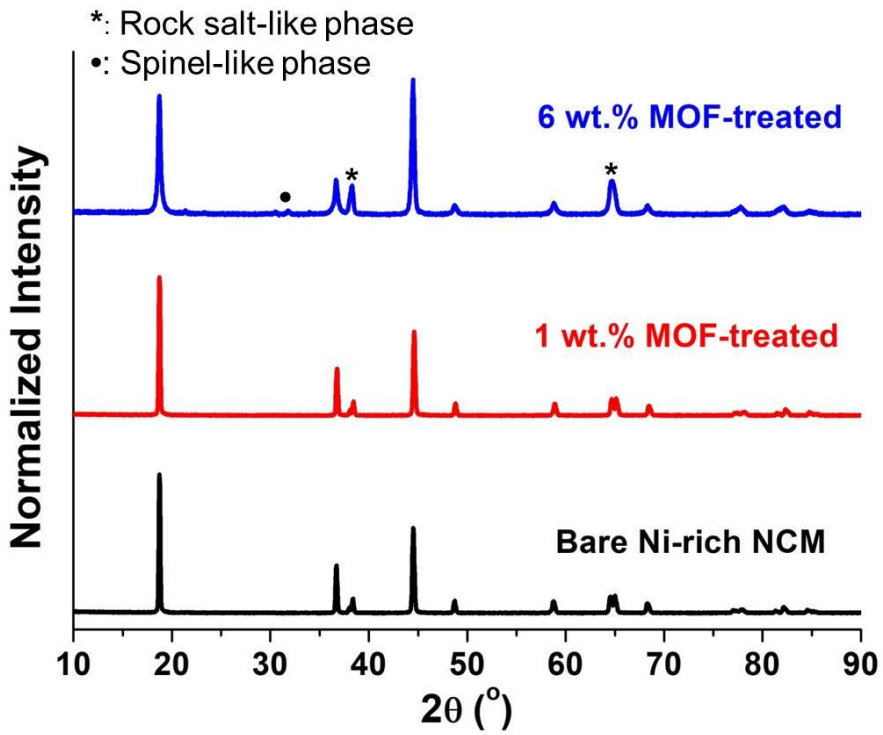

Figure 3.4 Normalized XRD patterns of (a) bare Ni-rich NCM, (b) 1 wt.% MOF-treated Ni-rich NCM, and (c) 6 wt.% MOF-treated Ni-rich NCM.

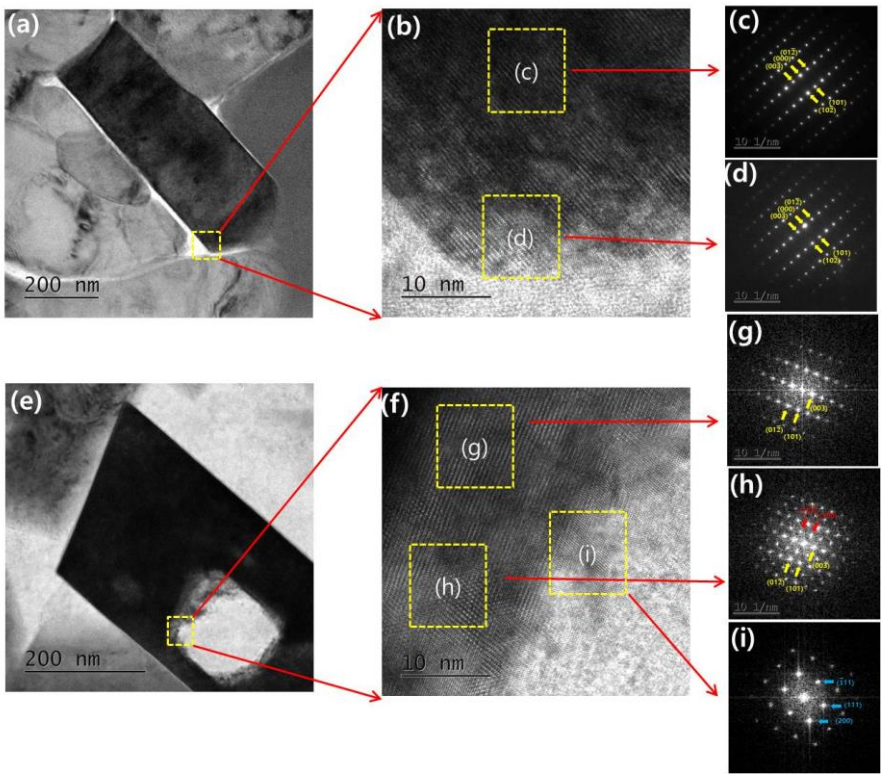

Figure 3.5 High-resolution transmission electron microscopy (HR-TEM) and fast Fourier transform (FFT) patterns of bare (a–d) and 6 wt.% MOF-treated Ni-rich NCM (e–i).

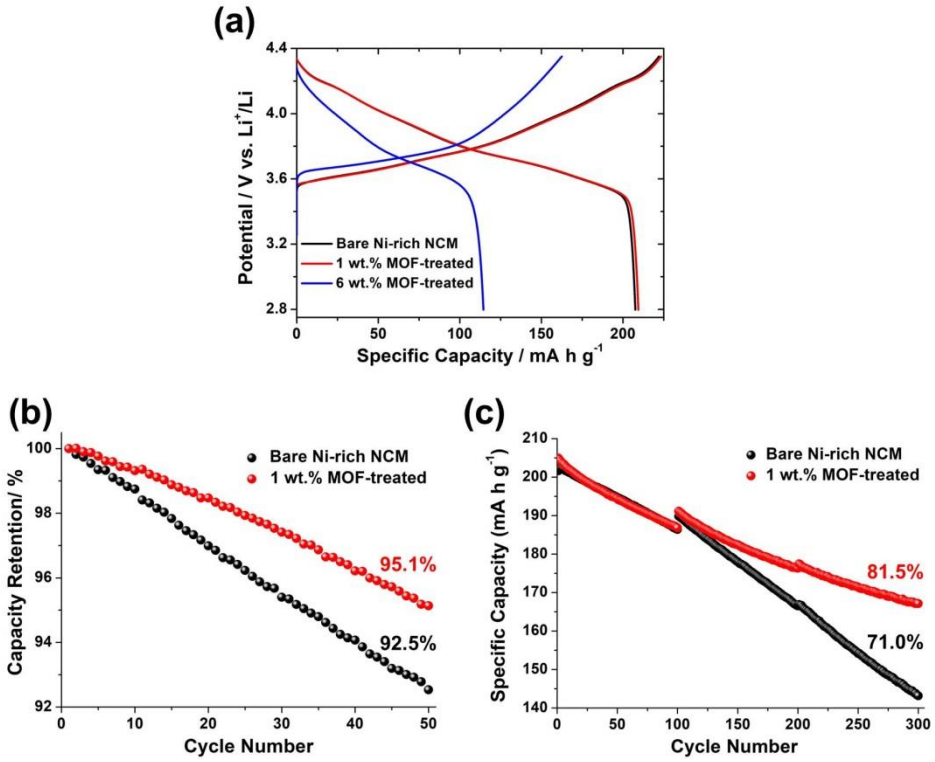

Figure 3.6 . (a) First charge–discharge curves between 2.8 and 4.35 V (vs. Li+/Li) at 0.1 C rate and the resulting 1C cyclability of bare, 1 wt.% MOF-treated, and 6 wt.% MOF-treated Ni-rich NCM at (b) room temperature and (c) 45 ℃.

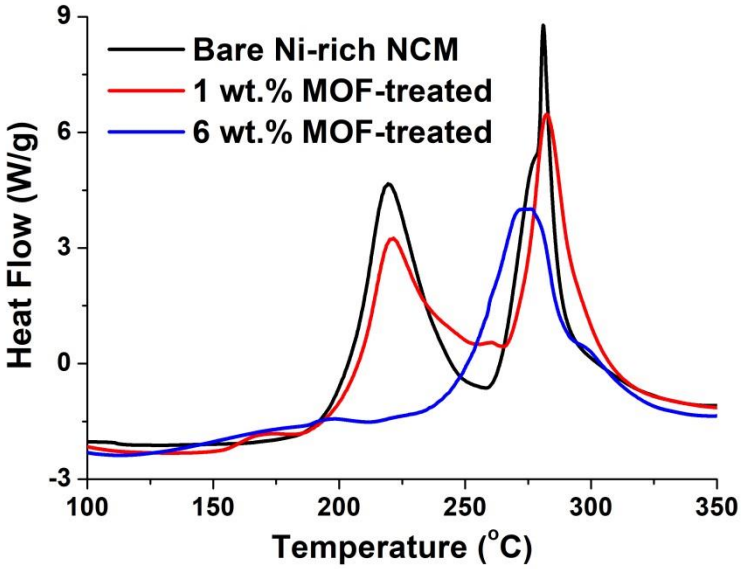

Figure 3.7 Differential scanning calorimetry (DSC) curves for bare, 1 wt.% MOF-treated, and 6 wt.% MOF-treated Ni-rich NCM charged to 4.35 V.

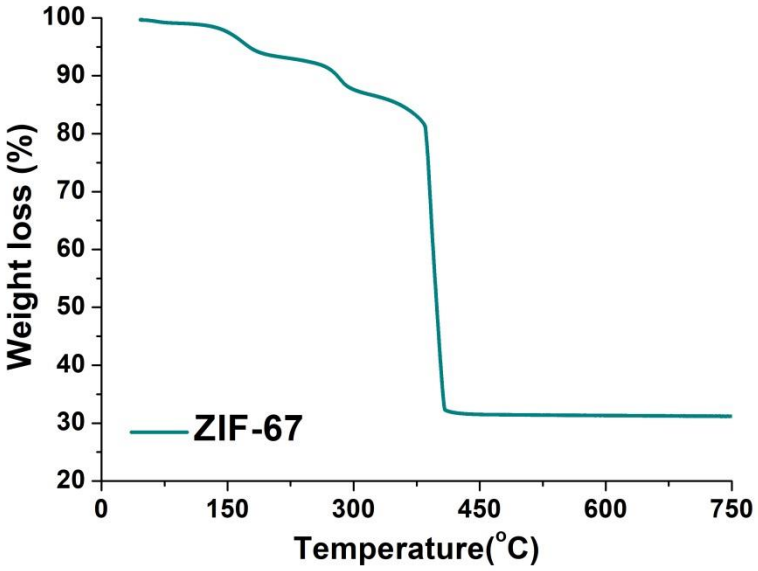

Figure 3.8 Thermogravimetric analysis curve of metal-organic framework ZIF-67 up to 750 ℃

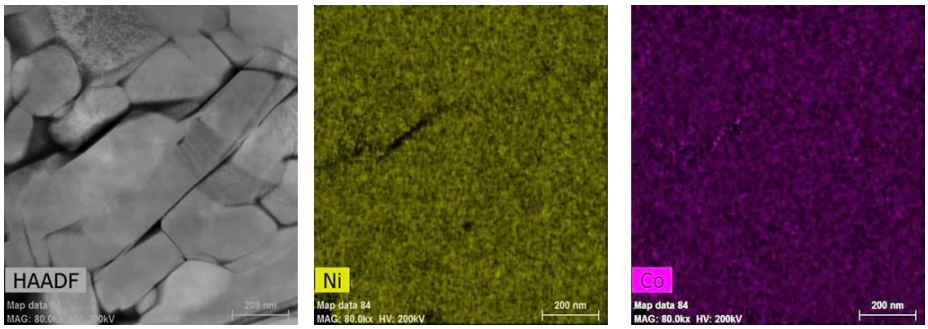

Figure 3.9 Cross-sectional high-angle annular dark field scanning transmission electron microscopy (HAADF-STEM) images and the corresponding EELS spectra (Ni, Co) of 1 wt.% MOF-treated Ni-rich NCM.

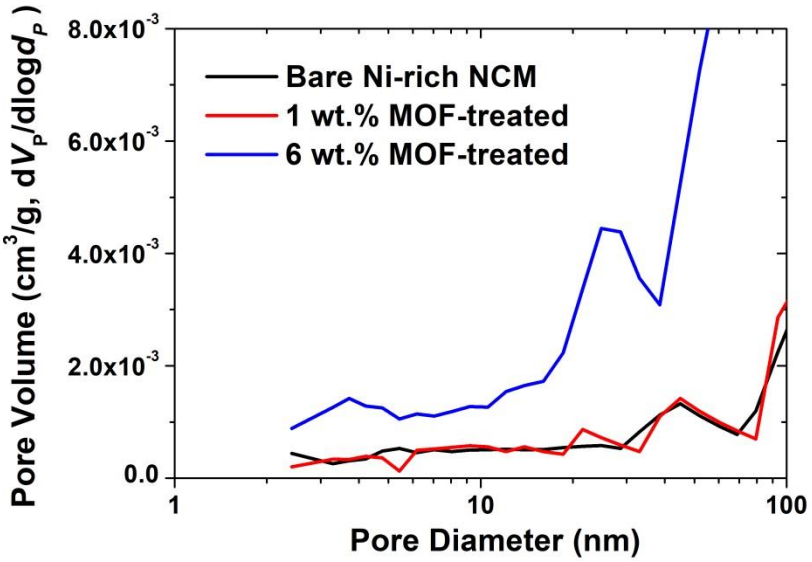

Figure 3.10 Pore size distributions of bare, 1 wt.% MOF-treated, and 6 wt.% MOF-treated Ni-rich NCM.

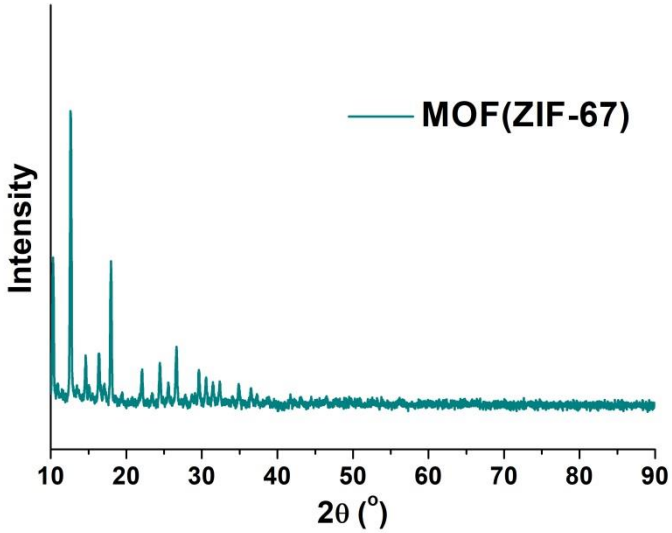

Figure 3.11 X-ray diffraction pattern of MOF (ZIF-67).

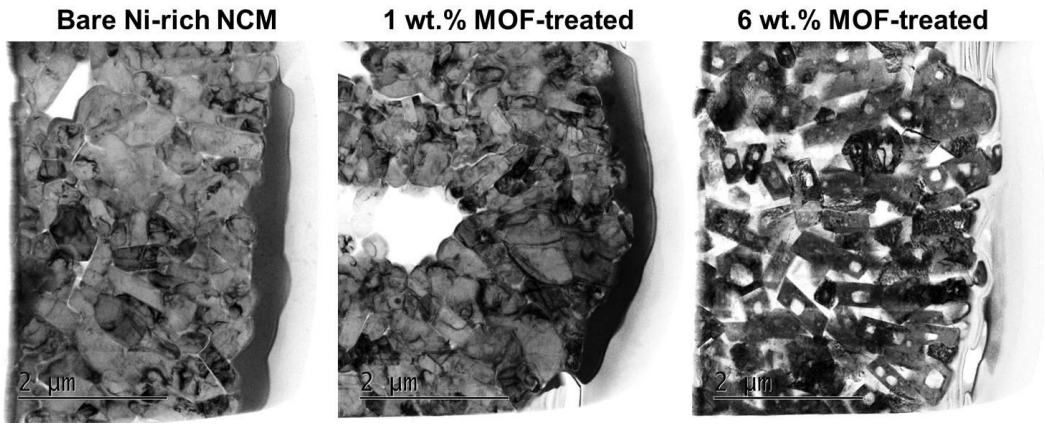

Figure 3.12 Changes in the particle morphology of Ni-rich NCM with increasing MOF content.

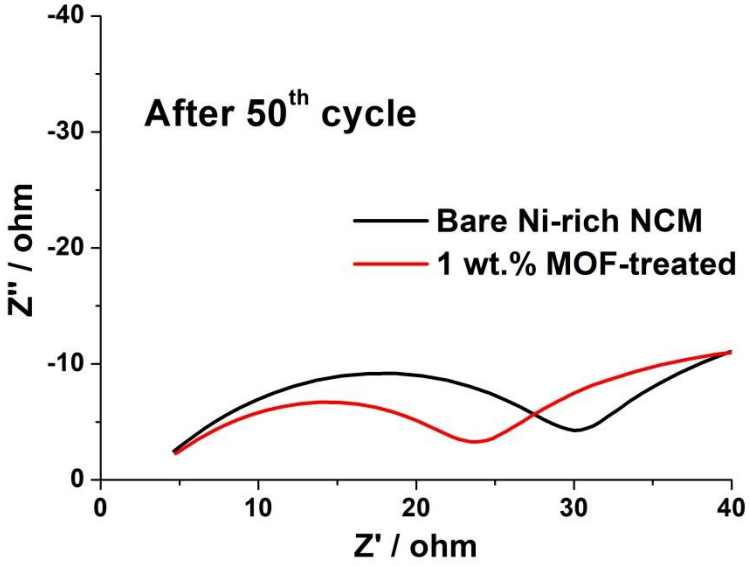

Figure 3.13 EIS data for bare, and 1 wt.% MOF-treated Ni-rich NCM after the 50th cycles.

(a)

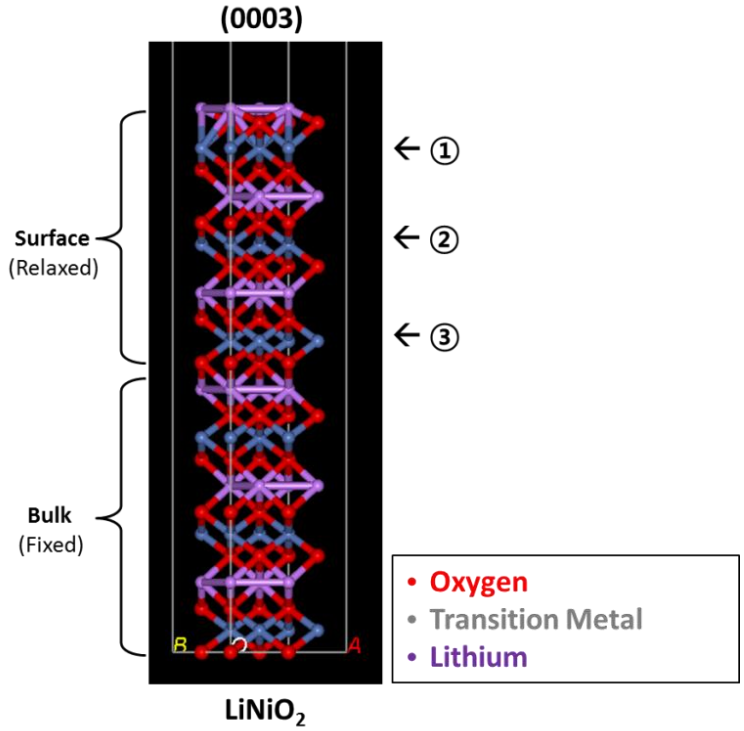

(b)

Co		H_f(eV)
Surface	①	-0.340
	②	-0.278
	③	-0.581
Bulk		-0.692

Figure 3.14. (a) The model of the $LiNiO_2$ near surface and (b) the first principle calculation results

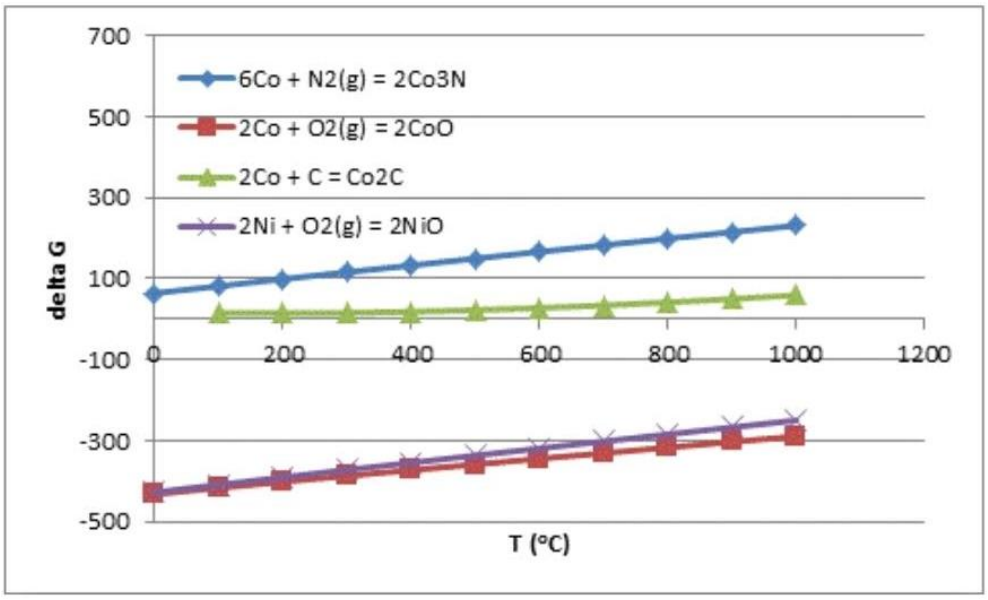

Figure 3.15 Thermodynamics calculation of stability with temperature (Calculated by Heechul Jung (SAIT) using HSC chemistry)

(a)

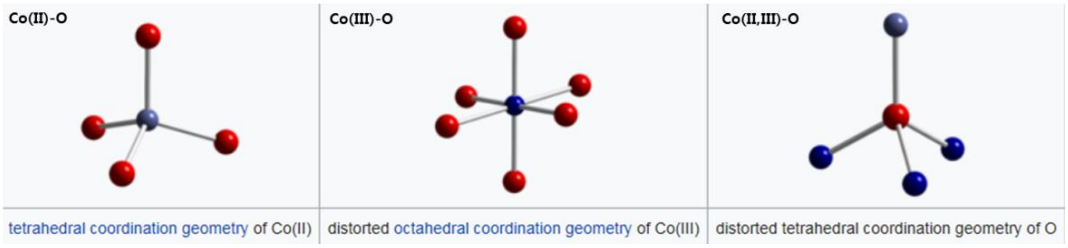

(b)

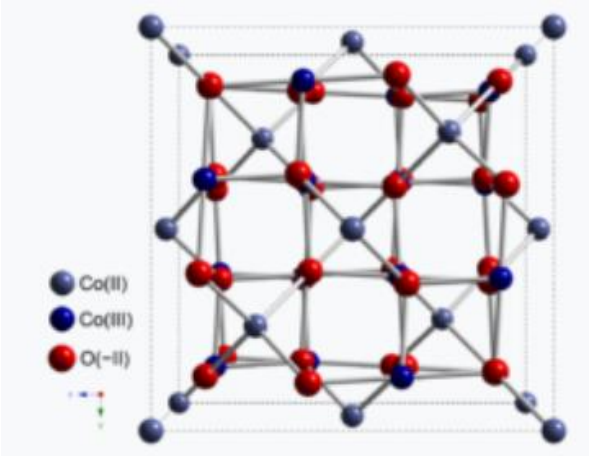

Figure 3.16 (a) various coordination between Co and O, and (b) the unit cell of Co_3O_4 [100].

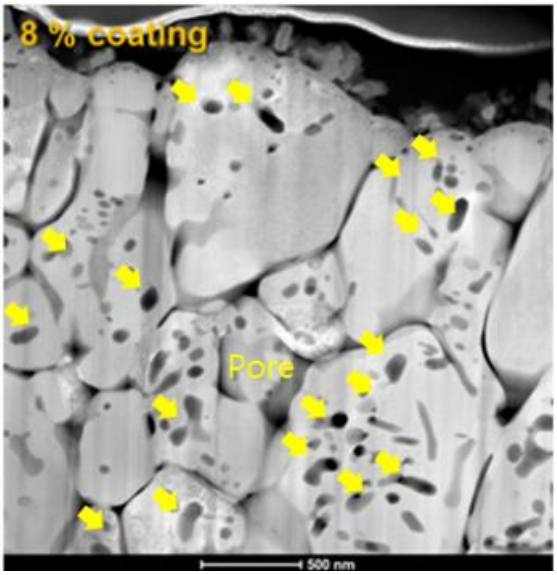

Figure 3.17 SEM images of conventional surface treatment (8 wt.% of Co) by conventional wet process.

Chapter 4.
Conclusions

Layered oxides such as OLO and Ni-rich layered oxides are the most balanced material to meet the high energy density and safety requirement.

Among layered ternary cathode materials, Ni-rich layered oxides (Ni-rich NCM with ≥70 mol.% of Ni and the remainder Co and Mn), are also good candidates as cathode materials due to their high capacity. However, the presence of surface residual lithium, which source of gas evolution, is an inevitable result of the manufacturing process of Ni-rich layered oxides.

Transition metal (TM = Al, Co, and Fe) phosphate coatings prepared by wet chemical deposition were used to enhance the electrochemical performance of $Li_{1.0}Ni_{0.8}Co_{0.15}Mn_{0.05}O_2$ (NCM) positive electrode materials, with the observed effects depending on the used metal and the TM/P ratio. In all cases, coating decreased the content of Li residuals, implying that these species were converted into other compounds during the coating process. Al/P was the most effective coating material, whereas Fe/P-coated NCM samples showed performances similar to that of pristine NCM. Considering the removal of Li residuals in addition to capacity and capacity retention, a 1:1 Co/P coating proved to be most effective for surface modification, achieving initial capacity and capacity retention increases of 10 mAh g^{-1} and 3%, respectively, as compared to the pristine material. Moreover, the beneficial effect of this coating was also confirmed for the more Ni-rich $Li_{1.0}Ni_{0.91}Co_{0.06}Mn_{0.03}O_2$.

Reducing the amount of residual lithium by washing the Ni-rich NCM is an important

process to facilitate the commercialization of this promising cathode material. A fundamental understanding of the reactions associated with washing is required to optimize the washing process, which was the focus of this investigation. The surface composition of the Ni-rich NCM, which includes a residual lithium layer, was dramatically altered by the parameters used in the washing process.. Although the residual lithium is most effectively removed by increasing the amount of water used for washing, the cycling performance decreases with increasing water use. The optimal water/NCM ratio for washing was determined to be 1:1. The resulting CRR was improved from 84.6% to 86.1%, and the gas evolution was reduced by &25% compared with the unwashed sample.

Nanosized δ-$VOPO_4$ synthesized using a reflux method and a ball milling was coated onto OLO using a mechanofusion technique. As a result, the irreversibility of the first charge-discharge cycle, which is an intrinsic problem of OLO positive electrodes, was considerably reduced by the application of $VOPO_4$, which provided additional lithium intercalation sites for discharge. Importantly, surface-coated $VOPO_4$ positively affected cycling lifetime and thermal stability.

A novel approach of introducing Co on the surfaces of Ni-rich NCM cathode materials for Li-ion batteries using Co-embedded ZIF-67 (a mass-producible MOF) was developed, which enhanced their charge–discharge performance and thermal stability. During the post-heat

treatment, ZIF-67 on the surface of the Ni-rich NCM thermally decomposed and the residual Co was incorporated into the layered Ni-rich NCM, followed by structural changes via phase transformation from the layered to a spinel-like structure. The phase transition induced by the MOF treatment formed thermally and electrochemically stable spinel-like structure on the Ni-rich NCM cathode materials.

References

[1] J.M. Tarascon, M. Armand, Issues and challenges facing rechargeable lithium batteries, Nature. 414 (2001) 359–367. doi:10.1109/ICUWB.2008.4653360.

[2] B. Dunn, H. Kamath, J.M. Tarascon, Electrical energy storage for the grid: A battery of choices, Science (80-.). 334 (2011) 928–935. doi:10.1126/science.1212741.

[3] M.M. Thackeray, C. Wolverton, E.D. Isaacs, Electrical energy storage for transportation - Approaching the limits of, and going beyond, lithium-ion batteries, Energy Environ. Sci. 5 (2012) 7854–7863. doi:10.1039/c2ee21892e.

[4] J. Vetter, P. Novák, M.R. Wagner, C. Veit, K.C. Möller, J.O. Besenhard, M. Winter, M. Wohlfahrt-Mehrens, C. Vogler, A. Hammouche, Ageing mechanisms in lithium-ion batteries, J. Power Sources. 147 (2005) 269–281. doi:10.1016/j.jpowsour.2005.01.006.

[5] D. Mohanty, S. Kalnaus, R.A. Meisner, K.J. Rhodes, J. Li, E.A. Payzant, D.L. Wood, C. Daniel, Structural transformation of a lithium-rich Li1.2Co0.1Mn0.55Ni0.15O2cathode during high voltage cycling resolved by in situ X-ray diffraction, J. Power Sources. 229 (2013) 239–248. doi:10.1163/22106286-12341315.

[6] D.P. Abraham, R.D. Twesten, M. Balasubramanian, J. Kropf, D. Fischer, J. McBreen, I. Petrov, K. Amine, Microscopy and Spectroscopy of Lithium Nickel Oxide-Based Particles Used in High Power Lithium-Ion Cells, J. Electrochem. Soc. 150 (2003) A1450.

doi:10.1149/1.1613291.

[7] K. Min, S.W. Seo, B. Choi, K. Park, E. Cho, Computational Screening for Design of Optimal Coating Materials to Suppress Gas Evolution in Li-Ion Battery Cathodes, ACS Appl. Mater. Interfaces. 9 (2017) 17822–17834. doi:10.1021/acsami.7b00260.

[8] C. Liu, F. Li, L.-P. Ma, H.-M. Cheng, Advanced materials for energy storage., Adv. Mater. 22 (2010) E28-62. doi:10.1002/adma.200903328.

[9] Walter A. van Schalkwijk, Bruno Scrosati, Advances in Lithium-Ion Batteries, Kluwer Academic Publications, New York, 2002.

[10] M.S. Whittingham, Lithium batteries and cathode materials, Chem. Rev. 104 (2004) 4271–4301. doi:10.1021/cr020731c.

[11] J.B. Goodenough, Y. Kim, Challenges for rechargeable Li batteries, Chem. Mater. 22 (2010) 587–603. doi:10.1021/cm901452z.

[12] K. Ozawa, Lithium-ion rechargeable batteries with LiCoO2 and carbon electrodes: the LiCoO2/C system, Solid State Ionics. 69 (1994) 212–221. doi:10.1016/0167-2738(94)90411-1.

[13] R. Hausbrand, G. Cherkashinin, H. Ehrenberg, M. Gr??ting, K. Albe, C. Hess, W. Jaegermann, Fundamental degradation mechanisms of layered oxide Li-ion battery cathode materials: Methodology, insights and novel approaches, Mater. Sci. Eng. B

Solid-State Mater. Adv. Technol. (2015). doi:10.1016/j.mseb.2014.11.014.

[14] A. Manthiram, J.C. Knight, S.T. Myung, S.M. Oh, Y.K. Sun, Nickel-Rich and Lithium-Rich Layered Oxide Cathodes: Progress and Perspectives, Adv. Energy Mater. (2016). doi:10.1002/aenm.201501010.

[15] A. Manthiram, W. Choi, Suppression of Mn Dissolution in Spinel Cathodes by Trapping the Protons within Layered Oxide Cathodes, (2007). doi:10.1149/1.2754387.

[16] H. Zheng, Q. Sun, G. Liu, X. Song, V.S. Battaglia, Correlation between dissolution behavior and electrochemical cycling performance for LiNi1/3Co1/3Mn1/3O2-based cells, J. Power Sources. 207 (2012) 134–140. doi:10.1016/j.jpowsour.2012.01.122.

[17] X. Zheng, X. Li, Z. Wang, H. Guo, Z. Huang, G. Yan, D. Wang, Investigation and improvement on the electrochemical performance and storage characteristics of LiNiO 2 -based materials for lithium ion battery, (2016). doi:10.1016/j.electacta.2016.01.142.

[18] Y.K. Sun, K.J. Hong, J. Prakash, K. Amine, Electrochemical performance of nano-sized ZnO-coated LiNi0.5Mn1.5O4 spinel as 5 V materials at elevated temperatures, Electrochem. Commun. 4 (2002) 344–348. doi:10.1016/S1388-2481(02)00277-1.

[19] D. Aurbach, B. Markovsky, G. Salitra, E. Markevich, Y. Talyossef, M. Koltypin, L. Nazar, B. Ellis, D. Kovacheva, Review on electrode-electrolyte solution interactions, related to cathode materials for Li-ion batteries, J. Power Sources. (2007).

doi:10.1016/j.jpowsour.2006.10.025.

[20] J. Yang, Y. Xia, Suppressing the Phase Transition of the Layered Ni-Rich Oxide Cathode during High-Voltage Cycling by Introducing Low-Content Li2MnO3, ACS Appl. Mater. Interfaces. (2016). doi:10.1021/acsami.5b09938.

[21] W. Choi, A. Benayard, J.H. Park, J. Park, S.G. Doo, J. Mun, Versatile coating of lithium conductive Li2TiF6on over-lithiated layered oxide in lithium-ion batteries, Electrochim. Acta. 117 (2014) 492–497. doi:10.1016/j.electacta.2013.11.184.

[22] K. Park, B.-S. Lee, J.-H. Park, S.-G. Hong, The synergistic effect of inert oxide and metal fluoride dual coatings on advanced cathode materials for lithium ion battery applications, Phys. Chem. Chem. Phys. Phys. Chem. Chem. Phys. 18 (2016) 15861–15866. doi:10.1039/c6cp02007k.

[23] P. Yan, J. Zheng, M. Gu, J. Xiao, J.G. Zhang, C.M. Wang, Intragranular cracking as a critical barrier for high-voltage usage of layer-structured cathode for lithium-ion batteries, Nat. Commun. 8 (2017) 1–9. doi:10.1038/ncomms14101.

[24] E.J. Lee, Z. Chen, H.J. Noh, S.C. Nam, S. Kang, D.H. Kim, K. Amine, Y.K. Sun, Development of microstrain in aged lithium transition metal oxides, Nano Lett. (2014). doi:10.1021/nl5022859.

[25] Y.K. Sun, C.S. Yoon, I.H. Oh, Surface structural change of ZnO-coated

LiNi0.5Mn1.5O4 spinel as 5 V cathode materials at elevated temperatures, Electrochim. Acta. 48 (2003) 503–506. doi:10.1016/S0013-4686(02)00717-X.

[26] Z. Chen, Y. Qin, K. Amine, Y.-K. Sun, Role of surface coating on cathode materials for lithium-ion batteries, (n.d.). doi:10.1039/c0jm00154f.

[27] S.T. Myung, F. Maglia, K.J. Park, C.S. Yoon, P. Lamp, S.J. Kim, Y.K. Sun, Nickel-Rich Layered Cathode Materials for Automotive Lithium-Ion Batteries: Achievements and Perspectives, ACS Energy Lett. 2 (2017) 196–223. doi:10.1021/acsenergylett.6b00594.

[28] D. Mohanty, K. Dahlberg, D.M. King, L.A. David, A.S. Sefat, D.L. Wood, C. Daniel, S. Dhar, V. Mahajan, M. Lee, F. Albano, Modification of Ni-Rich FCG NMC and NCA Cathodes by Atomic Layer Deposition: Preventing Surface Phase Transitions for High-Voltage Lithium-Ion Batteries, Nat. Publ. Gr. (2016). doi:10.1038/srep26532.

[29] X. Xiao, D. Ahn, Z. Liu, J.H. Kim, P. Lu, Atomic layer coating to mitigate capacity fading associated with manganese dissolution in lithium ion batteries, Electrochem. Commun. 32 (2013) 31–34. doi:10.1016/j.elecom.2013.03.030.

[30] B. Han, T. Paulauskas, B. Key, C. Peebles, J.S. Park, R.F. Klie, J.T. Vaughey, F. Dogan, Understanding the Role of Temperature and Cathode Composition on Interface and Bulk: Optimizing Aluminum Oxide Coatings for Li-Ion Cathodes, ACS Appl. Mater. Interfaces. 9 (2017) 14769–14778. doi:10.1021/acsami.7b00595.

[31] M. Aykol, S. Kirklin, C. Wolverton, Thermodynamic aspects of cathode coatings for lithium-ion batteries, Adv. Energy Mater. 4 (2014) 1–11. doi:10.1002/aenm.201400690.

[32] R. Zhao, J. Liang, J. Huang, R. Zeng, J. Zhang, H. Chen, G. Shi, Improving the Ni-rich LiNi 0.5 Co 0.2 Mn 0.3 O 2 cathode properties at high operating voltage by double coating layer of Al 2 O 3 and AlPO 4, J. Alloys Compd. 724 (2017) 1109–1116. doi:10.1016/j.jallcom.2017.05.331.

[33] N. Nitta, F. Wu, J.T. Lee, G. Yushin, Li-ion battery materials: Present and future, Mater. Today. 18 (2015) 252–264. doi:10.1016/j.mattod.2014.10.040.

[34] X. Xiong, Z. Wang, G. Yan, H. Guo, X. Li, Role of V2O5 coating on LiNiO2-based materials for lithium ion battery, J. Power Sources. (2014). doi:10.1016/j.jpowsour.2013.06.133.

[35] M.-J. Lee, M. Noh, M.-H. Park, M. Jo, H. Kim, H. Nam, J. Cho, The role of nanoscale-range vanadium treatment in LiNi 0.8 Co 0.15 Al 0.05 O 2 cathode materials for Li-ion batteries at elevated temperatures, (n.d.). doi:10.1039/c5ta01571e.

[36] K. Heo, J.-S. Lee, H.-S. Kim, J. Kim, J. Lim, Enhanced Electrochemical Performance of Ionic-Conductor Coated Li[Ni 0.7 Co 0.15 Mn 0.15]O 2, J. Electrochem. Soc. 164 (2017) A2398–A2402. doi:10.1149/2.0791712jes.

[37] Y. Kim, Encapsulation of LiNi 0.5 Co 0.2 Mn 0.3 O 2 with a thin inorganic electrolyte

film to reduce gas evolution in the application of lithium ion batteries, Phys. Chem. Chem. Phys. Phys. Chem. Chem. Phys. 15 (2013) 6400–6405. doi:10.1039/c3cp50567g.

[38] M.M. Thackeray, C.S. Johnson, J.T. Vaughey, N. Li, S.A. Hackney, Advances in manganese-oxide “composite” electrodes for lithium-ion batteries, J. Mater. Chem. 15 (2005) 2257–2267. doi:10.1039/b417616m.

[39] H. Kim, K. Lee, S. Kim, Y. Kim, Fluorination of free lithium residues on the surface of lithium nickel cobalt aluminum oxide cathode materials for lithium ion batteries, Mater. Des. (2016). doi:10.1016/j.matdes.2016.03.121.

[40] L. Wang, B. Wu, D. Mu, X. Liu, Y. Peng, H. Xu, Q. Liu, L. Gai, F. Wu, Single-crystal LiNi0.6Co0.2Mn0.2O2 as high performance cathode materials for Li-ion batteries, J. Alloys Compd. (2016). doi:10.1016/j.jallcom.2016.03.061.

[41] J.C. Arrebola, Á. Caballero, L. Hernán, J. Morales, Aqueous Rechargeable Lithium Battery Based on LiNi 0.5 Mn 1.5 O 4 Spinel with Promising Performance Ni Mesh, Energy & Fuels. 27 (2013) 7854–7857. doi:10.1021/ef402188h.

[42] W. Kong, H. Li, X. Huang, L. Chen, Gas evolution behaviors for several cathode materials in lithium-ion batteries, J. Power Sources. (2005). doi:10.1016/j.jpowsour.2004.10.008.

[43] W. Li, B.L. Lucht, Lithium-Ion Batteries: Thermal Reactions of Electrolyte with the

Surface of Metal Oxide Cathode Particles, J. Electrochem. Soc. (2006). doi:10.1149/1.2210588.

[44] Z. Tang, J. Bao, Q. Du, Y. Shao, M. Gao, B. Zou, C. Chen, Surface Surgery of the Nickel-Rich Cathode Material LiNi Toward a Complete and Ordered Surface Layered Structure and Better Electrochemical Properties, (n.d.). doi:10.1021/acsami.6b11431.

[45] G. V. Zhuang, G. Chen, J. Shim, X. Song, P.N. Ross, T.J. Richardson, Li2CO3 in LiNi0.8Co0.15Al 0.05O2 cathodes and its effects on capacity and power, J. Power Sources. 134 (2004) 293–297. doi:10.1016/j.jpowsour.2004.02.030.

[46] Y. Cho, P. Oh, J. Cho, A new type of protective surface layer for high-capacity ni-based cathode materials: Nanoscaled surface pillaring layer, Nano Lett. (2013). doi:10.1021/nl304558t.

[47] H.S. Liu, Z.R. Zhang, Z.L. Gong, Y. Yang, Origin of Deterioration for LiNiO 2 Cathode Material during Storage in Air, (2004). doi:10.1149/1.1738471.

[48] J. Kim, Y. Hong, K.S. Ryu, M.G. Kim, J. Cho, Washing Effect of a LiNi[sub 0.83]Co[sub 0.15]Al[sub 0.02]O[sub 2] Cathode in Water, Electrochem. Solid-State Lett. 9 (2006) A19. doi:10.1149/1.2135427.

[49] H. Lee, M.G. Kim, J. Cho, Olivine LiCoPO4 phase grown LiCoO2 cathode material for high density Li batteries, Electrochem. Commun. 9 (2007) 149–154.

doi:10.1016/j.elecom.2006.08.058.

[50] Z. Wang, E. Liu, C. He, C. Shi, J. Li, N. Zhao, Effect of amorphous FePO4coating on structure and electrochemical performance of Li1.2Ni0.13Co0.13Mn0.54O2as cathode material for Li-ion batteries, J. Power Sources. 236 (2013) 25–32. doi:10.1016/j.jpowsour.2013.02.022.

[51] H.S. Kim, J. Kim, S. Kim, Y.D. Park, J. Mun, Post surface treatment of LiNi0.6Co0.1Mn0.3O2electrode with poly(4-vinylphenol) for lithium ion batteries, Electrochim. Acta. 246 (2017) 51–58. doi:10.1016/j.electacta.2017.05.148.

[52] J. Mun, T. Yim, J.H. Park, J.H. Ryu, S.Y. Lee, Y.G. Kim, S.M. Oh, Allylic ionic liquid electrolyte-assisted electrochemical surface passivation of LiCoO2 for advanced, safe lithium-ion batteries, Sci. Rep. 4 (2015) 5802. doi:10.1038/srep05802.

[53] K. Tasaki, A. Goldberg, J.-J. Lian, M. Walker, A. Timmons, S.J. Harris, Solubility of Lithium Salts Formed on the Lithium-Ion Battery Negative Electrode Surface in Organic Solvents, (n.d.). doi:10.1149/1.3239850.

[54] W.E. Gent, K. Lim, Y. Liang, Q. Li, T. Barnes, S.J. Ahn, K.H. Stone, M. McIntire, J. Hong, J.H. Song, Y. Li, A. Mehta, S. Ermon, T. Tyliszczak, D. Kilcoyne, D. Vine, J.H. Park, S.K. Doo, M.F. Toney, W. Yang, D. Prendergast, W.C. Chueh, Coupling between oxygen redox and cation migration explains unusual electrochemistry in lithium-rich

layered oxides, Nat. Commun. 8 (2017). doi:10.1038/s41467-017-02041-x.

[55] J. Mun, J.-H. Park, W. Choi, A. Benayad, J.-H. Park, J.-M. Lee, S.-G. Doo, S.M. Oh, New dry carbon nanotube coating of over-lithiated layered oxide cathode for lithium ion batteries, (n.d.). doi:10.1039/c4ta04818k.

[56] I.H. Son, J.H. Park, J. Mun, Surface modification of over-lithiated layered oxide by low-temperature chemical vapor deposition for high energy lithium-ion batteries, Energy Storage Mater. 4 (2016) 137–144. doi:10.1016/j.ensm.2016.05.004.

[57] Y. Zhu, X. Luo, M. Xu, L. Zhang, L. Yu, W. Fan, W. Li, Failure mechanism of layered lithium-rich oxide/graphite cell and its solution by using electrolyte additive, J. Power Sources. 317 (2016) 65–73. doi:10.1016/j.jpowsour.2016.03.090.

[58] K.S. Park, A. Benayad, M.S. Park, W. Choi, D. Im, Suppression of O2 evolution from oxide cathode for lithium-ion batteries: VOx-impregnated 0.5Li2MnO3-0. 5LiNi0.4Co0.2Mn0.4O2 cathode, Chem. Commun. 46 (2010) 4190–4192. doi:10.1039/c0cc00281j.

[59] M.M. Thackeray, S.H. Kang, C.S. Johnson, J.T. Vaughey, R. Benedek, S.A. Hackney, Li<inf>2</inf>MnO<inf>3</inf>-stabilized LiMO<inf>2</inf> (M = Mn, Ni, Co) electrodes for lithium-ion batteries, J. Mater. Chem. 17 (2007) 3112–3125. doi:10.1039/b702425h.

[60] B.M. Azmi, T. Ishihara, H. Nishiguchi, Y. Takita, Vanadyl phosphates of VOPO4 as a cathode of Li-ion rechargeable batteries, J. Power Sources. 119–121 (2003) 273–277. doi:10.1016/S0378-7753(03)00148-4.

[61] H. Lee, Y. Kim, Y.-S. Hong, Y. Kim, M.G. Kim, N.-S. Shin, J. Cho, Structural Characterization of the Surface-Modified Li[sub x]Ni[sub 0.9]Co[sub 0.1]O[sub 2] Cathode Materials by MPO[sub 4] Coating (M=Al, Ce, SrH, and Fe) for Li-Ion Cells, J. Electrochem. Soc. 153 (2006) A781. doi:10.1149/1.2172567.

[62] J. Cho, J.G. Lee, B. Kim, B. Park, Effect of P2O5 and AlPO4 coating on LiCoO2 cathode material, Chem. Mater. 15 (2003) 3190–3193. doi:10.1021/cm0302173.

[63] Enhancement in the electrochemical performance of zirconium phosphate bi-functional coatings on LiNiCoMnO2 by the removal of Li residuals(2016)_Kwangjin Park_PCCP, (n.d.).

[64] H.J. V. Tyrrell, The origin and present status of Fick's diffusion law, J. Chem. Educ. 41 (1964) 397. doi:10.1021/ed041p397.

[65] K. Matsumoto, R. Kuzuo, K. Takeya, A. Yamanaka, Effects of CO2 in air on Li deintercalation from LiNi1−x−yCoxAlyO2, J. Power Sources. 81–82 (1999) 558–561. doi:10.1016/S0378-7753(99)00216-5.

[66] J. Hyeon Jo, C.-H. Jo, H. Yashiro, S.-J. Kim, S.-T. Myung, Re-heating effect of Ni-rich

cathode material on structure and electrochemical properties, (2016). doi:10.1016/j.jpowsour.2016.02.015.

[67] J.-H. Shim, C.-Y. Kim, S.-W. Cho, A. Missiul, J.-K. Kim, Y.J. Ahn, S. Lee, Effects of heat-treatment atmosphere on electrochemical performances of Ni-rich mixed-metal oxide (LiNi0.80Co0.15Mn0.05O2) as a cathode material for lithium ion battery, Electrochim. Acta. 138 (2014) 15–21. doi:10.1016/j.electacta.2014.06.079.

[68] F. Wu, J. Tian, Y. Su, J. Wang, C. Zhang, L. Bao, T. He, J. Li, S. Chen, Effect of Ni^{2+} content on lithium/nickel disorder for Ni-rich cathode materials, ACS Appl. Mater. Interfaces. (2015). doi:10.1021/acsami.5b00645.

[69] W. Jong Lee, K. Prasanna, Y. Nam Jo, K. Jae Kim, H. Shin Kim, C. Woo Lee, Depth profile studies on nickel rich cathode material surfaces after cycling with an electrolyte containing vinylene carbonate at elevated temperature, Phys. Chem. Chem. Phys. Phys. Chem. Chem. Phys. 16 (1706) 17062–17071. doi:10.1039/c4cp02075h.

[70] A.M. Andersson, D.P. Abraham, R. Haasch, S. Maclaren, J. Liu, K. Amine, Surface Characterization of Electrodes from High Power Lithium-Ion Batteries, (2002). doi:10.1149/1.1505636.

[71] D.L. Perry, Inorganic Compound Data, in: Handb. Inorg. Compd., 2011: pp. 84–85. doi:doi:10.1201/b10908-2.

[72] Y. Bi, T. Wang, M. Liu, R. Du, W. Yang, Z. Liu, Z. Peng, Y. Liu, D. Wang, X. Sun, Stability of Li 2 CO 3 in cathode of lithium ion battery and its influence on electrochemical performance, (n.d.). doi:10.1039/c6ra00648e.

[73] M. Herstedt, M. Stjerndahl, T. Gustafsson, K. Edström, Anion receptor for enhanced thermal stability of the graphite anode interface in a Li-ion battery, Electrochem. Commun. (2003). doi:10.1016/S1388-2481(03)00106-1.

[74] Y.-S. Kang, T. Yoon, J. Mun, M.S. Park, I.-Y. Song, A. Benayad, S.M. Oh, Effective passivation of a high-voltage positive electrode by 5-hydroxy-1H-indazole additives, (n.d.). doi:10.1039/c4ta01891e.

[75] Y.-M. Lin, K.C. Klavetter, P.R. Abel, N.C. Davy, J.L. Snider, A. Heller, C.B. Mullins, High performance silicon nanoparticle anode in fluoroethylene carbonate-based electrolyte for Li-ion batteriesw, Chem. Commun. Chem. Commun. 48 (2012) 7268–7270. doi:10.1039/c2cc31712e.

[76] H. Yildirim, A. Kinaci, M.K.Y. Chan, J.P. Greeley, First-Principles Analysis of Defect Thermodynamics and Ion Transport in Inorganic SEI Compounds: LiF and NaF, ACS Appl. Mater. Interfaces. (2015). doi:10.1021/acsami.5b02904.

[77] A. Zaban, E. Zinigrad, D. Aurbach, Impedance Spectroscopy of Li Electrodes. 4. A General Simple Model of the Li-Solution Interphase in Polar Aprotic Systems, (n.d.).

[78] J.H. Song, J.H. Shim, A. Kapylou, D.H. Yeon, D.H. Lee, D.H. Kim, J.H. Park, S.H. Kang, Suppression of voltage depression in Li-rich layered oxide by introducing GaO4 structural units in the Li2MnO3-like nano-domain, Nano Energy. 30 (2016) 717–727. doi:10.1016/j.nanoen.2016.09.028.

[79] B.M. Azmi, T. Ishihara, H. Nishiguchi, Y. Takita, Cathodic performance of VOPO4 with various crystal phases for Li ion rechargeable battery, Electrochim. Acta. 48 (2002) 165–170. doi:10.1016/S0013-4686(02)00597-2.

[80] A. Tron, Y.N. Jo, S.H. Oh, Y.D. Park, J. Mun, Surface Modification of the LiFePO4Cathode for the Aqueous Rechargeable Lithium Ion Battery, ACS Appl. Mater. Interfaces. 9 (2017) 12391–12399. doi:10.1021/acsami.6b16675.

[81] S.-U. Woo, C.S. Yoon, K. Amine, I. Belharouak, Y.-K. Sun, Significant Improvement of Electrochemical Performance of AlF[sub 3]-Coated Li[Ni[sub 0.8]Co[sub 0.1]Mn[sub 0.1]]O[sub 2] Cathode Materials, J. Electrochem. Soc. 154 (2007) A1005. doi:10.1149/1.2776160.

[82] Y.-K. Sun, S.-T. Myung, B.-C. Park, J. Prakash, I. Belharouak, K. Amine, High-energy cathode material for long-life and safe lithium batteries, Nat. Mater. 8 (2009). doi:10.1038/NMAT2418.

[83] A. Manthiram, B. Song, W. Li, A perspective on nickel-rich layered oxide cathodes for

lithium-ion batteries, Energy Storage Mater. (2017). doi:10.1016/j.ensm.2016.10.007.

[84] E. Zhecheva, R. Stoyanova, Stabilization of the layered crystal structure of $LiNiO_2$ by Co-substitution, Solid State Ionics. 66 (1993) 143–149. doi:10.1016/0167-2738(93)90037-4.

[85] A. Rougier, Effect of cobalt substitution on cationic distribution in LiNi1 − y CoyO2 electrode materials, Solid State Ionics. 90 (1996) 83–90. doi:10.1016/S0167-2738(96)00370-0.

[86] C. Delmas, I. Saadoune, A. Rougier, The cycling properties of the LixNil _ yCOyO2 electrode, 44 (1993) 595–602.

[87] J. Li, R. Doig, J. Camardese, K. Plucknett, J.R. Dahn, Measurements of Interdiffusion Coefficients of Transition Metals in Layered Li-Ni-Mn-Co Oxide Core-Shell Materials during Sintering, Chem. Mater. 27 (2015) 7765–7773. doi:10.1021/acs.chemmater.5b03499.

[88] X. Li, J. Liu, M.N. Banis, A. Lushington, R. Li, M. Cai, X. Sun, Atomic layer deposition of solid-state electrolyte coated cathode materials with superior high-voltage cycling behavior for lithium ion battery application, Energy Environ. Sci. 7 (2014) 768–778. doi:10.1039/c3ee42704h.

[89] F. Schipper, E.M. Erickson, C. Erk, J.-Y. Shin, F.F. Chesneau, D. Aurbach, Review—

Recent Advances and Remaining Challenges for Lithium Ion Battery Cathodes, J. Electrochem. Soc. 164 (2017) A6220–A6228. doi:10.1149/2.0351701jes.

[90] R.R. Kuruppathparambil, T. Jose, R. Babu, G.Y. Hwang, A.C. Kathalikkattil, D.W. Kim, D.W. Park, A room temperature synthesizable and environmental friendly heterogeneous ZIF-67 catalyst for the solvent less and co-catalyst free synthesis of cyclic carbonates, Appl. Catal. B Environ. 182 (2016) 562–569. doi:10.1016/j.apcatb.2015.10.005.

[91] S. Li, X. Fu, J. Zhou, Y. Han, P. Qi, X. Gao, X. Feng, B. Wang, Supporting Information for Effect approach to improve the electrochemical performance of LiNi 0.6 Co 0.2 Mn 0.2 O 2 cathode material by MOF-derived coating Experimental section, (n.d.).

[92] M.H. Oh, T. Yu, S.-H. Yu, B. Lim, K.-T. Ko, M.-G. Willinger, D.-H. Seo, B.H. Kim, M.G. Cho, J.-H. Park, K. Kang, Y.-E. Sung, N. Pinna, T. Hyeon, Galvanic Replacement Reactions in Metal Oxide Nanocrystals, Science (80-.). 340 (2013) 964–968. doi:10.1126/science.1234751.

[93] G. Kresse and J.Hafner, Inition Method, 47 (1992). doi:10.1103/PhysRevB.47.558.

[94] G. Kresse, J. Furthmiiller, Water news roundup, J. / Am. Water Work. Assoc. 96 (1996) 14–20. doi:10.1016/0927-0256(96)00008-0.

[95] A. Rolland, L. Pouget, M. Brunel, G. Loas, M. Alouini, Bridging the THz to RF gap by four-wave mixing in a highly nonlinear fiber, 59 (2013) 3–4.

doi:10.1103/PhysRevB.59.1758.

[96] P.W. Tasker, The stability of ionic crystal surfaces. Journal of Physics C: Solid State Physics, 12(22), 4977., (1979) 3865–3868. doi:10.1103/PhysRevLett.77.3865.

[97] L. Wang, T. Maxisch, G. Ceder, A first-principles approach to studying the thermal stability of oxide cathode materials, Chem. Mater. 19 (2007) 543–552. doi:10.1021/cm0620943.

[98] H. Wu, X. Qian, H. Zhu, S. Ma, G. Zhu, Y. Long, Controlled synthesis of highly stable zeolitic imidazolate framework-67 dodecahedra and their use towards the templated formation of a hollow Co3O4 catalyst for CO oxidation, RSC Adv. 6 (2016) 6915–6920. doi:10.1039/C5RA18557B.

[99] P. Krokidas, M. Castier, S. Moncho, D.N. Sredojevic, E.N. Brothers, H.T. Kwon, H.-K. Jeong, ‖ Jong, S. Lee, I.G. Economou, ZIF-67 Framework: A Promising New Candidate for Propylene/ Propane Separation. Experimental Data and Molecular Simulations, (n.d.). doi:10.1021/acs.jpcc.6b00305.

[100] A. Greenwood, Norman N.; Earnshaw, Chemistry of the Elements (2nd ed.), Butterworth-Heinemann, 1997.

[101] X. Xia, Y. Wang, A. Ruditskiy, Y. Xia, 25th anniversary article: Galvanic replacement: A simple and versatile route to hollow nanostructures with tunable and well-controlled

properties, Adv. Mater. 25 (2013) 6313–6332. doi:10.1002/adma.201302820.

[102] 이승원최수안, Silicon carbide-free graphene growth on silicon for lithium-ion battery with high volumetric energy density, Nat. Commun. 9 (2017) 1–6. doi:10.1038/ncomms8393.

[103] W. Liu, P. Oh, X. Liu, M.J. Lee, W. Cho, S. Chae, Y. Kim, J. Cho, Nickel-Rich Layered Lithium Transition-Metal Oxide for High-Energy Lithium-Ion Batteries, Angew. Chemie - Int. Ed. (2015). doi:10.1002/anie.201409262.

[104] H.J. Noh, S. Youn, C.S. Yoon, Y.K. Sun, Comparison of the structural and electrochemical properties of layered Li[NixCoyMnz]O2 (x = 1/3, 0.5, 0.6, 0.7, 0.8 and 0.85) cathode material for lithium-ion batteries, J. Power Sources. (2013). doi:10.1016/j.jpowsour.2013.01.063.

Curriculum Vitae Jun-Ho Park

Staff Researcher

Energy Lab, Samsung advanced Institute of Technology (SAIT), 130, Samsung-ro,

Yeongtong-gu, Suwon-si, Gyeonggi-do, 443-803, Republic of Korea

Tel:+82-31-8061-1263, FAX:+82-31-8061-1319

e-mail: agentpark11@gmail.com

PERSONAL

Name: Jun-Ho Park

Sex: male

Date of Birth: August, 1st, 1983

Nationality: Republic of Korea

EDUCATION

Seoul National University, Seoul, Korea

Ph.D. in Materials Science and Engineering (2019)

Advisor: Prof. Heung Nam Han

Thesis: Design of Layered Cathode Materials for High-Performance Li-Ion Batteries(고성능 리튬이온전지용 층상구조 양극소재의 설계)

Seoul National University, Seoul, Korea

M.S. in Materials Science and Engineering (2011)

Advisor: Prof. Heung Nam Han

Thesis: Statistical analysis on evolution of recrystallization texture in AZ31 magnesium alloy sheet (AZ31 마그네슘합금 판재의 재결정 집합조직 형성에 관한 통계적 고찰)

Hanyang University, Seoul, Korea

B.S. in Materials Science and Engineering (2007)

EXPERIENCE

Energy Lab., Samsung Advanced Institute of Technology(SAIT), Staff Researcher, High Energy Density LIB Material project (Aug. 2011 – Present)

RESEARCH INTERESTS & TECHNICAL SKILLS

- **Material design, synthesis and characterization**

- **Cathode material:** High energy density layered cathode (OLO, Ni-rich layered oxides)
- **Post-treatment process:** wet process, dry process, sintering.
- **Large scale material synthesis**

- **Cell design**

- High capacity & safe design

- High density electrode design

- **Electrochemical analysis**

- Fabrication and optimization of electrodes and cells

- Cell diagnostics, Degradation mechanism.

- Analysis : galvanostatic, EIS

- **Software**

Minitab, Microsoft office, Origin, Mendeley

JOURNAL PUBLICATIONS

[1] Jun-Ho Park, Kwangjin Park, Dongwook Han*, Byungjin Choi, Seong Yong Park, Jin-Hwan Park, Heung Nam Han, Kang Hee Lee*, "Molecular-level Surface Rearrangements for High-stability Ni-rich Layered Oxide Cathode Materials using Metal-organic Frameworks", submitted

[2] Dong-Su Ko†*, Jun-Ho Park†, Sungjun Park, Yong Nam Ham, Sung Jin Ahn, Jin-Hwan Park, Heung Nam Han, Eunha Lee, Woo Sung Jeon, and Changhoon Jung*, "Microstructural visualization of compositional changes induced by transition metal

dissolution in Ni-rich layered cathode materials by high-resolution particle analysis", Nano Energy 56 (2019) 434-442

[3] Kwangjin Park*, Juyong Kim, Jun-Ho Park, Yunil Hwang, Dongwook Han*, "Synchronous Phase Transition and Carbon Coating on the Surface of Li-rich Layered Oxide Cathode Materials for Rechargeable Li-ion Batteries", Journal of Power Sources 408 (2018) 105–110

[4] Dongwook Han, Kwangjin Park*, Jun-Ho Park, Dong-Jin Yun, You-Hwan Son, "Selective doping of Li-rich layered oxide cathode materials for high-stability rechargeable Li-ion batteries", Journal of Industrial and Engineering Chemistry, 68, (2018), 180-186,

[5] Jun-Ho Park, Jin-Hwan Park, Seonghun Jeong, Heung Nam Han, Junyoung Mun*, "Mechanochemical coating with nano-$VOPO_4$: Over lithiated layered oxide with high coulombic efficiency and good thermal stability", Electrochimica Acta, 282, (2018), 582-587

[6] Jun-Ho Park, Byungjin Choi, Yoon-Sok Kang, Seong Yong Park, Dong Jin Yun, Insun Park, Jae Ha Shim, Jin-Hwan Park, Heung Nam Han, Kwangjin Park*, "Effect of Residual Lithium Rearrangement on Ni-richLayered Oxide Cathodes for Lithium-Ion Batteries", Energy Technol. (2018), 6, 1361 – 1369

[7] Kwangjin Park, Jun-Ho Park*, Byungjin Choi, Jung Hwa Kim, Suk-Gi Hong*, Heung Nam Han, "Metal phosphate-coated Ni-rich layered oxide positive electrode materials for Li-ion

batteries: improved electrochemical performance and decreased Li residuals content", Electrochimica Acta, 257, (2017), 217–223

[8] Kwangjin Park, Jun-Ho Park, Suk-Gi Hong, Byungjin Choi, Sung Heo, Seung-Woo Seo, Kyoungmin Min, Jin-Hwan Park, "Re-construction layer effect of $LiNi_{0.8}Co_{0.15}Mn_{0.05}O_2$ with solvent evaporation process", Sci. Rep, (2017), 7, 44557.

[9] Yoon-Sok Kang*, Min Sik Park, Insun Park, Dong Young Kim, Jun-Ho Park, Kwangjin Park, Meiten Koh, Seok-Gwang Doo, "Tetrathiafulvalene as a Conductive Film-Making Additive on High-Voltage Cathode", ACS Appl. Mater. Interfaces, (2017), 9, 3590－3595

[10] Kwangjin Park*, Jun-Ho Park, Suk-Gi Hong, Byungjin Choi, Seung-Woo Seo, Jin-Hwan Park, Kyoungmin Min, "Enhancement in the electrochemical performance of zirconium/phosphate bi-functional coatings on $LiNi_{0.8}Co_{0.15}Mn_{0.05}O_2$ by the removal of Li residuals", Phys.Chem.Chem.Phys.,(2016), 18, 29076

[11] Kwangjin Park, Jun-Ho Park, Suk-Gi Hong, Jaegu Yoon, Seongyong Park, Jung-Hwa Kim, Dongjin Yoon, Hyunjin Kim, You-Hwan Son*, Jin-Hwan Park, Soonchul Kwon, "Induced AlF_3 segregation for the generation of reciprocal Al_2O_3 and LiF coating layer on self-generated $LiMn_2O_4$ surface of over-lithiated oxide based Li-ion battery", Electrochimica Acta, 222, (2016), 830–837

[12] Kwangjin Park*, Byoung-Sun Lee, Jun-Ho Park and Suk-Gi Hong, The synergistic effect

of inert oxide and metal fluoride dual coatings on advanced cathode materials for lithium ion battery applications", *Phys.Chem.Chem.Phys., (*2016), 18, 15861

[13] Byoung-Sun Lee, Jihyun Yoon, Changhoon Jung, Dong Young Kim, Seung-Yeol Jeon, Ki-Hong Kim, Jun-Ho Park, Hosang Park, Kang Hee Lee, Yoon-Sok Kang, Jin-Hwan Park, Heechul Jung*, Woong-Ryeol Yu*, Seok-Gwang Doo "Silicon/Carbon Nanotube/$BaTiO_3$ Nanocomposite Anode: Evidence for Enhanced Lithium-Ion Mobility Induced by the Local Piezoelectric Potential", ACS Nano, (2016), 10, 2617－2627

[14] Jun-Ho Park, Kwangjin Park, Ryoung-Hee Kim, Dong-Jin Yun, Seong-Yong Park, Dongwook Han*, Seok-Soo Lee and Jin-Hwan Park, "Improving the kinetics and surface stability of sodium manganese oxide cathode materials for sodium rechargeable batteries with Al_2O_3/MWCNT hybrid networks", J. Mater. Chem. A, (2015), 3, 10730

[15] Wonchang Choi, Anass Benayard, Jin-Hwan Park, Junho Park, Seok-Gwang Doo, Junyoung Mun, "Versatile Coating of Lithium Conductive Li_2TiF_6 on Over-lithiated Layered Oxide in Lithium-Ion Batteries", Electrochimica Acta 117 (2014) 492– 497

[16] Junyoung Mun, Jin-Hwan Park, Wonchang Choi, Anass Benayad, Jun-Ho Park, Jae-Myung Lee, Seok-Gwang Doo, Seung M. Oh*, "New dry carbon nanotube coating of over-lithiated layered oxide cathode for lithium ion batteries", J. Mater. Chem. A, (2014), 2, 19670

[17] Jun-Ho Park, Tae-Hong Ahn, Hyun-Sik Choi, Jung-Man Chung, Dong-Ik Kim, Kyu Hwan Oh, Heung Nam Han, "Statistical Analysis on Static Recrystallization Texture Evolution in Cold-Rolled AZ31 Magnesium Alloy Sheet", Microsc. Microanal. (2013), 19, S5, 21–24,

† These authors contributed equally.

* Corresponding authors.

CONFERENCES

<Oral presentation>

[1] Jun-Ho Park *, Byungjin Choi, Kwangjin Park, Kang Hee Lee, Seong Yong Park, Jin-Hwan Park, Heung Nam Han, "A Simple Method for Molecular level Modification of Ni-rich Layered Oxide Cathode for Lithium-ion Batteries using Metal-organic Frameworks", American Chemcial Society(ACS) (Boston, Aug., 21th, 2018)

[2] Junyoung Mun, Jun-Ho Park*, Jaegu Yoon, Jinhwan Park, Jaemyung Lee, Byungjin Choi, Yoon Seok Kang, Myunghoon Kim and Seok Gwang Doo, "Diverse Surface Modifications of Over-lithiated Layered Oxide Cathode Material for Lithium Ion Batteries" Materials Research Society(MRS) (Boston, Dec. 4th. 2013)

<Poster presentation>

[1] Jun-Ho Park*, Junyoung Mun, Dongwook Han, Heung Nam Han, Jin-Hwan Park, "Surface treatments assisted by CNT networks of over-lithiated layered oxide cathode materials for lithium ion batteries" 한국전기화학회 (spring, 2017)

[2] 박준호*, 문준영, 박진환, 윤재구, "$VOPO_4$가 도입된 리튬이차 전지용 고용량 과리튬화양극 소재의 성능 개선 및 고찰", 한국전기화학회 (spring, 2013)

Patents

[1] S.Hong, Y.Son, B.Yu, K.Park, J.H.Park, J.Park, B.Choi, Composite cathode active material, method of preparing the same, and cathode and lithium battery including th composite cathode active material(CoMOx를 포함하는 코팅층을 갖는 Ni계 LIB 양극 소재), (US patent App.:US16/102087, Filed:08/1/2018, Korea patent App.:P20170110344, Filed:08/30/2017)

[2] J.H.Park, K.Park, Y.Son, K.Lee, S.Hong, B.Choi, Composite cathode active material, cathode and lithium battery including the composite cathode active material, and method of prepating the composite cathode active material(M-NC 표면처리를 통해 전기화학성능 및 셀안전성이 향상된 리튬이차전지용 양극활물질), (US patent App.:US15/876410, Filed:01/22/2018, Korea patent App.:P2017/0055758, Filed:04/28/2017)

[3] S.Hong, K.Park, J.H.Park, B.Choi, Dual coated NCM cathode material with acid treatment for Li ion battery(산처리가 추가된 산화물과 인산염계 물질의 코팅을 통한 전기화학 성능이 향상된 양극 활물질), (US patent App.:US15/403583, Filed:01/11/2017, Korea patent App.:P20160075839, Filed:06/17/2016)

[4] Y.Son, S.Park, J.Ha, S.Hong, K.Park, J.H.Park, B.Choi, Cathode composition comprising layer-layer hybrid material and therof (층상-층상 하이브리드 양극 산화물 및 그의 제조 방법), (US patent App.:US15/622133, Filed:06/14/2017, Korea patent App.:P20160073828, Filed:06/14/2016)

[5] J.H.Park, K.Park, D.Shin, J.Yoon, S.Hong, Composite cathode active material for lithium battery, cathode for lithium battery including the same, and lithium battery including the cathode(리튬전지용 양극 활물질, 이를 포함하는 리튬전지용 야윽 및 리튬전지), (US patent No.:US15/152861, issued:11/14/2018, Korea patent App.:P20150180199, Filed:12/16/2015)

[6] J.Mun, G.Kim, H.Jung, J.H.Park, Composite for anode active material, anode including the composite, lithium secondary battery including the anode, and method of preparing the composite(음극 활물질 복합체, 상기 활물질 복합체를 포함하는 음극, 상기 음극을 포함하는 리튬 이차전지, 및 상기 음극 활물질 복합체의 제조방법), (US patent No.:US15/172259, issued:06/03/2016, Korea patent

App.:P20150081504, Filed:06/09/2015)

[7] S.Hong, K.Park, J.H.Park, J.Yoon, Electrochemical performance enhanced cathode material using Metal oxide and LiF dual coating for Li batteries(금속산화물/LiF Dual coating을 통한 전기화학 성능 향상된 양극 활물질), (US patent App.: US15/207885, Filed:07/12/2016, Korea patent App.: P20150099224, Filed:07/13/2015)

[8] B.Choi, Y.Kang, J.H.Park, J.Park, S.Ahn, D.Yeon, J.Yoon, Composite cathode active material, method of preparing the same, and cathode and lithium battery containing the same(Li2CoMn3O8 포함된 복합양극활물질, 그 제조방법 및 이를 채용한 양극과 리튬이차전지), (US patent No.:US10044030, issued:08/07/2018 Korea patent No. P1675110, issued:11/04/2016)

[9] J.H.Park, W.Choi, J.Yoon, Y.Kang, J.Park, S.Ahn, J.Chang, B.Choi, The cathode active matierls which contain fully fluorinated polymer and secondary lithium ion battery comporising the same(불소계고분자 및 카본나노튜브가 포함된 양극활물질 및 이를 사용한 전지), (US patent App. US14/02358, Filed:01/22/2015, Korea patent App. P201400665522, Filed:05/30/2014)

[10] B. Choi, Y. Kang, J. Park, Y.Yoon, M.Kim, J.Mun, J.H.Park, S.Ahn, Cathode material for lithium secondary battery stabilized with spinel phase(Spinel phase도입으로 OLO 구조 안정화된 리튬 이차전지용 양극재료), (US patent No.

US9373868, Issued:02/24/2016, Korea patent App. P20130111186, Filed:09/16/2013)

[11] J. Lee, J. Mun, K. Kim, Y. Kang, M, Kim, J.H. Park, J.Park, J.Yoon, B.Choi, Composite cathode active material, method of preparing the composite cathod active material, and cathode and lithium battery each including the composite cathode active material(리튬전도체가 코팅된 리튬이차전지용 양극 물질), (US patent No. US10056608, Issued 08/21/18 Korea patent App. P20130072720, Filed 06/24/2013)

[12] J.H. Park, J.Mun, J. Park, J.Yoon, Cathode materials including inorganic materials and carbon nano tube for rechargeable lithium ion battery(무기물 및 CNT가 포함된 리튬이차전지용 양극물질), (US patent App. US14/311491, Filed:06/23/2014, Korea Patent App. P20130091162, Filed:07/31/2013)

[13] J. Park, J. Mun, K. Kim, J.H. Park, J. Yoon, Composite cathode active material, preparation method thereof, and cathode and lithium battery containing the material (리튬이차전지용 양극물질), (US patent App. US14/051600, Filed:10/11/2013, Korea patent App. P20120119294, Filed:10/25/2012)

[14] J.H. Park, J. Mun, J. Park, Y. Yoon, Cathode material including VOPO4 for rechargeable lithium ion battery (바나듐인산화물이 포함된 리튬이차전지용 양극소재), (US patent App. US13/849839, Filed:03/25/2013, Korea patent App. P20120114196, Filed:10/15/2012)

[15] J. Yoon, J. Mun, J. Park, J.H. Park, Cathode materials coated by carbon nano tube for rechargeable lithium ion battery (탄소 나노 튜브가 코팅된 리튬 이차전지용 양극 물질), (US patent App. US13/707215, Filed:06/13/2012, Korea patent App. p20120063409, Filed:06/13/2012, China patent App. 201310232576.6, Filed:06/13/2013, Europe patent App. 13171687.0, Filed:12/06/2013)

초 록

에너지 및 환경 문제가 대두됨에 따라 리튬이온전지의 그 중요성은 더해지고 있으며, 전기자동차, 전력저장에 적용하기 위해 고용량, 장수명, 낮은 비용을 갖는 양극소재에 대한 연구가 활발히 진행되고 있다. 본 연구에서는 고에너지밀도 양극소재로서 가장 주목 받고 있는 과리튬망간복합산화물과 고함량니켈산화물의 성능향상을 위한 연구이다. 성능향상을 위해 두 양극의 고유특성에 대해서 완전한 이해가 필요하며 그 특성에 따라 후처리법을 달리해야 한다. 과리튬망간복합산화물은 첫번째 사이클에서의 비가역성, 수명저하, 전압강하 등이 개선할 점이고, 고함량니켈산화물의 경우, 잔류리튬제거, 리튬 및 니켈의 자리변경, 고온안전성, 수명저하 등을 개선해야 한다. 특히, 셀 내에서 양극의 문제는 표면에서 시작되어 내부로 전파되기 때문에, 적절한 후처리 방법은 적절한 표면개질에서부터 고에너지밀도양극소재의 성능을 최대한은 이끌어 낼 수 있다, 그리하여, 후처리법과 그 원리이해는 학계뿐만 아니라, 산업계에서도 관심사항이다. 하지만, 그 원리가 불분명하고 많이 알려져 있지 않아서, 연구가 필요한 상황이다.

본 연구에서는 고에너지밀도 양극소재의 성능향상을 위하여 양극종류에 따른 고유특성과 미비점을 보완할 수 있는 전통적인 후처리 방법을 분류하였고, 각 항목에 대해 케이스실험을 수행하였다. 그리고 나아가서 MOF 열분해를 이용한

새로운 표면처리방법을 제안하였다.

전통적인 방법으로서 크게 증발방식 및 필터링방식을 포함하는 습식후처리와 블렌딩 및 메카노퓨전방식을 포함하는 건식후처리 방식이 있으며, 각 방법에 해당하는 케이스실험을 수행하여 이들의 장점 및 단점에 대해 알 수 있었다.

습식후처리법은 리튬잔여물(또는 잔류리튬)제어가 필수적인 고함량니켈산화물에 주로 적합한 방법이며, 증발방식과 필터링 방식으로 나눌 수 있었다. 증발방식은 잔류리튬제거효과는 불충분하였지만, 활물질 손상은 적었고, 표면코팅층 형성에는 효과적이었다. 필터링방식 리튬제거에는 매우 효과적이었지만, 성능감소가 발생할 가능성이 있었다. 건식방법은 기능성코팅층 형성에 효과적일 수 있었으나, 균일한 코팅층형성은 어려운 점이 있었다. 메카노퓨전방식으로 전기화학 및 열적안정소재인 바나딜인산을 과리튬망간복합산화물에 건식표면처리 하였으며, 첫번째 사이클 효율저하 및 열적안정성을 개선할 수 있었다.

최종적으로는, Co를 포함하는 MOF의 열분해를 이용하여 고함량니켈산화물에 안정구조를 도입할 수 있었다. 건식후처리로 기능성소재를 도입한 후 잔류리튬제거 등의 습식공정기반의 후처리효과를 얻을 수 있는 새로운 방법을 제안하였다. 적용결과, 기존의 층상구조에 안정한 유사스피넬구조를 일부 도입한 양극을 얻을 수 있었고, 무게비 1%정도 적용 시, 셀 수명 및 열적안정성도 확보를 확인 할 수 있었다.

본 연구결과는 향후 고용량 층상구조 양극 소재의 상용화를 위한 성능향상에 기여할 수 있을 것으로 기대된다.

주요어: 이차전지, 양극, 층상구조, 리튬이온전지, 후처리, 표면처리

학 번: 2016-30201